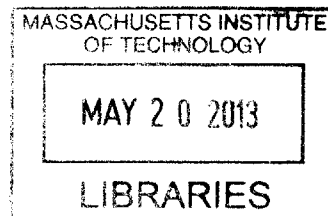


Thermodynamic properties and atomic structure **ARCHIVES**  
of Ca-based liquid alloys



by

Sophie Poizeau

Ingénieur Centralien, École Centrale Paris, France (2008)

Submitted to the Department of Materials Science and Engineering  
in partial fulfillment of the requirements for the degree of

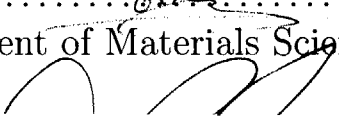
Doctor of Philosophy in Materials Science and Engineering

at the

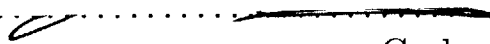
MASSACHUSETTS INSTITUTE OF TECHNOLOGY

February 2013

© Massachusetts Institute of Technology 2013. All rights reserved.

Author .....  
Department of Materials Science and Engineering  
  
September 9, 2012

Certified by .....  
  
Donald R. Sadoway  
John F. Elliott Professor of Materials Chemistry  
Thesis Supervisor

Accepted by .....  
  
Gerbrand Ceder  
Chairman, Department Committee on Graduate Students



# Thermodynamic properties and atomic structure of Ca-based liquid alloys

by

Sophie Poizeau

Submitted to the Department of Materials Science and Engineering  
on September 9, 2012, in partial fulfillment of the  
requirements for the degree of  
Doctor of Philosophy in Materials Science and Engineering

## Abstract

To identify the most promising positive electrodes for Ca-based liquid metal batteries, the thermodynamic properties of diverse Ca-based liquid alloys were investigated. The thermodynamic properties of Ca-Sb alloys were determined by emf measurements. It was found that Sb as positive electrode would provide the highest voltage for Ca-based liquid metal batteries (1 V). The price of such a battery would be competitive for the grid-scale energy storage market. The impact of Pb, a natural impurity of Sb, was predicted successfully and confirmed via electrochemical measurements. It was shown that the impact on the open circuit voltage would be minor. Indeed, the interaction between Ca and Sb was demonstrated to be much stronger than between Ca and Pb using thermodynamic modeling, which explains why the partial thermodynamic properties of Ca would not vary much with the addition of Pb to Sb. However, the usage of the positive electrode would be reduced, which would limit the interest of a Pb-Sb positive electrode.

Throughout this work, the molecular interaction volume model (MIVM) was used for the first time for alloys with thermodynamic properties showing strong negative deviation from ideality. This model showed that systems such as Ca-Sb have strong short-range order: Ca is most stable when its first nearest neighbors are Sb. This is consistent with what the more traditional thermodynamic model, the regular association model, would predict. The advantages of the MIVM are the absence of assumption regarding the composition of an associate, and the reduced number of fitting parameters (2 instead of 5). Based on the parameters derived from the thermodynamic modeling using the MIVM, a new potential of mixing for liquid alloys was defined to compare the strength of interaction in different Ca-based alloys. Comparing this trend with the strength of interaction in the solid state of these systems (assessed by the energy of formation of the intermetallics), the systems with the most stable intermetallics were found to have the strongest interaction in the liquid state. Eventually, a new criteria was formulated to select electrode materials for liquid metal batteries. Systems with the most stable intermetallics, which can be evaluated by the enthalpy of formation of these systems, will yield the highest voltage when assembled

as positive and negative electrodes in a liquid metal battery.

Thesis Supervisor: Donald R. Sadoway

Title: John F. Elliott Professor of Materials Chemistry

# Acknowledgments

First and foremost, I would like to thank my advisor, Prof. Don Sadoway, for his great mentorship, his words of wisdom and teaching me how to think. He always knew when to support me when challenges were coming up and give me confidence in my research approaches. Thank you also to my committee members, Prof. Chris Schuh and Prof. Tom Eagar, with whom I was able to discuss scientific ideas and life in general. I also want to thank Prof. Antoine Allanore, who gave me input during my past 2 years at MIT, and provided insightful feedback at my preliminary defense.

Thank you also to the different organizations that supported me at MIT: chronologically, the MIT presidential fellowship, the Jean Gaillard fellowship, NASA, the American and Iron Steel Institute, Total S.A. — and in particular Dr. Shaffiq Jaffer who organized biannual meetings at which he gave me the opportunity to present and discuss my research with many other researchers at Total, ARPA-E, and the ECS battery division for their travel grant.

I was lucky to be surrounded by many amazing researchers during my time at MIT, without whom I would never have been able to know how to start being a researcher myself. Among my colleagues, I would like to express special thanks to Dr. Dane Boysen, who took me under his wing at a time when I was questioning my ability to pursue a PhD, Dr. Hojong Kim, for his great mentorship and teaching me how to run and think about experiments, at a time when I hadn't have any such experience, and Dr. Taka Ouchi for his constant eagerness and availability to share his knowledge and experience. Jocelyn Newhouse and John Rogosic have also always been here to give me most valuable input, both at a scientific level on an everyday basis and at a grammatical level for my papers, which was always very helpful, especially for a non-native speaker. And of course, I want to address my deepest gratitude to all the past and present members of the Sadoway group, who shared their life wisdom and scientific knowledge with me. You really made me appreciate being part of this group and come to work with you as part of a team. Thank you to the liquid metal battery research group: Dr. Dave Bradwell, Dr. Paul Burke, Dr. Brice Chung, Dr. Kai Jiang, Dr. Ulrich Muecke, Dr. Xiaohui Ning, Dr. Jit Phadke, Dr. Alina Tomaszowska, Dr. Greg Thompson, Dr. Kangli Wang, Dr. Weifeng Wei, Dr. Lan Yin, Adam LaDelpha, Sal Barriga, and Brian Spatocco. Thank you also to all the other researchers of the Sadoway group and in particular Dr. Ghazal Azimi and Dr. Aislinn Sirk, as well as our amazing administrative assistant Hilary Sheldon, who is responsible for making everything look easy at MIT.

During my thesis work at MIT, I collaborated with the Snyder group at Caltech to prepare some samples. I could not have dreamt of a more welcoming group. Thank you Dr. Snyder for welcoming me, inviting me to play frisbee and discuss science with you. Thank you Alex Zevalkink for spending two weeks working with me, having barbecue at your place looking more and more cosy every day, showing me around and being such a great friend.

MIT has always been able to provide me with the most capable people to discuss and help with my everyday work related questions. I would like to thank the MIT

Libraries, and in particular Angie Locknar and Daniel Pribble, who helped me track down old reports and many other articles across the United States, as well as Dr. Neel Chatterjee for the use of the microprobe and Patrick Boisvert for training me to use the SEM. Thank you also to Mike Tarkanian and Matt Humbert for their practical wisdom.

These past five years were certainly among the most amazing ones I have had so far, and part of this was due to the fact that MIT is one of these rare places that encourages students to have a balanced life to bring the most of themselves to work as well. And it certainly participated to my work motivation and progress. In my case, I was able to continue playing the flute in the MIT Wind Ensemble, directed by Dr. Fred Harris, an astonishing musician and caring person. Our 5 weekly hours of rehearsal at night were always a time I was looking forward to, both for the amazing repertoire and the amazing people I met there during the years. Thank you Shannon, Marta, Helen, Emily and Emily, Eric, Sarah and all the wind ensemble musicians and collaborators. Thank you also to my fantastic flute teacher, Sue-Ellen Hershman-Tcherepnin, in particular to organize our May recital with Fred Harris. This was definitely one of the best times I had in these 5 years.

My friends have also been crucial to keep me going in the times of doubt, and share all the excitement that also comes with research. Thank you Heather, for making your office the most likely place to find me when I wasn't in the lab or in my office, sharing our ups and downs with research while enjoying tea, going to the gym, and a conference together. MIT wouldn't have been the same without you. Thank you Tracey for our Starbucks breaks building a better world. Thank you Liz for all the fun we had together, in particular for our videos and other EHS competitions. Thank you Caro for our runs and more together, and getting me to run a 10K! Thank you Tess for our "date" nights I am always looking forward to.

Last but not least, my deepest love and gratitude go to my family, and in particular my parents and sister without whom I wouldn't be where and who I am today. Thank you for always being supportive, coming to visit me so often in Boston, while my 10 days off were not enough to see you as much as I would have wished for. Thank you for being such a loving family, teaching me your values and having always been here for me all the years. My love and gratitude also go to my longtime boyfriend Romain, who probably knows more about liquid metals than he ever wished for, for his continuous support and love every day of my PhD.

Thank you all.

# Contents

<b>1</b>	<b>List of constants, symbols, and acronyms</b>	<b>21</b>
1.1	Constants . . . . .	21
1.2	Symbols . . . . .	22
1.3	Acronyms and abbreviations . . . . .	23
<b>2</b>	<b>Introduction</b>	<b>25</b>
2.1	Liquid metal batteries . . . . .	25
2.1.1	From waste heat recovery to grid-scale storage . . . . .	25
2.1.2	Unique characteristics of liquid metal batteries . . . . .	27
2.1.3	Operating principles of liquid metal batteries . . . . .	28
2.2	Selection of the materials of interest . . . . .	29
2.2.1	Selection criteria for the electrodes . . . . .	30
2.2.2	Ca-based liquid metal batteries . . . . .	32
2.3	Research objectives . . . . .	35
2.3.1	How can we quantify the theoretical voltage of a Ca  Sb LMB for appropriate ranges of temperature and composition? . . .	35
2.3.2	How can we correlate the OCV of a Ca  Sb LMB with the struc- ture of the Ca-Sb alloys? . . . . .	36
2.3.3	Are systems with high-melting intermetallics interesting to use in LMB, and if so why? . . . . .	36
2.3.4	Can we use our thermodynamic modeling of binaries to predict the OCV of a Ca  X-Y LMB? . . . . .	37
2.4	Conclusions of the chapter . . . . .	37

<b>3</b>	<b>Thermodynamic properties of mixing of liquid calcium-antimony alloys via emf measurements</b>	<b>39</b>
3.1	Experimental methods for the determination of the thermodynamic properties of liquid alloys . . . . .	40
3.1.1	Vapor pressure measurements . . . . .	40
3.1.2	Calorimetric measurements . . . . .	41
3.1.3	Electromotive force (emf) measurements . . . . .	42
3.1.4	Application to liquid Ca-Sb alloys . . . . .	43
3.2	Experimental set-up . . . . .	44
3.2.1	Preparation of the electrolyte and caps . . . . .	44
3.2.2	Preparation of the alloys . . . . .	45
3.2.3	Set-up . . . . .	47
3.3	Experimental procedure . . . . .	47
3.4	Sources of experimental errors . . . . .	49
3.4.1	Temperature deviation . . . . .	49
3.4.2	Reference electrodes . . . . .	50
3.4.3	Electrode composition . . . . .	51
3.5	Results and data analysis . . . . .	56
3.5.1	Results . . . . .	56
3.5.2	Data analysis . . . . .	59
3.5.3	Activity coefficients and thermodynamic properties of mixing .	60
3.5.4	Phase diagram . . . . .	64
3.6	Conclusions of the chapter . . . . .	66
<b>4</b>	<b>Thermodynamic modeling of Ca-Sb liquid alloys at 800 °C</b>	<b>69</b>
4.1	Association model . . . . .	70
4.1.1	Evidence of short-range order . . . . .	70
4.1.2	Model theory . . . . .	73
4.1.3	Applications of the association model . . . . .	75



4.2	Molecular interaction volume model (MIVM) . . . . .	78
4.2.1	Model theory . . . . .	78
4.2.2	Applications of the MIVM . . . . .	80
4.3	Application to Ca-Sb liquid alloys at 800 °C . . . . .	81
4.3.1	Application of the regular association model to Ca-Sb liquid alloys . . . . .	81
4.3.2	Application of the MIVM to Ca-Sb liquid alloys . . . . .	84
4.4	Comparison of the association model and the MIVM . . . . .	86
4.4.1	Quantitative comparison . . . . .	86
4.4.2	Qualitative comparison . . . . .	87
4.5	Conclusions of the chapter . . . . .	88
<b>5</b>	<b>Interaction in calcium-based liquid alloys</b>	<b>91</b>
5.1	Derivation of the interaction parameters in the MIVM . . . . .	92
5.1.1	Input parameters: molar volume and first coordination number	92
5.1.2	Output parameters: the pair-potential energy interaction parameters $B_{ij}$ . . . . .	94
5.1.3	Derivation of the interaction parameters . . . . .	95
5.2	Results . . . . .	96
5.2.1	Experimental data . . . . .	96
5.2.2	Interaction parameters . . . . .	97
5.2.3	Temperature dependence . . . . .	99
5.3	Definition of a mixing potential for liquid alloys . . . . .	101
5.4	Analysis of the trend in $V_{CaX}$ . . . . .	103
5.4.1	Identification of the Ca-X systems of interest . . . . .	103
5.4.2	Enthalpy of formation of Ca-X intermetallics . . . . .	104
5.5	Conclusions of the chapter . . . . .	107
<b>6</b>	<b>Application to Ca-Sb-Pb liquid alloys</b>	<b>111</b>
6.1	Prediction of $a_{Ca}$ in Ca-Sb-Pb alloys . . . . .	113

6.1.1	Application of the MIVM to ternary alloys . . . . .	113
6.1.2	Input parameters . . . . .	113
6.1.3	Results . . . . .	116
6.1.4	Interpretation of the results . . . . .	116
6.2	Comparison with experimental data . . . . .	118
6.2.1	Selection of Ca-Sb-Pb compositions of interest . . . . .	118
6.2.2	Experimental set-up . . . . .	118
6.2.3	Results . . . . .	119
6.2.4	Comparison with predicted values . . . . .	121
6.3	Refinement of the modeling . . . . .	121
6.3.1	Interpretation of the results at the atomistic level . . . . .	121
6.3.2	Correction of the interaction coefficients around Ca . . . . .	122
6.3.3	Interpretation of the new values for the energy parameters . . . . .	123
6.4	Prediction of the activity of calcium for other Ca-Sb-Pb alloys . . . . .	124
6.4.1	Emf measurements . . . . .	124
6.4.2	Assessment of the prediction with corrected coefficients . . . . .	125
6.4.3	Results interpretation . . . . .	127
6.5	Conclusions of the chapter . . . . .	128
<b>7</b>	<b>Conclusion</b> . . . . .	<b>131</b>
7.1	Summary . . . . .	131
7.1.1	Main results . . . . .	131
7.1.2	Application to Ca-based liquid metal batteries . . . . .	132
7.2	Contributions . . . . .	134
7.2.1	Application of the MIVM for liquid alloys exhibiting short- range order . . . . .	134
7.2.2	Definition of a new potential of mixing for liquid alloys . . . . .	134
7.2.3	Short-range order and stable intermetallics . . . . .	135
7.3	Future work . . . . .	136

7.3.1	Ternary systems . . . . .	136
7.3.2	Investigation of the Ca-based liquid metal batteries . . . . .	137
7.4	Perspectives . . . . .	139
<b>A</b>	<b>Standard operating procedure for the emf Ca-Sb cell preparation</b>	<b>141</b>
A.1	Preparation of the CaF <sub>2</sub> electrolyte and caps . . . . .	141
A.1.1	Safety precautions and personal protective equipment . . . . .	141
A.1.2	Equipment and materials . . . . .	141
A.1.3	Operating procedure . . . . .	142
A.2	Preparation of the Ca-Sb samples . . . . .	144
A.2.1	Safety precautions and personal protective equipment . . . . .	144
A.2.2	Equipment and materials . . . . .	144
A.2.3	Operating procedure . . . . .	144
A.3	Assembly . . . . .	146
A.3.1	Safety precautions and personal protective equipment . . . . .	146
A.3.2	Equipment and materials . . . . .	146
A.3.3	Operating procedure . . . . .	147
<b>B</b>	<b>Algorithms for the determination of the MIVM coefficients of Ca-Sn alloys at 800 °C</b>	<b>149</b>
B.1	Coefficients determination via error minimization algorithm . . . . .	149
B.2	Coefficients determination using partial differentials . . . . .	154
B.3	Conclusion . . . . .	157



# List of Figures

2-1	Schematic diagram of a thermally regenerative galvanic cell system [19]	26
2-2	Schematic of a closed Na  Bi cell with molten salt electrolyte [19]	26
2-3	Sectioned Mg  Sb liquid metal battery after operation at 700 °C. The cell was filled with epoxy prior to sectioning. [17]	27
2-4	Schematic of the charge and discharge mechanism in a A  B liquid metal battery	28
2-5	Installed storage capacity of storage technologies as a function of cost [14]	31
2-6	Phase diagrams of Ca-Bi, Ca-Pb, Ca-Sb, Ca-Sn systems from ASM international	34
3-1	Partial molar Gibbs free energy of Ca in binary alloys at 800°C measured by coulometric titration by Delcet [23]	43
3-2	Experimental set-up for emf measurements	45
3-3	Alloys of interest for the emf measurements, with the temperature range of the test	46
3-4	Preparation of the experimental set-up, in the glovebox, before enclosure in the test vessel	47
3-5	Temperature and emf measurements over time of an experiment Ca(s) CaF <sub>2</sub>  Ca-Sb cell	49
3-6	Temperature of the wells vs. measured temperature	50

3-7	Emf measured between 2 Ca REs, in a $\text{Ca(s)} \text{CaF}_2 \text{Ca-Sb}$ cell, error bar corresponds to the variation of the signal at equilibrium over a 30 min duration . . . . .	51
3-8	Back-scattered image of $x_{\text{Ca}} = 0.05$ Ca-Sb alloy obtained using a JSM-5910 SEM . . . . .	53
3-9	Scan of $x_{\text{Ca}} = 0.05$ Ca-Sb alloy obtained using a PANalytical X'pert Pro Multipurpose Diffractometer in 90 min . . . . .	53
3-10	Back-scattered image of $x_{\text{Ca}} = 0.55$ Ca-Sb alloy obtained using a ZEISS 1550VP Field Emission SEM . . . . .	55
3-11	Back-scattered image of $x_{\text{Ca}} = 0.63$ Ca-Sb alloy obtained using a ZEISS 1550VP Field Emission SEM . . . . .	55
3-12	Emf vs. temperature data for $\text{Ca(s)} \text{CaF}_2 \text{Ca-Sb}$ cells between 500 °C and 830 °C . . . . .	57
3-13	Emf vs. Ca concentration in Ca-Sb alloy for $\text{Ca(s)} \text{CaF}_2 \text{Ca-Sb}$ cells at 700 °C . . . . .	58
3-14	Measured partial molar Gibbs free energy vs. Ca concentration of calcium in Ca-Sb alloys at 800 °C compared with the results from Delcet [23] and Bouhajib [11] . . . . .	60
3-15	Activities of Ca and Sb vs. Ca concentration in Ca-Sb alloys at 800 °C vs. Ca(bcc) and Sb(l) (data in Table 3.3) . . . . .	62
3-16	$\Delta H$ , $\Delta G$ and $\Delta S$ vs. Ca concentration of Ca-Sb alloys at 800 °C vs. Ca(l) and Sb(l) (data in Table 3.3) . . . . .	64
3-17	Liquidus and transition temperatures from emf and DTA measurements [49, 12] on Ca-Sb phase diagram [53] (data in Table 3.4) . . . .	66
4-1	Thermodynamic properties of mixing of Sn-Te and Li-Pb alloys, modeled by Sommer using the association model [70], and corresponding phase diagrams from ASM international . . . . .	71
4-2	Ca-Mg: a system for which the minimum in the entropy of mixing does not correspond to the composition of an intermetallic . . . . .	72

4-3	Total structure factor $S(q)$ for liquid Na-Sn alloys, from neutron diffraction measurements at different compositions 25 °C above the liquidus temperature [3] . . . . .	72
4-4	Schematic of an A-B melt forming a C associate according to the associate model . . . . .	73
4-5	Thermodynamic properties of compound-forming alloys, modeled by Sommer using the association model [70] . . . . .	77
4-6	Schematic of an $i - j$ melt according to the MIVM: two types of hypothetical fluids are present in solution, which depend on the center atom considered. . . . .	79
4-7	Thermodynamic properties of mixing of Ca-Sb liquid alloys at 1078 K, solid points: experimental points; line: calculated using the association model assuming the presence of a CaSb associate [11] . . . . .	82
4-8	Enthalpy and entropy of mixing of Ca-Sb liquid alloys vs. Ca concentration at 800 °C (reference Sb(l) and Ca(l)) . . . . .	83
4-9	Composition of the ternary melt at 800 °C using $s_{II}$ . . . . .	84
4-10	Activity of Ca vs. Ca concentration in Ca-Sb liquid alloys at 800 °C, with experimental error, (reference Sb(l) and Ca(bcc)) . . . . .	86
4-11	The variation of Ca and Sb environments vs. Ca concentration in Ca-Sb liquid alloys at 800 °C . . . . .	87
5-1	$Z$ (shaded area) corresponds to the integral of the first peak of the radial distribution function (r.d.f), represented here in a typical case [34] . . . . .	93
5-2	$err$ for Ca-Sn liquid alloys at 800 °C (min for $B_{CaSn} = 1.4587$ and $B_{SnCa} = 5.9444$ ) . . . . .	96
5-3	Ca activity in diverse Ca-X liquid alloys, experimental data represented by the empty symbols (Ca-Mg from [48], Ca-Zn from [25], Ca-Ag and Ca-In from [24], Ca-Tl from [23]), data modeled by the MIVM represented by the solid lines . . . . .	98

5-4	Ca activity in diverse Ca-X liquid alloys at different temperatures, experimental data represented by the empty symbols (Ca-Bi from [23] (stars) and [39] (squares), Ca-Sb from [57], Ca-Pb from [23] (squares) and [27] (diamond)), data modeled by the MIVM represented by the solid lines . . . . .	100
5-5	Ranking of the strength of interaction in liquid Ca-X alloys . . . . .	103
5-6	Periodic chart, with the elements of interest in this chapter in purple (Ca) and blue (X) . . . . .	104
5-7	Interaction in the solid vs. liquid state for Ca-X systems with high-melting intermetallics . . . . .	105
6-1	Phase diagram of Pb-Sb alloys determined by Ohtani [51] from ASM International . . . . .	112
6-2	$a_{\text{Pb}}$ in Sb-Pb liquid alloys at 700 and 800 °C, modeled by the MIVM and measured by Sebkova [66] . . . . .	115
6-3	Prediction of $a_{\text{Ca}}$ in Ca-Sb-Pb liquid alloys for fixed $r = x_{\text{Pb}}/(x_{\text{Sb}} + x_{\text{Pb}})$ ratios at 800 °C . . . . .	117
6-4	$x_{i\text{Ca}}$ : fraction of first nearest neighbors of Ca of type $i$ . . . . .	118
6-5	Emf vs. temperature data for Ca(s) CaF <sub>2</sub>  Ca-Sb-Pb cells, for $x_{\text{Pb}}/(x_{\text{Sb}} + x_{\text{Pb}}) = 0.30$ , between 500 °C and 830 °C . . . . .	120
6-6	$\epsilon_{ij} - \epsilon_{jj}$ , with $j$ central atom (in orange) and $i$ first nearest neighbor (in green) . . . . .	122
6-7	Emf vs. temperature data for Ca(s) CaF <sub>2</sub>  Ca-Sb-Pb cells, between 500 °C and 830 °C, $r = x_{\text{Pb}}/(x_{\text{Sb}} + x_{\text{Pb}})$ . . . . .	125
6-8	Liquidus temperature of Ca-Sb-Pb alloys. Experimental data obtained through this work represented by the black points . . . . .	126



6-9	$a_{Ca}$ in Ca-Sb-Pb liquid alloys at 800 °C for fixed $r = x_{Pb}/(x_{Sb} + x_{Pb})$ ratios. The lines represent the data predicted by the MIVM after correction of the coefficients corresponding to the first nearest neighbors of Ca, and the squares represent the experimental data measured by emf. The data for Ca-Pb is from Delcet [23], the other datapoints were obtained from this work. . . . .	128
7-1	Melting temperature as a function of enthalpy of formation for the B2 phases CuZn (+), FeAl (#), CoAl (x), NiAl (*), and for the L1 phase TiAl (o) [64] . . . . .	135
A-1	Mini-lathe configuration for ductile sample machining . . . . .	145
A-2	Carrier preparation in open air . . . . .	148
A-3	Final assembly inside the Ar-filled glovebox, <1 ppm O <sub>2</sub> , < 0.1 ppm H <sub>2</sub> O 148	
B-1	MuPAD algorithm 1 . . . . .	149
B-1	MuPAD algorithm 1 (cont.) . . . . .	150
B-1	MuPAD algorithm 1 (cont.) . . . . .	151
B-1	MuPAD algorithm 1 (cont.) . . . . .	152
B-1	MuPAD algorithm 1 (cont.) . . . . .	153
B-2	MuPAD algorithm 2 . . . . .	154
B-2	MuPAD algorithm 2 (cont.) . . . . .	155
B-2	MuPAD algorithm 2 (cont.) . . . . .	156
B-2	MuPAD algorithm 2 (cont.) . . . . .	157



# List of Tables

2.1	Theoretical OCVs of A  Sn LMBs fully charged and fully discharged, calculated from activity measurements . . . . .	32
2.2	Theoretical voltages of Ca  X LMBs for $x_{\text{Ca}} = 0.1$ in the positive electrode, calculated from activity measurements . . . . .	33
3.1	Partial molar enthalpy and entropy of calcium in Ca-Sb alloys vs. Ca(s) determined from the linear fit of the experimental data (T in K), with the temperature range over which the fit is valid . . . . .	61
3.2	Emf (in V) measured vs. Ca(s) as a function of temperature (in K) non linear fits: $E = a + bT + cT \ln(T)$ . . . . .	61
3.3	Activities of Ca (with the measured standard deviation) and Sb vs. Ca(s) and Sb(l), and enthalpy and entropy of mixing vs. Ca(l) and Sb(l) at 800 °C in Ca-Sb alloys . . . . .	63
3.4	Liquidus temperatures of Ca-Sb alloys found by intersecting the emf fitting lines . . . . .	65
4.1	Enthalpy and entropy of formation of CaSb <sub>2</sub> and interaction coefficients found for each expression of the configurational entropy at 800 °C . . .	83
4.2	Input parameters in the MIVM: molar volume and atomic first coordination number . . . . .	84
4.3	Experimental and modeled activities of Ca in Ca-Sb alloys at 800 °C and corresponding emf and $\Delta\bar{G}_{\text{Ca}}$ difference . . . . .	85

4.4	Experimental and modeled activities of Ca vs. Ca(bcc) in Ca-Sb alloys at 800 °C via the regular association model and corresponding emf and $\Delta\bar{G}_{\text{Ca}}$ error . . . . .	88
5.1	Input parameters for MIVM [34, 77] . . . . .	94
5.2	Interaction parameters of Ca-X liquid alloys . . . . .	98
5.3	Temperature dependence of the interaction parameters in Ca-X liquid alloys . . . . .	101
5.4	Potential of mixing of liquid Ca-X alloys . . . . .	103
5.5	Standard enthalpy of formation of intermetallics in Ca-X ordered systems	106
5.6	Experimental vs. modeled by the MIVM $a_{\text{Ca}}$ . . . . .	109
5.7	Experimental vs. modeled by the MIVM $a_{\text{Ca}}$ . . . . .	110
6.1	Experimental vs. modeled by the MIVM $a_{\text{Pb}}$ in Pb-Sb liquid alloys .	114
6.2	$\epsilon_{ij} - \epsilon_{jj} = -kT \ln B_{ij}$ (eV) . . . . .	115
6.3	Prediction of $a_{\text{Ca}}$ at 800 °C in Ca-Sb-Pb liquid alloys using the MIVM	117
6.4	Liquidus temperatures of Ca-Sb and Ca-(30Pb70Sb) alloys found by intersecting emf fitting lines . . . . .	120
6.5	Emf in Ca(s) CaF <sub>2</sub>  Ca-(30Pb70Sb)(l) predicted by the MIVM, and measured by emf . . . . .	121
6.6	$\epsilon_{ij} - \epsilon_{jj} = -kT \ln B_{ij}$ (eV). The parameters in black were derived from modeling of the binary systems, while the parameters in green were optimized in the ternary system . . . . .	123
6.7	Emf in Ca(s) CaF <sub>2</sub>  Ca-(30Pb70Sb)(l) measured by emf, and modeled after optimization of the energy levels of the first nearest neighbors of Ca . . . . .	123
6.8	Liquidus temperatures of Ca-Sb-Pb alloys found by intersecting emf fitting lines . . . . .	126
6.9	Emf in Ca(s) CaF <sub>2</sub>  Ca-Pb-Sb(l) measured by emf, and predicted by the MIVM, using the updated interaction coefficients . . . . .	127

# Chapter 1

## List of constants, symbols, and acronyms

### 1.1 Constants

	definition	value
$F$	Faraday's constant	96 485 C/mol
$k$	Boltzmann's constant	$8.617 \times 10^{-5}$ eV/K
$N_a$	Avogadro's number	$6.022 \times 10^{23}$
$R$	gas constant	8.314 J/mol/K
$Z_c$	close packed coordination number	12

## 1.2 Symbols

	definition	unit
$a$	activity	
$a_{Ca}$	activity of calcium in Ca-X alloys	
$\alpha_V$	thermal coefficient of expansion	$K^{-1}$
$B_{ij}$	pair-potential energy interaction parameter of $i$ around $j$ in the MIVM	
$\Delta G$	Gibbs free energy of mixing	J/mol
$\Delta \bar{G}$	partial molar Gibbs free energy	J/mol
$\Delta H$	enthalpy of mixing	J/mol
$\Delta \bar{H}$	partial molar enthalpy	J/mol
$\Delta H^0$	enthalpy of formation of associate in regular association model	J/mol
$\Delta H_f^0$	standard enthalpy of formation at 298K	J/mol
$\Delta H_{fus}$	enthalpy of melting	J/mol
$\Delta S$	entropy of mixing	J/mol
$\Delta \bar{S}$	partial molar entropy	J/mol
$\Delta S^0$	entropy of formation of associate in regular association model	J/mol
$E$	emf vs. Ca(s)	V
$\epsilon_{ij}$	energy of a $j$ atom surrounded by an $i$ atom	eV
$\epsilon_p$	mixing potential energy in the MIVM	eV
$\Phi$	volume fraction	
$g$	pair distribution function	
$\gamma$	activity coefficient	
$G_m^E$	excess Gibbs free energy of mixing	J/mol
$\Lambda$	Debye length	m
$N$	number of particles (free atoms or associates) per mole of alloy in the association model	
$p_i^0$	vapor pressure of pure $i$	Pa
$p_i$	partial vapor pressure of $i$ in a mixture	Pa
$Q$	partition function in canonical ensemble	
$Q_p$	configurational partition function in canonical ensemble	
$r_0$	beginning value of the radial distance	m
$r_m$	first peak value of the radial distance	m
$s$	configurational entropy	J/mol/K
$T_{liq}$	liquidus temperature	K
$T_m$	melting point	K
$V_{ij}$	potential of mixing of $i - j$ liquid alloy	eV
$V_{fus}$	molar volume at the melting point	$m^3/mol$
$V_m$	molar volume	$m^3/mol$
$W_{ij}$	bond energy of $i - j$ bond	eV
$\omega_{ij}$	interaction coefficient between $i$ and $j$ in the regular association model	J/mol

	definition	unit
$x$	molar fraction	
$x_{ij}$	molar fraction of $i$ first nearest neighbors of $j$ in the MIVM	
$X$	molar fraction in compound forming liquid alloy in association model, considering associates as separate species	
$z$	charge number	
$Z$	first coordination number	
$Z_{ij}$	the number of $j$ atoms surrounding the central $i$ atom in the MIVM	
	phase boundary	

### 1.3 Acronyms and abbreviations

	definition
ANL	Argonne National Laboratory
BNL	Brookhaven National Laboratory
BSE	back scattered electrons
bcc	body centered cubic
DTA	differential thermal analysis
emf	electromotive force
EDS	energy dispersive spectroscopy
g	gas phase
ID	inner diameter
l	liquid phase
LMB	liquid metal battery
MIVM	molecular interaction volume model
OCV	open circuit voltage
OD	outer diameter
PVA	polyvinyl alcohol
r.d.f.	radial distribution function
RE	reference electrode
s	solid phase
SS	stainless steel
WDS	wavelength dispersive spectroscopy
WE	working electrode
XRD	X-ray diffraction





# Chapter 2

## Introduction

The objective of this work is to investigate the thermodynamic properties of Ca-based liquid alloys, in particular to identify promising metallic systems to use as positive electrodes in Ca-based liquid metal batteries.

### 2.1 Liquid metal batteries

#### 2.1.1 From waste heat recovery to grid-scale storage

Systems with liquid metal electrodes and a molten salt electrolyte were first investigated at the Argonne National Laboratory (ANL) by Cairns et al. in the 1960s and 1970s. The original aim of these galvanic cells with fused-salt electrolytes, which were thermally regenerative cells, was to use the heat generated by a nuclear reactor to produce electric energy. During the charge, the more volatile anode metal A from the A-C cathode alloy vaporized due to the heat and migrated to the anode A (schematic in Figure 2-1). During the discharge, metal A from the anode alloyed with the metal C in the cathode by electrochemical reaction producing electricity. A and C were chosen such that A was much more volatile than C, and the Gibbs free energy of formation of the AC alloy was high. Demonstrated chemistries included Na||Bi, with impressive lifespan (17 months) at current densities above 1 A/cm<sup>2</sup> [19].

Later, the battery design evolved (Figure 2-2) for use in mobile applications with

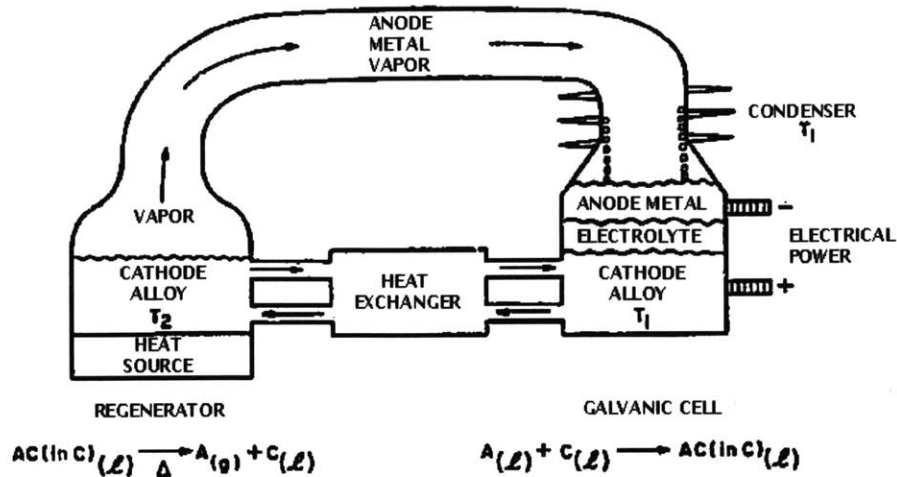


Figure 2-1: Schematic diagram of a thermally regenerative galvanic cell system [19]

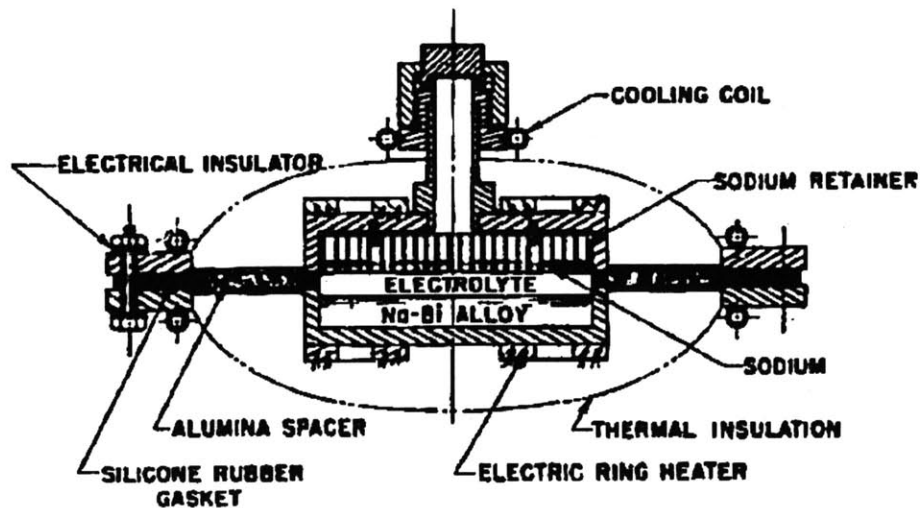


Figure 2-2: Schematic of a closed Na||Bi cell with molten salt electrolyte [19]

the advent of electric vehicles [20], charging the system with electricity instead of heat. Eventually, the high temperature that was demanded by these cells limited their application in electric vehicles, and the research ended without commercialization.

With use for grid-scale storage in mind, the concept of batteries with all liquid components (two liquid metals sandwiching a layer of molten salt), was revisited by Sadoway and Bradwell [14, 15], inspired by the success of the Hall-Héroult cell in the aluminum industry. Targeting a low cost demanding application, Bradwell et al. demonstrated the operation of the first Mg||Sb liquid metal battery [17], with materials much cheaper than those used by Cairns et al.. The configuration chosen

by Bradwell et al. is visible in Figure 2-3 on a post-experiment cross-section of such a battery.

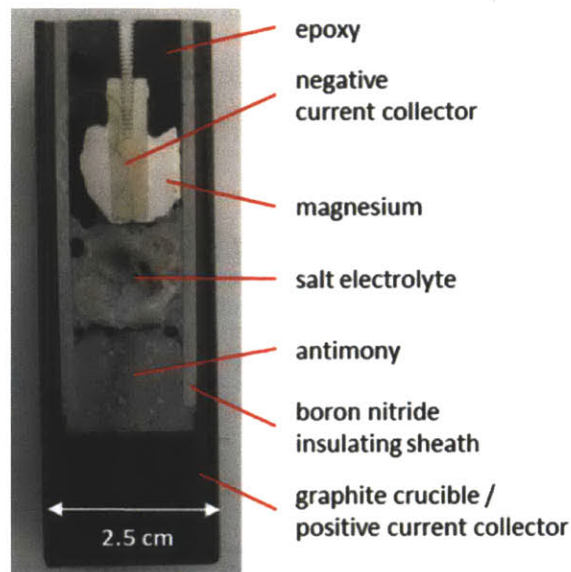


Figure 2-3: Sectioned Mg||Sb liquid metal battery after operation at 700 °C. The cell was filled with epoxy prior to sectioning. [17]

### 2.1.2 Unique characteristics of liquid metal batteries

While liquid metal batteries may not have been appropriate for energy storage in electric vehicles, they are very attractive for grid-scale energy storage [16]:

- Liquid-liquid interfaces can be challenging to stabilize, disqualifying their use in portable applications. However, liquid-liquid interfaces allow the battery to withstand high current densities, such as 1 A/cm<sup>2</sup> in the case of Na||Bi cells [19]. The current density can therefore be adapted depending on high or low energy generation. This is particularly interesting to store intermittent energies, such as solar or wind energy.

- The temperature required to keep the layers liquid (from 500 to 800 °C depending on the materials used) would again be an issue for portable storage, but not for stationary storage.

### 2.1.3 Operating principles of liquid metal batteries

Liquid metal batteries come with different names and use different materials; however, they all work similarly. A schematic in Figure 2-4 shows how the battery works during charge and discharge. As the name indicates, liquid metal batteries are composed of three liquid layers, that self segregate due to the difference in density. Two liquid metals A and B are separated by a molten salt electrolyte layer that conducts  $A^{z+}$  cations.

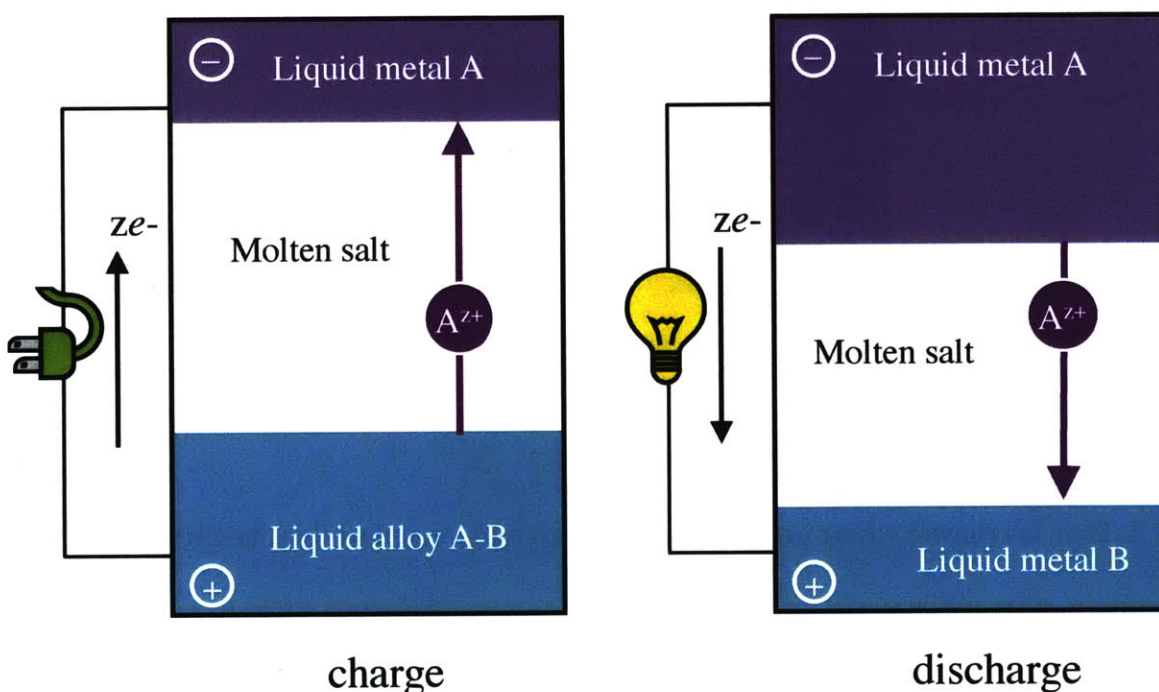
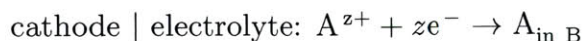


Figure 2-4: Schematic of the charge and discharge mechanism in a A||B liquid metal battery

During the discharge, A is oxidized at the anode into  $A^{z+}$ , while the electrons are released into the external circuit.  $A^{z+}$  migrates through the electrolyte from the anode to the cathode. At the cathode | electrolyte interface  $A^{z+}$  is reduced to A, which alloys with B at the cathode, according to:



The driving force for the electrochemical reaction is the difference in electrochemical potential of A between pure A and A alloyed with B. Indeed, the electrochemical

potential of A at each electrode can be expressed via the Nernst equation:

$$E_{\text{cathode}} = E_{\text{A}}^0 + \frac{RT}{zF} \ln \left( \frac{a_{\text{A}^{z+}}}{a_{\text{A,cathode}}} \right) \quad (2.1)$$

$$E_{\text{anode}} = E_{\text{A}}^0 + \frac{RT}{zF} \ln \left( \frac{a_{\text{A}^{z+}}}{a_{\text{A,anode}}} \right) \quad (2.2)$$

The standard state is defined as the state for which A is the most stable at the temperature and pressure considered for the operation. The activity of pure A in the anode is 1 by convention. The activity of  $\text{A}^{z+}$  in the bulk electrolyte,  $a_{\text{A}^{z+}}$ , is the same in the two expressions. The standard electrochemical potential of pure A,  $E_{\text{A}}^0$ , is also the same in the two expressions. Therefore, the difference of electric potential between the two electrodes, which is also the OCV of the battery, can be expressed as:

$$\Delta E = -\frac{RT}{zF} \ln a_{\text{A}} = -zF \Delta \bar{G}_{\text{A}} \quad (2.3)$$

where  $a_{\text{A}}$  the activity of A in B, and  $\Delta \bar{G}_{\text{A}}$  the partial Gibbs free energy of A in B. The theoretical discharge curve of a A||B liquid metal battery can therefore be computed from the knowledge of the activity of A in B.

During charge, the reverse reactions occur, consuming energy to electrochemically separate the A-B alloy into its constituents A at the negative electrode and B at the positive electrode.

## 2.2 Selection of the materials of interest

Many materials are involved in the design of a liquid metal battery: the active components, which are responsible for the energy storage, such as the electrodes; and passive components, such as the electrolyte, and the positive and negative current collectors, which let charge flow through them but ideally do not react with the active materials.

The choice of these passive materials is crucial to design an efficient battery. They

might indeed react with the electrodes, through reactions such as the dissolution of the electrodes in the electrolyte and corrosion of the current collectors. However, this choice cannot be tackled until the electrodes, that will store the energy, have been determined, since the reactivity, or not, of these ideally passive components will depend on the active components they would interact with. Therefore, the first step to design a liquid metal battery is the choice of the electrodes.

### 2.2.1 Selection criteria for the electrodes

To work as a liquid metal battery, the electrodes must possess the following characteristics: (1) be liquid, (2) be metals, (3) provide a high voltage, and (4) have a density difference high enough to self-segregate.

Criteria can be specified as follow:

(1) The melting temperature should be below 1000 °C to operate the liquid metal battery at a reasonable temperature.

(2) The conductivity of the materials should be high enough ( $> 10^5$  S/m, i.e. metals or semimetals) to avoid the addition of a complicated electrically conductive matrix structure in the electrodes, which would be difficult to scale up.

(3) The OCV of an A||B liquid metal battery should be as large as possible. It is directly related to the activity coefficient of A in A-B alloy, as demonstrated in the previous section. This translates therefore into low activity coefficients of A in A-B alloy.

(4) From the knowledge in the aluminum industry [28], the difference between the positive electrode and the electrolyte on one side, and the negative electrode and electrolyte on the other side, needs to be more than 0.2 g/cm<sup>3</sup> to allow the phases to separate.

Additional characteristics need to be met to make them an interesting alternative to current technologies for grid-scale storage.

- The materials used should not be radioactive and less toxic than mercury.
- For the technology to be competitive, the materials used should be abundant and cheap. According to Bradwell [16], the capital cost of the battery should be

less than \$150 /kWh [16] to be competitive. As a comparison, the installed capacity vs. the capital cost of different battery technologies is plotted in Figure 2-5 from [14]. Today, only pumped hydro is cheaper than this \$150 /kWh figure, but its deployment is limited geographically. This means that the liquid metal battery could have a potential market for grid-scale storage, even if it were not cheaper than pumped hydro.

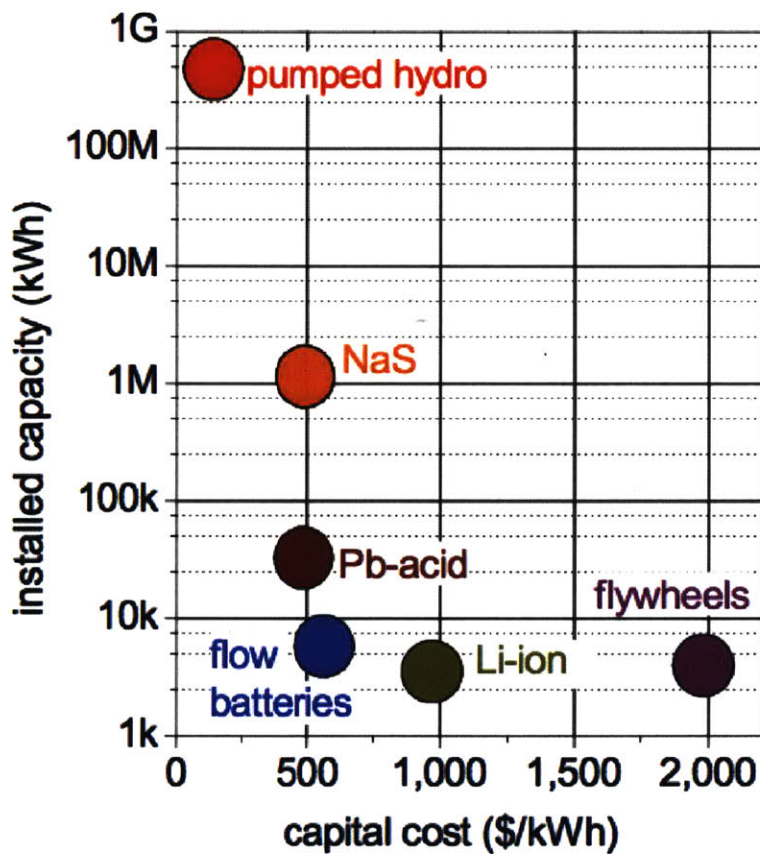


Figure 2-5: Installed storage capacity of storage technologies as a function of cost [14]

Based on these criteria, alkali and alkaline earth metals were selected as candidates for the negative electrode, while most semimetals were judged interesting for the positive electrode.

## 2.2.2 Ca-based liquid metal batteries

### Choice of calcium

Among the alkali and alkaline earth candidates for the negative electrode, Li, Na, and Ca are particularly appealing with a price below \$0.5 /mol [40]. Li and Na-based liquid metal batteries have been extensively studied by Cairns et al. at the ANL [19], leading to batteries such as Li||Sn, Li||Te, Li||Bi, Na||Sn, Na||Pb, and Na||Bi.

Ca-based liquid metal batteries have been understudied, even though the predicted values of OCV against the same positive electrode are comparable. For instance, predicted average OCVs from activity measurements for liquid metal batteries (LMB) using Sn as a positive electrode are compared in Table 2.1. It may be because Ca is much more reactive with air and moisture than metals such as Na or Li, which makes it more difficult to handle. Therefore, Ca-based liquid metal batteries were chosen as the subject of this thesis.

A	T (°C)	$\Delta E_{max}$ (V)	$\Delta E_{min}$ (V)
Li	550	0.87 [46]	0.46 [46]
Na	580	0.63 [61]	0.20 [61]
Ca	800	0.88 [23]	0.53 [23]

Table 2.1: Theoretical OCVs of A||Sn LMBs fully charged and fully discharged, calculated from activity measurements

### High-melting intermetallics

Considering Ca-based liquid metal batteries, most semimetals are of interest for the positive electrode using the criteria above. Some thermodynamic measurements are available for Ca-X systems, with X the semimetal of interest. The corresponding open circuit voltage of these Ca||X LMBs can be calculated using the Nernst equation. The data available from the literature are reported in Table 2.2. The thermodynamic data available in the literature are available only for limited ranges and only at one temperature in most cases.

Interestingly, Ca-X systems with X a semimetal show the presence of high-melting intermetallics. A few examples are given in Figure 2-6. This is the sign of a very

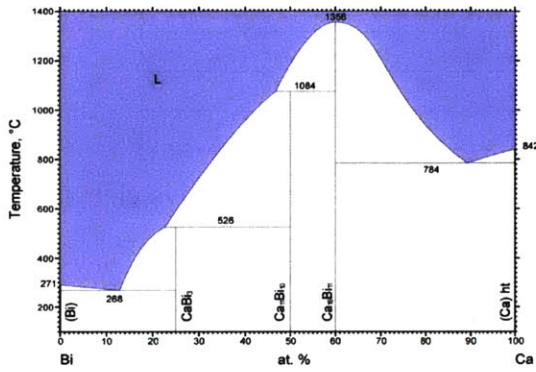


X	T (°C)	$\Delta E$ (V) for $x_{\text{Ca}} = 0.1$ in the positive electrode
Ag	800 only	0.53 [24]
Bi	800	0.87 [23, 39]
	700	0.86 [39]
	600	0.85 [39]
In	800 only	0.56 [24]
Pb	800 only	0.65 [23]
Sb	800	1.01 [23]
	805	0.67 [11]
Sn	800 only	0.71 [23]
Tl	800 only	0.58 [23]
Zn	800 only	0.39 [25]

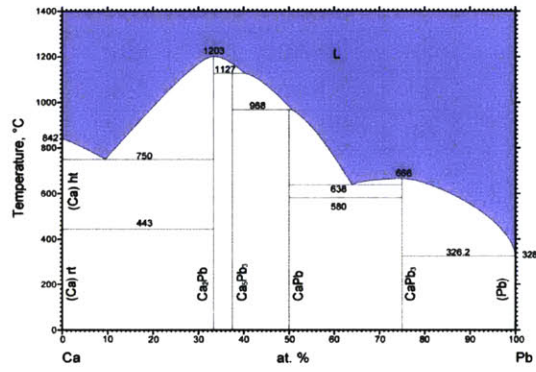
Table 2.2: Theoretical voltages of Ca||X LMBs for  $x_{\text{Ca}} = 0.1$  in the positive electrode, calculated from activity measurements

favorable mixing between Ca and X in the solid state. Intuitively, these systems should have strong interaction in the liquid state as well, and therefore be interesting to use in liquid metal batteries. Indeed, a strong interaction would mean that Ca is much more stable in contact with the semimetal than by itself, which should translate in low Ca activity and high cell voltage.

Such an example is the Ca-Sb system, which has a particularly high-melting intermetallic. Looking at the phase diagram (Figure 2-6(c)), this system might be promising since it shows strong interaction in the solid state. However, the knowledge of the phase diagram determined experimentally does not allow one to predict the properties of the liquid state and the Ca-Sb system deserves a more thorough study since there is no consensus on the thermodynamic properties of this system in the liquid state. Additionally, Sb is one of the cheapest semimetals (\$1.8 /mol [1]), and assuming an OCV of 1 V, a Ca||Sb would meet the target price [55].



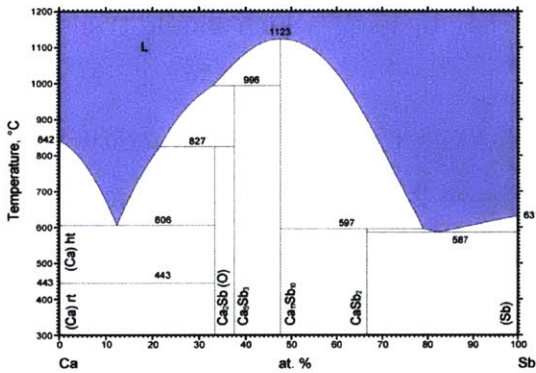
© ASM International 2009. Diagram No. 101064



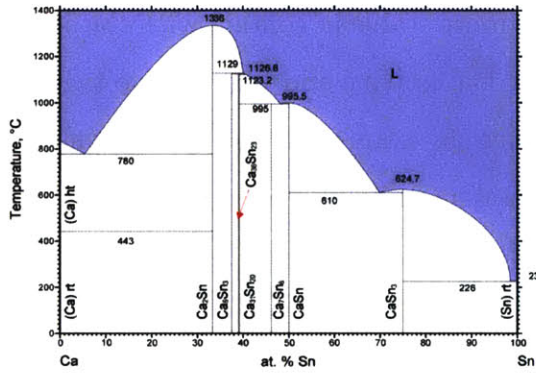
© ASM International 2005. Diagram No. 979918

(a) Ca-Bi phase diagram [50]

(b) Ca-Pb phase diagram [38]



© ASM International 2006. Diagram No. 1500429.



© ASM International 2010. Diagram No. 102651

(c) Ca-Sb phase diagram [53]

(d) Ca-Sn phase diagram [22]

Figure 2-6: Phase diagrams of Ca-Bi, Ca-Pb, Ca-Sb, Ca-Sn systems from ASM international

## 2.3 Research objectives

The importance of exploring Ca-based liquid metal batteries, as potential storage media for grid-scale applications, was demonstrated. To judge the performance of a battery, the discharge curve is usually used, since it shows the storage capabilities of the battery. The theoretical discharge curve, in particular, is crucial to evaluate the maximal performances of a potential battery, and assess the suitability of a candidate electrode over another. This theoretical discharge curve is directly related to the activity of Ca in the metal X chosen for the positive electrode, highlighting the importance of the determination of the activity of Ca in different metals X and at different temperatures.

To choose the best candidate(s) for the positive electrode of a Ca-based liquid metal battery, the thermodynamic and experimental tools necessary will need to be identified, and invented when they do not exist. To identify this (these) metals, the following research questions will need to be answered:

### 2.3.1 How can we quantify the theoretical voltage of a Ca||Sb LMB for appropriate ranges of temperature and composition?

Antimony was shown as a possible material for the positive electrode that would generate the highest voltage for a Ca||X liquid metal batteries, and be a cheap metal that would fulfill the price demand for grid-scale storage. However, data are not consistent between the different sources in the literature.

A method will therefore need to be developed to measure the activity of Ca and derive the thermodynamic properties of Ca-Sb liquid alloys. The range of interest to cycle a Ca||Sb liquid metal battery will be identified, and the properties of Ca-Sb alloys will be evaluated for a temperature range, to the opposite of a single temperature, as it is the case in the literature for most Ca-X alloys.

### **2.3.2 How can we correlate the OCV of a Ca||Sb LMB with the structure of the Ca-Sb alloys?**

To answer this question, one approach would have been to run neutron diffraction experiments, here a more fundamental approach was chosen. To understand why a metal is or is not an interesting candidate for the positive electrode of a Ca-based liquid metal battery, the thermodynamic properties of the corresponding Ca-based liquid alloys will be modeled. Indeed, a model (or several models) will help understand how the atomic structure of the alloy of interest affects the activity of Ca in the Ca-X alloy.

The example chosen is the case of antimony, since its thermodynamic properties will have been evaluated. The appropriate model(s) will have to be selected, and applied to the Ca-Sb liquid alloys, and show how Ca and Sb atoms are arranged in the liquid alloy, based on the thermodynamic data.

### **2.3.3 Are systems with high-melting intermetallics interesting to use in LMB, and if so why?**

Systems with high-melting intermetallics intuitively have strong interaction in the solid state, and might have strong interaction in the liquid state, which would be interesting for a liquid metal battery. Indeed, the more stable Ca is in the alloy, the lower the Ca activity and the greater the OCV.

To answer this question, multiple Ca-X systems with high-melting intermetallic compounds will need to be modeled, and a new parameter to characterize the interaction in the liquid alloys will need to be derived, based on the thermodynamic data, to compare the systems to one another.

The trend observed for the interaction parameter in the liquid state will have to be compared to a parameter to show the strength of the interaction for these systems in the solid state. The parameter for the solid state will also need to be selected and justified.

### 2.3.4 Can we use our thermodynamic modeling of binaries to predict the OCV of a Ca||X-Y LMB?

Until now, only pure metal positive electrodes were considered, the reason being that only thermodynamic measurements for binary Ca-X alloys were found in the literature. To which extent can the binary thermodynamic modeling help design a binary positive electrode?

An X-Y system of interest will need to be chosen, and the thermodynamic properties of Ca-X-Y will be modeled based on the thermodynamic modeling of the Ca-X, Ca-Y and X-Y systems. The prediction will have to be compared with experimental data that will be collected, and the precision of the model will be assessed and interpreted.

## 2.4 Conclusions of the chapter

The operating mechanism of A||B liquid metal batteries was explained, with A the negative electrode and B the positive electrode, underlining the direct relationship between the OCV of the battery and the activity of A in liquid A-B alloy. Therefore, the knowledge of the thermodynamic properties of liquid A-B alloys is key to select materials that will ensure a high voltage A||B LMB.

The recent development of liquid metal batteries for grid-scale storage has highlighted the lack of work on Ca-based alloys. However, the few measurements available suggest that Ca would be an interesting alternative to lithium and sodium as a negative electrode, since it would ensure an OCV as high as Li, while being much cheaper. Therefore, this thesis will focus on the materials to use as positive electrodes for Ca-based liquid metal batteries.

Sb was identified as a possibly interesting material for the positive electrode of a Ca-based LMB, but the literature lacks reproducible data for Ca-Sb liquid alloys. Partial data are available for other Ca-based liquid alloys, showing that Ca-X systems with high-melting intermetallics are more likely to ensure a high voltage Ca||X LMB.

Systematic modeling of these systems will therefore be performed, to complete the database containing the thermodynamic properties of these alloys. A binary alloy X-Y for the positive electrode will be considered, and properties of the Ca-X-Y systems will be modeled to predict the OCV of such a Ca||X-Y battery.

Ultimately, the goal is to relate the thermodynamic properties of liquid Ca-based alloys to their structure, and explain how a material X can or cannot be expected to provide a high voltage Ca||X LMB from atomistics. Beyond the application to Ca-based liquid metal batteries, this work will provide a more systematic approach to the selection of materials for liquid metal batteries.

## Chapter 3

# Thermodynamic properties of mixing of liquid calcium-antimony alloys via emf measurements

This chapter focuses on the experimental determination of the thermodynamic properties of liquid Ca-Sb alloys. The main methods that have been used in the literature to determine these properties for liquid alloys will be reviewed, and the choice of an emf method in the case of liquid Ca-Sb alloys will be justified. The experimental set-up with the materials chosen, and the experimental procedure will be described and explained. Finally, the results obtained for the entire range of compositions of Ca-Sb alloys will be presented and analyzed to calculate the activities of Ca and Sb, and the integral thermodynamic properties of mixing of liquid Ca-Sb alloys.

# 3.1 Experimental methods for the determination of the thermodynamic properties of liquid alloys

Several methods can be used to determine the thermodynamic properties of liquid alloys. This section will review these different methods, and justify the choice of emf measurements for this work.

## 3.1.1 Vapor pressure measurements

Numerous methods have been developed over the years to extract thermodynamic data from vapor pressure measurements [35]. These methods rely on the relationship between the partial vapor pressure of one component,  $p_i$ , and its activity,  $a_i$ , by  $p_i = a_i \times p_i^0$ , with  $p_i^0$  is the vapor pressure of pure component  $i$ . The vapor pressure that is measured,  $p_{tot}$ , is related to the partial vapor pressure of each one of its components via Dalton's law:

$$p_{tot} = \sum_i p_i = \sum_i a_i p_i^0 \quad (3.1)$$

To obtain the partial vapor pressure  $p_i$  from the total vapor pressure  $p_{tot}$ , the composition of the vapor must be measured or hypothesized. For instance, for liquid alloys of elements that have very different vapor pressures, the contribution of the less volatile elements can be neglected, and the total vapor pressure is equal to the vapor pressure of the more volatile element, as in the case of Ca-Mg, where Mg is much more volatile than Ca at 1010K, for  $x_{Ca} < 0.8$  [68]. Otherwise, the composition of the vapor is usually determined by mass spectroscopy and, assuming that the vapor is an ideal mixture, the partial pressure of each species can be determined by  $p_i = p_{tot} \times x_i$ .

In the case of Ca-Sb, the vapor pressures of pure Ca and Sb have the same order of magnitude: at 800 °C, the vapor pressure of antimony is 240 Pa, mainly as  $Sb_4(g)$ ,



while the vapor pressure of calcium is 106 Pa, mainly as Ca(g) [32]. Also, given the stability of the intermetallics (higher melting points than pure Ca and Sb), associates would likely form, as it has been observed for Au-Dy [30]. Therefore, the composition could only be inferred from mass spectroscopy analysis. However, the reactivity of calcium with most ceramics makes it particularly difficult to find an apparatus equipped with a mass spectrometer that would not react with the vapor, in which case its measured composition could be inaccurate.

### 3.1.2 Calorimetric measurements

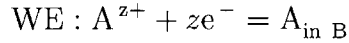
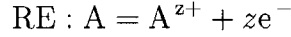
For high temperature work, the most used calorimetric method is the direct drop method: pure solid A is dropped in the calorimeter containing a bath of pure B or liquid alloy  $A_xB_y$  [41]. With knowledge of the temperature of the calorimeter, the partial enthalpy of formation of A can be calculated from measuring the heat of reaction. Indeed, since the quantity of A added is much smaller than the quantity of the bath, the heat of reaction measured represents the heat of the reaction  $A(s, T_i) \rightarrow A(\text{alloy}, T_f)$ .

An important requirement for the use of calorimetric methods is the identification of a non-reactive container and the calibration of its properties. Indeed, the calorimetry of the sample and of the container cannot be separated, and to measure the partial enthalpy of formation of A in A-B alloys, the alloying reaction must be the only one happening. This is particularly challenging in the case of Ca-Sb alloys since Sb alloys with most metals that do not alloy with Ca. One of the few metals it doesn't alloy with is tungsten, particularly challenging to machine. Additionally, Ca reacts with most common ceramics such as alumina or quartz since CaO is particularly stable.

Bouhajib [10] reported using a drop calorimetry method to measure the partial enthalpy of Ca and the enthalpy of mixing of Ca-Sb liquid alloys at 805 °C and  $x_{Ca} < 0.6$ . The calorimeter used was an in-house retrofitted Calvet calorimeter, with alumina crucibles.

### 3.1.3 Electromotive force (emf) measurements

Emf measurements are usually performed in a cell of the type  $A | A^{z+}$ -based electrolyte  $| A$ -B, where A is the reference electrode (RE) and A-B the working electrode (WE). The overall cell reaction is the alloying of A in B according to the following two steps, which correspond to the half reactions at the electrodes:



At equilibrium, the difference of potential measured between the reference electrode and the working electrode is related to the activity of A in the A-B alloy by the Nernst equation  $E = -\frac{RT}{zF} \ln a_{A_{\text{in B}}}$ . The electrolyte should contain  $A^{z+}$  and A should be present in both electrodes to have an equilibrium at each interface. If pure A is not an option for the RE, an A-based alloy of known A activity can be used. More details about the use of solid state galvanic cells are available in Chapter 9.2 of [65].

The choice of the electrolyte is crucial so that it does not affect the emf measured. The electronic conduction needs to be negligible or calibrated to obtain a correct value for the activity of A [25]. The electrolyte can be a molten salt or a solid electrolyte.

Emf measurements can then be broken down into two subcategories:

- emf measurements at a constant composition for a range of temperatures;
- emf measurements at a constant temperature for a range of compositions using coulometric titration. In this case, A from the  $A^{z+}$  conductor is deposited onto B and the composition of the A-B alloy (working electrode) varies with time, according to the current density used. Since A needs to diffuse through the electrolyte to be at equilibrium at the interfaces, these measurements can take several days. This method is mostly used with liquid electrolytes, since the diffusion is much faster. Otherwise, the solid electrolyte needs to be thin.

In the case of Ca-based alloys, Delcet et al. [58] used a  $\text{CaF}_2$  single crystal electrolyte, while Fray et al. [27] preferred the use of solid calcium magnetoplumbite.

Kim et al. [39] reported that the solubility of Ca in Ca-based molten salts was too high to allow reproducible measurements with a liquid electrolyte.

Delcet et al. [23] used a coulometric titration to evaluate the activity coefficient of calcium in calcium-antimony alloys at 800 °C for  $x_{Ca} < 0.6$ , using a Ca-Bi (1) reference electrode of known Ca activity, and solid  $CaF_2$  as electrolyte. The measured partial molar Gibbs free energy of Ca in Ca-X alloys, related to the activity of Ca in Ca-X alloys by  $\Delta\bar{G}_{Ca} = RT \ln(a_{Ca})$  (more details in Chapter 2), is reported in Figure 3-1.

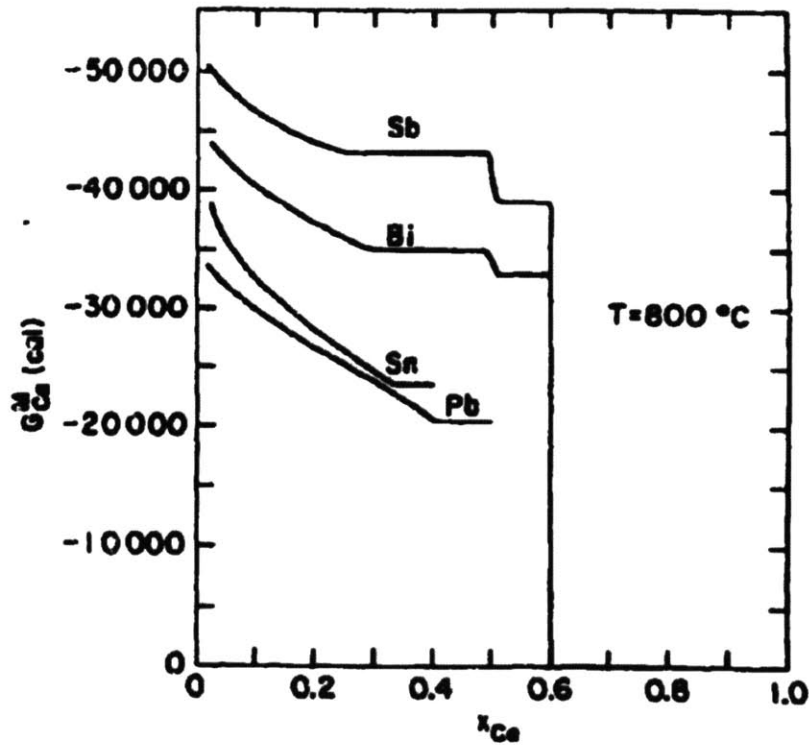


Figure 3-1: Partial molar Gibbs free energy of Ca in binary alloys at 800°C measured by coulometric titration by Delcet [23]

### 3.1.4 Application to liquid Ca-Sb alloys

The activity of Ca in Ca-Sb alloys was measured at two close temperatures (800 [23] and 805 °C [10]) for  $x_{Ca} < 0.6$  using emf measurements via coulometric titration [23], and a drop calorimetry technique [10]. However, the results from these two datasets differ substantially: Bouhajib obtained -129 and -119 kJ/mol for the partial Gibbs free energy of calcium at  $x_{Ca} = 0.1$  and 0.2 respectively [11] while Delcet measured

- 195 and -185 kJ/mol [23]. Depending on the dataset, this would translate into an OCV of 1 V (Delcet) vs. 0.6 V (Bouhajib) for a Ca||Sb battery with  $x_{\text{Ca}} = 0.1$  in the positive electrode at 800 °C.

To evaluate the suitability of Sb as a positive electrode in a Ca-based liquid metal battery, the activity of Ca needs to be evaluated and its temperature dependence to be quantified to determine the cycling range and operating temperature of a Ca||Sb LMB. The advantage of the emf measurement at constant composition is that it will provide this information, while revealing clearly the phase transformations of the Ca-Sb alloy, and in particular its liquidus. Therefore, choosing an emf method with constant composition seems appropriate to obtain, in particular, all the information necessary to evaluate the theoretical discharge curve of a Ca||Sb LMB.

Based on the review of the different methods that could have been used, the main challenge was to find a non-reactive container for the Ca-Sb alloys. A sintered  $\text{CaF}_2$  electrolyte, which can be machined to accommodate wells that will hold the liquid Ca-Sb alloys, solves the problem by avoiding the introduction of an additional material to contain the alloys.

## 3.2 Experimental set-up

Standard operating procedures for the preparation of the electrolyte, caps, alloys and assembling of the set-up are available in the Appendix A. The main points are described here as well.

### 3.2.1 Preparation of the electrolyte and caps

To prepare the custom-shaped  $\text{CaF}_2$  solid electrolyte, 500 g of  $\text{CaF}_2$  (Fischer Scientific, Stock No. C89-500) and 20 g of polyvinyl alcohol (Sigma Aldrich, Stock No. 341584) were mixed with 150 mL of deionized water. After drying for 48 h in air, 150 g of powder ( $< 850 \mu\text{m}$ ) was pressed into a pellet 75 mm in diameter using 30 MPa of uniaxial pressure for 10 minutes. As shown on the right hand side of Figure 3-2, 6 wells were machined into the  $\text{CaF}_2$  electrolyte pellet to contain 2 reference electrodes

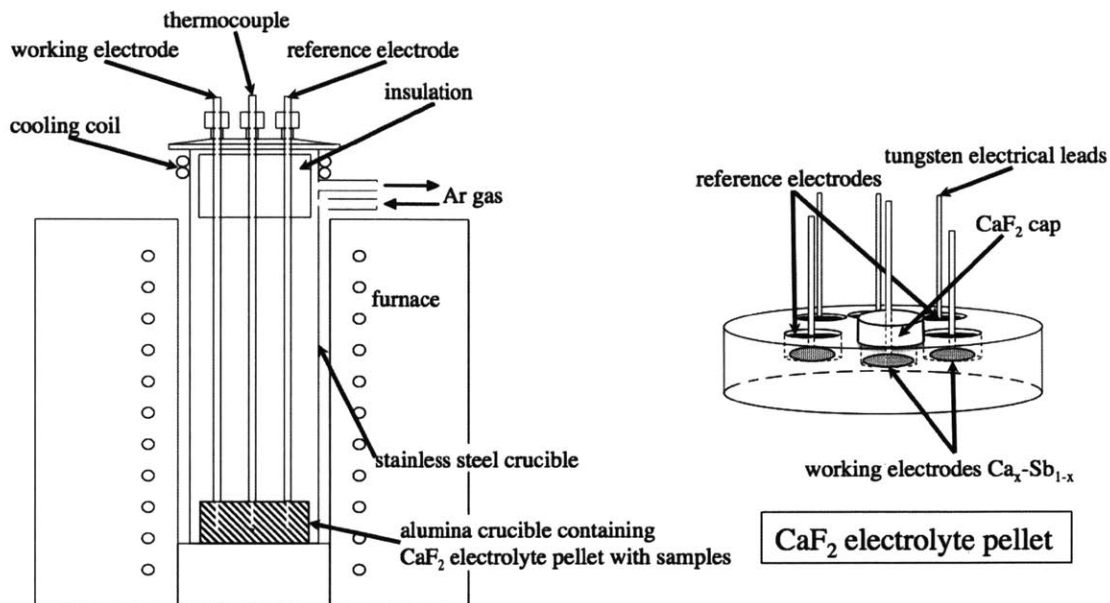


Figure 3-2: Experimental set-up for emf measurements

(RE) and 4 working electrodes (WE), the latter consisting of the Ca-Sb alloys of interest. An additional well is present in the center for a thermocouple. Similarly, 6 g of powder was pressed successively into 19 mm diameter pellets for 1.5 min at 94 MPa to produce  $\text{CaF}_2$  pellets (caps), and a hole of 1.1 mm in diameter was drilled in the center. The electrolyte and caps were then fired in ambient environment for 12 h at 120 °C, 8 h at 550 °C, and 4 h at 1000 °C to remove moisture, burn out the binder, and sinter, respectively. The final pellets were white in color with approximately 98% theoretical density.

### 3.2.2 Preparation of the alloys

The alloys probed through this set of emf measurements are identified in Figure 3-3, on the phase diagram [53].

For most alloys, the calcium (99.99% metals basis, Sigma Aldrich, Stock No. 441872) and the antimony (99.999% metals basis, Alfa Aesar, Stock No. 11348) were weighed out in an Ar-filled glovebox ( $< 0.1$  ppm  $\text{O}_2$ ,  $< 0.1$  ppm  $\text{H}_2\text{O}$ ), then arc melted using a MAM1 (Edmund Bühler GmbH). These samples were machined into cylinders 3-5 mm high and 9 mm in diameter, and a hole was drilled to accommodate

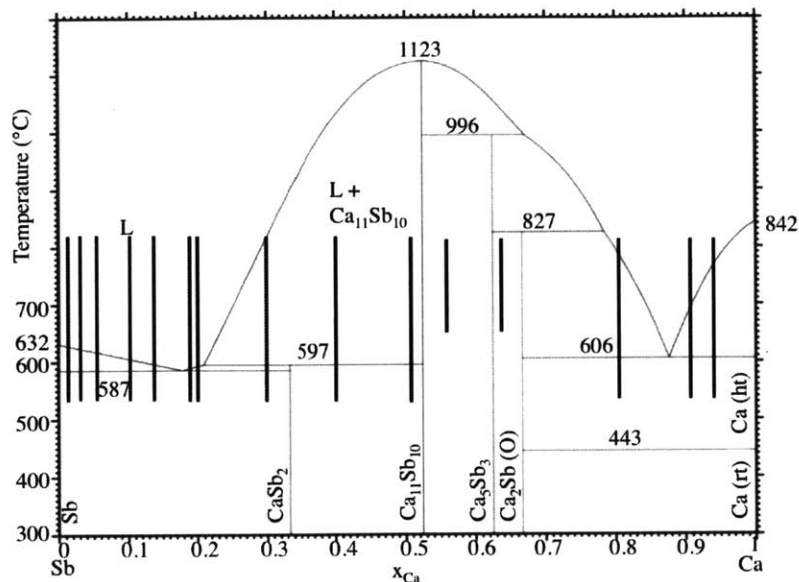


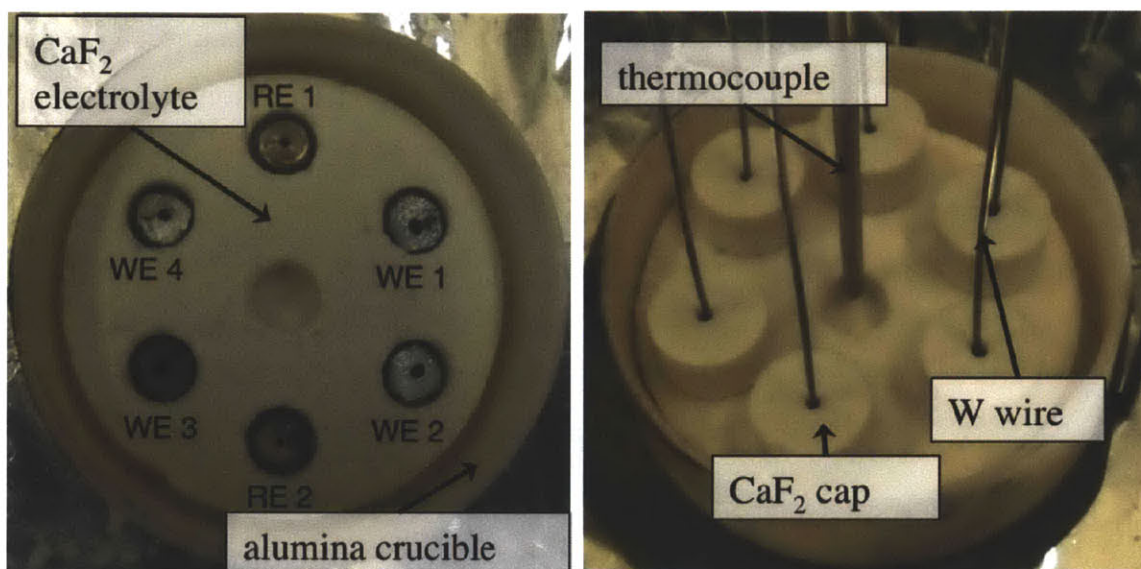
Figure 3-3: Alloys of interest for the emf measurements, with the temperature range of the test

the tungsten electrode lead. Tungsten was chosen since it does not alloy with either calcium or antimony.

For the alloys with high-melting points ( $\text{Ca}_{11}\text{Sb}_{10} + \text{Ca}_5\text{Sb}_3$  and  $\text{Ca}_5\text{Sb}_3 + \text{CaSb}_2$  regions), arc melted samples were inhomogeneous, porous and fragile, resulting in poor contact to electrical leads. For this reason, samples for  $x_{\text{Ca}} = 0.55$  and  $0.63$  were prepared by a powder processing method, adapted from Zevalkink et al. [81] with the help from Alex Zevalkink of the Snyder group at Caltech. The author is very grateful to Alex Zevalkink for her help and advice. For these samples, pure metals were weighed out in an Ar-filled glovebox, ball milled for 1 h in stainless steel crucibles and steel ball milling media, uniaxially hot pressed at 40 MPa under Ar gas at 800 °C for 4 h ( $x_{\text{Ca}} = 0.55$ ) or at 1600 °C for 12 h ( $x_{\text{Ca}} = 0.63$ ), and then annealed for 72 h under vacuum at 650 °C ( $x_{\text{Ca}} = 0.55$ ) or 400 °C ( $x_{\text{Ca}} = 0.63$ ). These samples were prepared in the shape of cylinders 3-5 mm high and 12 mm in diameter. Tungsten rods of 3 mm in diameter were used as electrical leads, providing a larger contact area for these samples that remained solid throughout the experiment.

### 3.2.3 Set-up

The air-tight stainless steel crucible was assembled inside an ultra-high purity Ar-filled glovebox ( $< 0.1$  ppm  $O_2$ ,  $< 0.1$  ppm  $H_2O$ ) and the vessel was sealed at the same time, to avoid any contamination from moisture and oxygen. A schematic of the set-up is presented in Figure 3-2, and pictures of the electrochemical cell are presented in Figure 3-4. The  $CaF_2$  caps positioned above the samples proved to be effective in reducing the evaporation of the alloys, and in particular of the more volatile Sb.



(a) Electrodes in place in the electrolyte before addition of the caps

(b) Electrodes covered with the caps, W leads and thermocouple in place

Figure 3-4: Preparation of the experimental set-up, in the glovebox, before enclosure in the test vessel

## 3.3 Experimental procedure

After assembly inside the glovebox, the air tight crucible was brought outside, and kept under active vacuum ( $\sim 1$  Pa) for 12 h at  $120$  °C in a furnace. Except for the high-melting samples ( $x_{Ca} = 0.55$  or  $0.63$ ), the experiment was started at a temperature above the melting point of the electrodes to ensure good contact with the tungsten electrical leads and the electrolyte. Samples were then cooled to  $600$  °C or less (depending on composition) in increments of  $40$  to  $20$  °C. The dwell time at

each step was about 90 min, then the cell was heated back up to 800 °C, via steps at intermediate temperatures. All temperature changes were made with a 5 °C/min ramp rate. The duration of the experiment was under 24 h.

The emf between one of the REs and the other electrodes was measured using a potentiostat-galvanostat (Autolab PGSTAT 302N, Metrohm AG), and the temperature was measured simultaneously using an ASTM K-type thermocouple. For the analysis of the results, the emf data considered were those recorded after the temperature reached a constant value (standard deviation < 0.5 °C). For all-liquid and partially liquid alloys, the thermodynamic equilibrium was reached almost immediately, while for alloys in a solid + solid 2-phase region, the thermodynamic equilibrium was reached up to 30 min after temperature equilibration. At each temperature step, the alloys were held at thermodynamic equilibrium for more than 30 min.

Sample results, showing the temperature and emf variation vs. time, are shown in Figure 3-5.



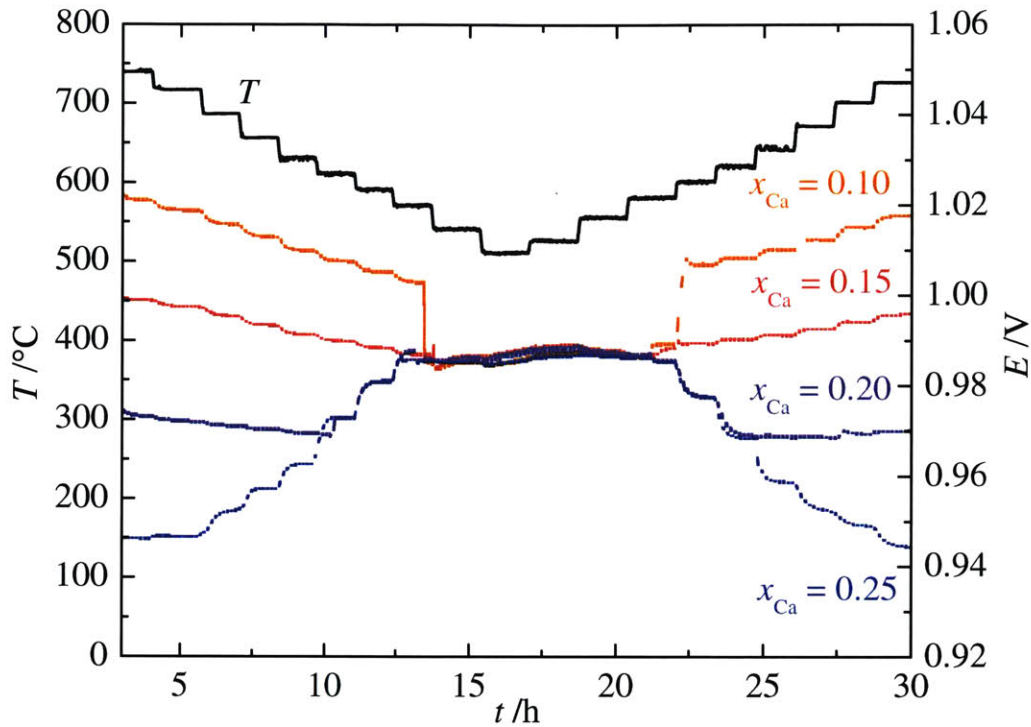


Figure 3-5: Temperature and emf measurements over time of an experiment  $\text{Ca(s)}|\text{CaF}_2|\text{Ca-Sb}$  cell

## 3.4 Sources of experimental errors

### 3.4.1 Temperature deviation

The temperature deviation between the temperature measured by the thermocouple in the middle of the setup and the different peripheral wells was mapped out by Dr. Hojong Kim. The author is grateful to Dr. Hojong Kim to let her use these results. They show that the temperature of the wells is about  $3 \pm 1$  °C warmer than the temperature measured by the central thermocouple (Figure 3-6).

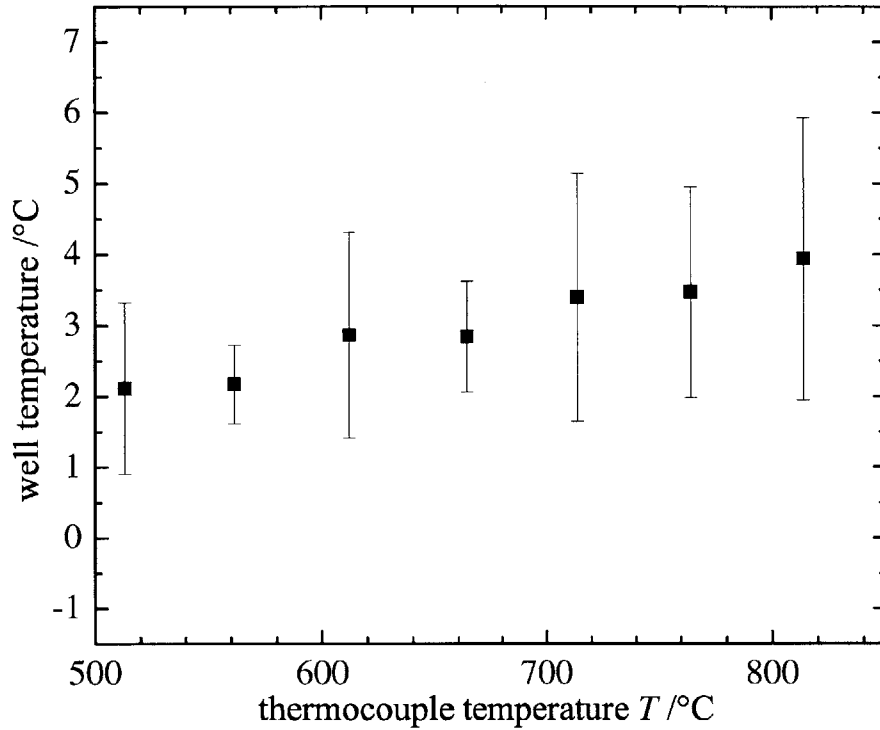


Figure 3-6: Temperature of the wells vs. measured temperature

### 3.4.2 Reference electrodes

The emf measured between the two reference electrodes on opposite sides of each other was less than 2 mV, as shown on Figure 3-7, in a representative example. This represents less than 0.3 % of the emf signal for samples on the high Sb side of the intermetallic, but up to 15 % of the emf signal on the high Ca side of the intermetallic.

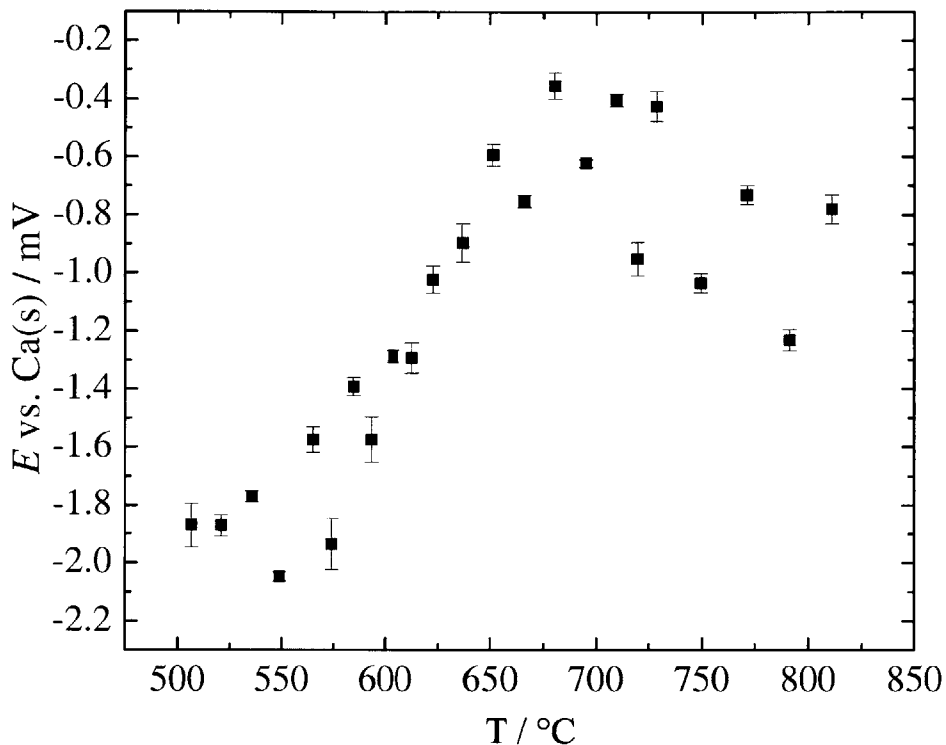


Figure 3-7: Emf measured between 2 Ca REs, in a  $\text{Ca(s)}|\text{CaF}_2|\text{Ca-Sb}$  cell, error bar corresponds to the variation of the signal at equilibrium over a 30 min duration

### 3.4.3 Electrode composition

#### Low-melting samples ( $T_{liq} < 1000$ °C)

The critical step in the preparation of these low-melting point samples, to keep the final composition as close to the nominal composition as possible, was the arc melting step. Indeed, during this step, the calcium and the antimony heat separately before mixing up in the liquid state, since they have different melting points and vapor pressures. The mixing was also observed as a violent exothermic reaction, which further elevated the temperature. After arc melting, the inside chamber of the arc melter was covered with black powder. To mitigate the loss of material, the samples were never heated more than 2-3 s at a time, through several short heatings (usually 3), to avoid heating the whole sample for a long time, while the pieces of Sb and

Ca were positioned close together during the rest times. The sample was also turned upside down before the last heating, to homogenize it.

Since antimony is the lower melting metal, and has a higher vapor pressure than calcium, the loss of material could potentially be attributed to antimony alone, which would mean that the final composition of the sample would differ from the prepared composition. Therefore, the alloys were all weighed after the arc melting step to quantify the weight loss. However, even when attributing the loss to antimony alone, the composition did not vary by more than 1 at%.

The composition of some the samples was also checked afterwards with WDS, since the strongest energy peaks of Ca and Sb are less than 200 eV apart from each other. It confirmed that the composition of the samples was within 1 at% of the nominal composition. As an example, the results for the SEM (BES) analysis of a  $x_{\text{Ca}} = 0.05$  sample (nominal composition), obtained using a JEOL-JSM-5910 SEM are available in Figure 3-8 . The average composition of the sample by WDS analysis, obtained using a JEOL-JXA-733 Superprobe upgrade microscope, was found to be  $x_{\text{Ca}} = 0.05 \pm 0.02$ , using 20 spots of  $50\mu\text{m}$  in diameter. The sample was homogeneous, with bright grains of antimony of approximately  $20\mu\text{m}$  in diameter. The darker phase in between the grains was composed of a lamellar submicron microstructure. The composition of the 2 phases was identified using XRD as  $\text{CaSb}_2$  and Sb, as expected. The scan, obtained with a PANalytical X'pert Pro Multipurpose Diffractometer over a 1.5 h measurement, after identification of the peaks, is available in Figure 3-9. The semiquantitative analysis gave a composition of  $x_{\text{Ca}} = 0.06$ , which is consistent with the WDS quantitative analysis.

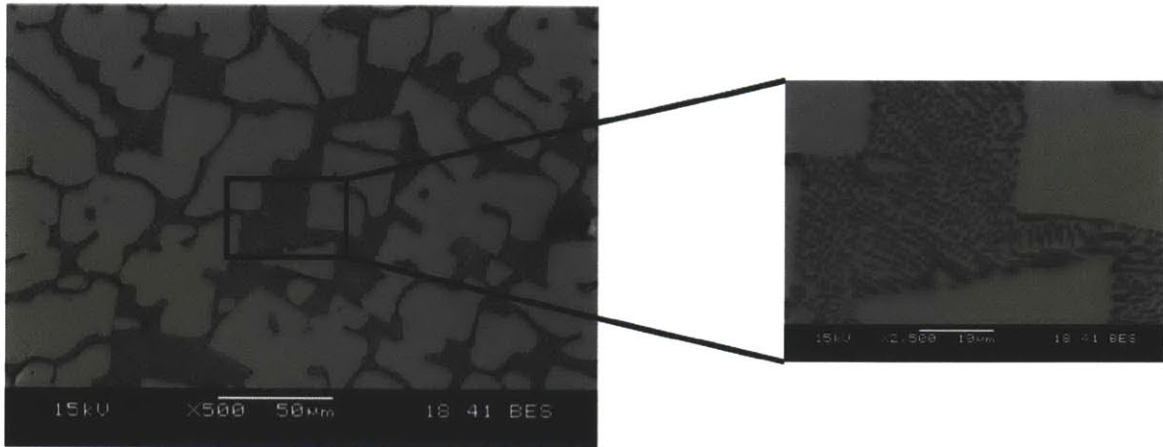


Figure 3-8: Back-scattered image of  $x_{Ca} = 0.05$  Ca-Sb alloy obtained using a JSM-5910 SEM

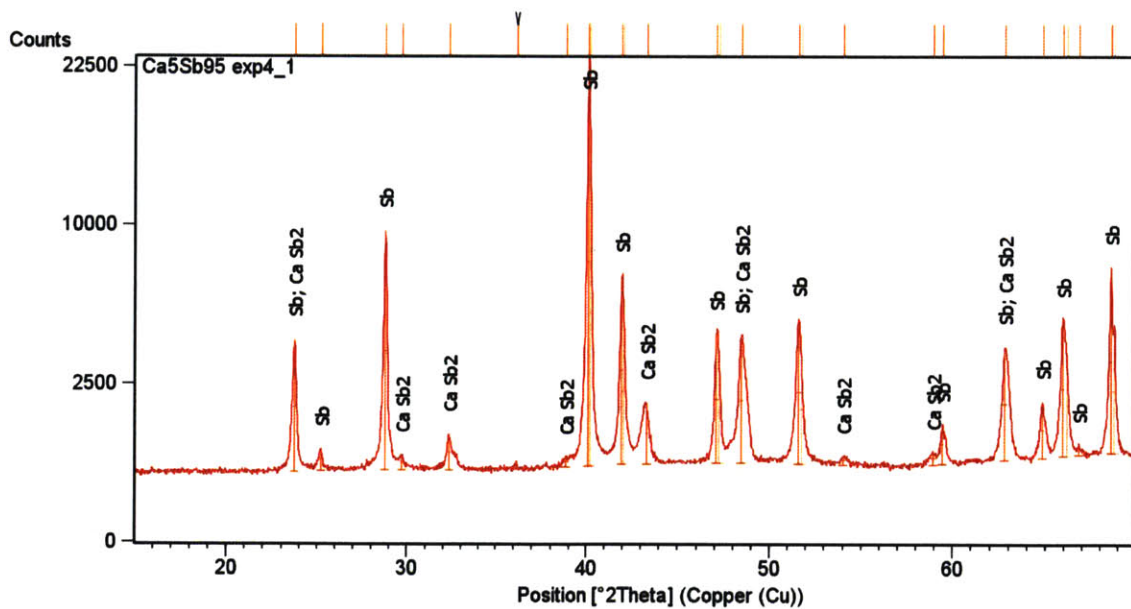


Figure 3-9: Scan of  $x_{Ca} = 0.05$  Ca-Sb alloy obtained using a PANalytical X'pert Pro Multipurpose Diffractometer in 90 min

## High-melting samples ( $T_{liq} > 1000$ °C)

The critical step in the preparation of these high-melting point samples, to keep the final composition as close to the nominal composition as possible, was the scraping of the inside of the stainless steel crucible and of the stainless steel balls, after ball milling. Even though the calcium and antimony react together during the ball milling, a lot of black powder cannot be completely scraped off, and the weight loss between before and after ball milling was up to 5 % of the total weight, while the composition of the black powder lost is not necessarily the same as the nominal composition of the sample. However, these samples' composition remains in a 2-phase domain during the emf measurement, so even if the composition had shifted by a few at%, the emf signal would have stayed the same.

The average composition of the samples was checked using WDS. The XRD scans run under air were not conclusive, because the high-melting intermetallics have complex structures, with numerous peaks, and the samples were reacting with oxygen and moisture during the scan, even with a film protection. Indeed, the activity of Ca in these samples is much higher than in the samples considered previously, and the calcium reactivity is much higher. The SEM (BSE) images available in Figures 3-10 and 3-11 were obtained with a ZEISS 1550VP Field Emission SEM at Caltech University, with the help of Alex Zevalkink. For the  $x_{Ca} = 0.55$  sample, the back-scattered image shows 2 phases, with a very fine structure of the darker phase (submicron features). After analysis with WDS, the brighter phase corresponds to  $x_{Ca} = 0.535 \pm 0.002$ , while the darker phase intertwined with the bright phase, corresponds to  $x_{Ca} = 0.57 \pm 0.01$ , which is consistent with a  $Ca_{11}Sb_{10} + Ca_5Sb_3$  structure. The average composition was measured as  $x_{Ca} = 0.54$ . For the  $x_{Ca} = 0.63$  sample, the back-scattered image shows 3 phases, with a very fine structure (submicron features). The darker phase corresponded to the medium dark phase oxidizing (the oxygen content was measured as high as 25 at% with EDS). After analysis with WDS, the brighter phase corresponds to  $x_{Ca} = 0.614 \pm 0.002$ , while the darker phase corresponded to  $x_{Ca} = 0.660 \pm 0.002$ , which is consistent with a  $Ca_5Sb_3 + Ca_2Sb$  structure. The average composition was

measured as  $x_{Ca} = 0.63$ .

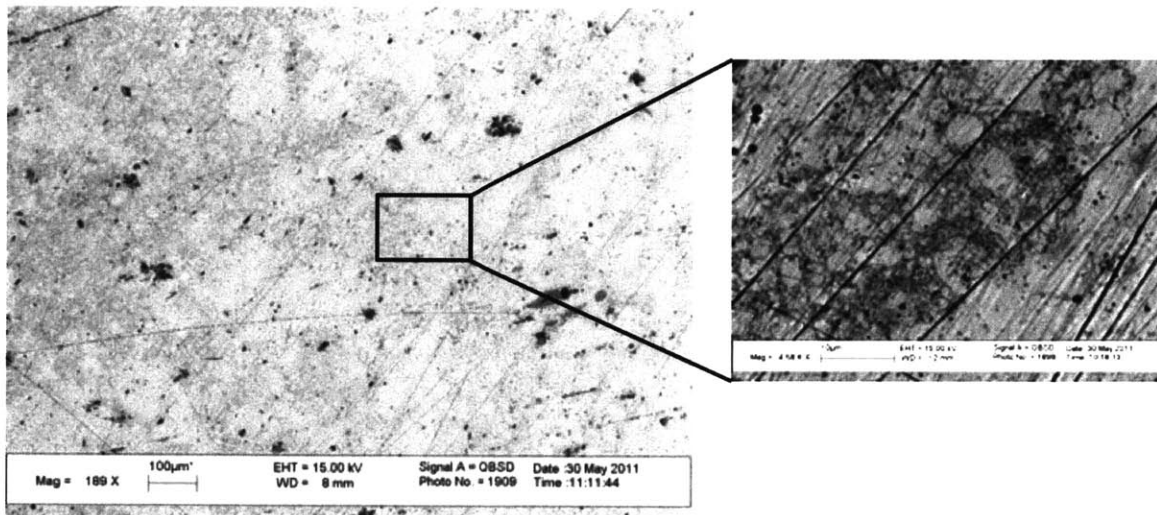


Figure 3-10: Back-scattered image of  $x_{Ca} = 0.55$  Ca-Sb alloy obtained using a ZEISS 1550VP Field Emission SEM

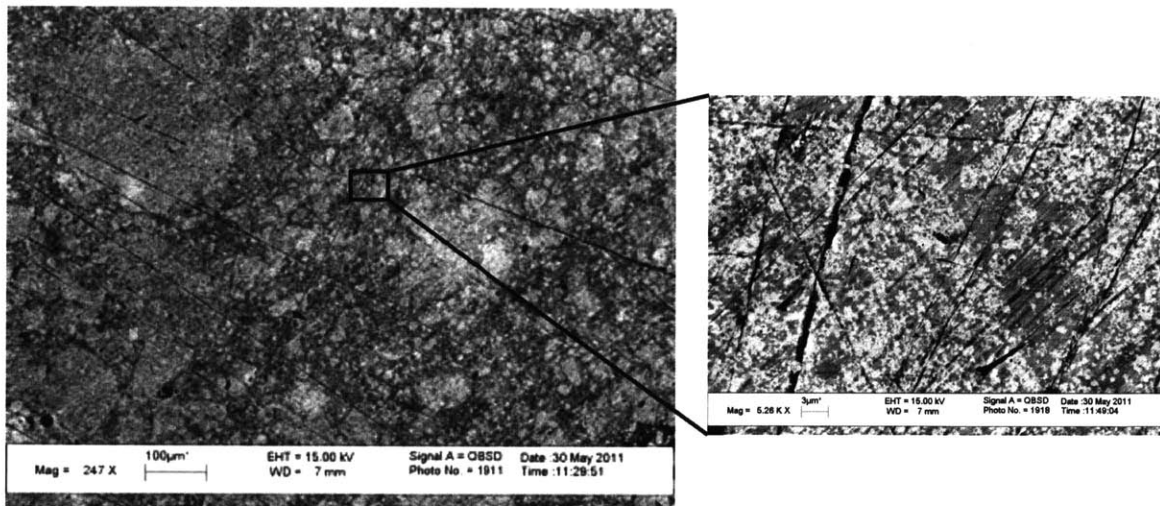
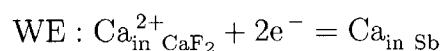
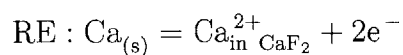


Figure 3-11: Back-scattered image of  $x_{Ca} = 0.63$  Ca-Sb alloy obtained using a ZEISS 1550VP Field Emission SEM

## 3.5 Results and data analysis

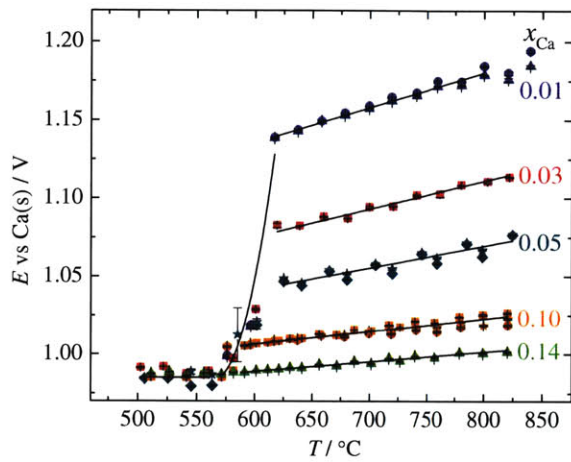
### 3.5.1 Results

The overall cell reaction is the alloying of calcium in antimony according to the following two steps, which correspond to the half reactions at the electrodes:

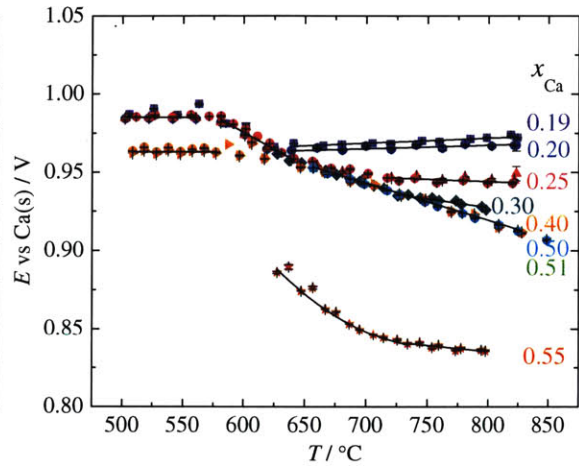


In most cases, Ca(s) was used as reference electrode. However, for the two highest-melting samples, a Ca-Sb alloy ( $x_{\text{Ca}} = 0.40$ ) served this purpose. In a two-phase region L + Ca<sub>11</sub>Sb<sub>10</sub> during the emf measurements, the latter RE allowed to start the experiment at slightly higher temperature, for a better contact between the high-melting electrodes and the electrical leads. The emf of this second RE was measured vs. Ca(s), in the temperature range of interest. Based on this calibration, all data reported herein have been expressed in terms of the pure calcium reference electrode, in its most stable state (solid state) at the temperature and pressure (1 atm) of interest. The variation of emf with temperature is plotted in Figure 3-12. The alignment of the datapoints upon heating and cooling and between different experiments (for instance in the case of  $x_{\text{Ca}} = 0.10$ ), attests to the reversibility and reproducibility of these measurements. The datapoints obtained for Ca-rich alloys ( $x_{\text{Ca}} > 0.625$ ) were not reproducible enough to be used in the derivation of the thermodynamic properties of mixing. Indeed, the error in emf was almost as high as the values themselves (less than 10 mV) for  $x_{\text{Ca}} > 0.80$ . The data for  $x_{\text{Ca}} = 0.63$  were irreproducible (possibly due to oxidation during the experiment).

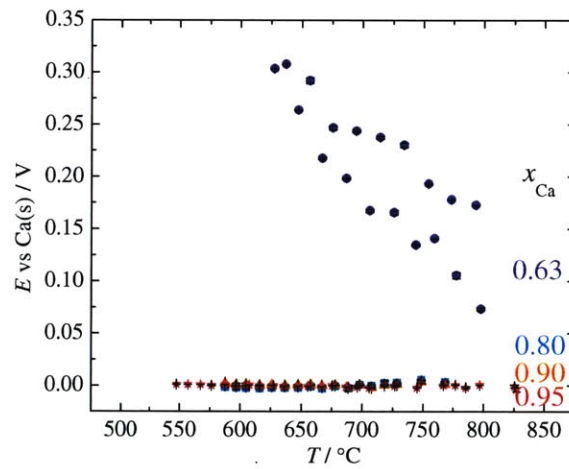




(a)  $x_{Ca} = 0.01$  to  $0.14$



(b)  $x_{Ca} = 0.19$  to  $0.55$



(c)  $x_{Ca} = 0.63$  to  $0.95$

Figure 3-12: Emf vs. temperature data for  $Ca(s)|CaF_2|Ca-Sb$  cells between  $500\text{ }^\circ C$  and  $830\text{ }^\circ C$

Figure 3-13 presents the isothermal variation of emf at 700 °C with increasing Ca content. The data were extracted from the measurements at constant Ca concentration presented in Figure 3-12 and show a major drop in the emf value (about 0.6 V) from the low Ca to high Ca sides of  $\text{Ca}_5\text{Sb}_3$ . This is consistent with the qualitative observation that samples with  $x_{\text{Ca}} > 0.625$  oxidize much faster than those at lower Ca concentrations, indicating a large increase in Ca activity, which corresponds to a much lower emf.

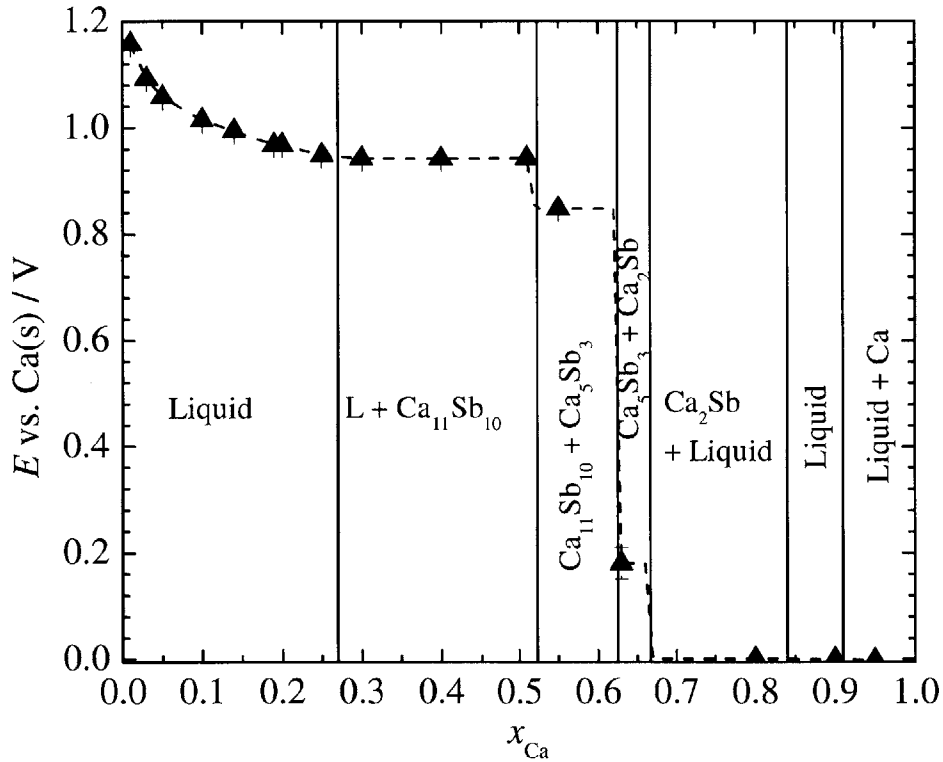


Figure 3-13: Emf vs. Ca concentration in Ca-Sb alloy for  $\text{Ca(s)}|\text{CaF}_2|\text{Ca-Sb}$  cells at 700 °C

### 3.5.2 Data analysis

The emf  $E$  measured between the reference and working electrode can be expressed by the Nernst equation:

$$E_{RE} = E_{Ca}^0 + \frac{RT}{2F} \ln a_{Ca^{2+}} \quad (3.2)$$

$$E_{WE} = E_{Ca}^0 + \frac{RT}{2F} \ln \left( \frac{a_{Ca^{2+}}}{a_{Ca}} \right) \quad (3.3)$$

$$E = E_{WE} - E_{RE} = -\frac{RT}{2F} \ln a_{Ca} \quad (3.4)$$

where  $E_{Ca}^0$  is the standard potential of pure calcium at the temperature  $T$  (in K), and  $R$  and  $F$  are the gas constant and the Faraday constant, respectively. The activity of pure Ca is 1 by convention. The activity of  $Ca^{2+}$  in the electrolyte,  $a_{Ca^{2+}}$ , is the same in equations (3.2) and (3.3). The activity of Ca in the Ca-Sb alloy is noted  $a_{Ca}$ . It is the only unknown and can be directly calculated from the emf.

The activity of the calcium,  $a_{Ca}$ , can be related to the partial Gibbs free energy of calcium,  $\Delta\bar{G}_{Ca}$ , by  $\Delta\bar{G}_{Ca} = RT \ln(a_{Ca})$ . The results for the partial Gibbs free energy of calcium at 800 °C are presented in Figure 3-14 along with the results from the literature reported by Delcet [23] and Bouhajib [11]. The results obtained in this work are consistent with those of Delcet.

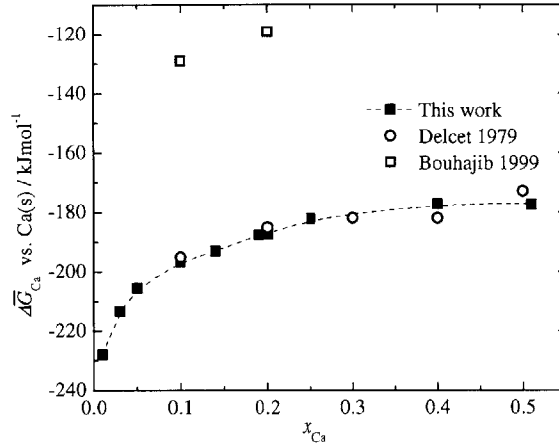


Figure 3-14: Measured partial molar Gibbs free energy vs. Ca concentration of calcium in Ca-Sb alloys at 800 °C compared with the results from Delcet [23] and Bouhajib [11]

### 3.5.3 Activity coefficients and thermodynamic properties of mixing

The activity coefficient of antimony and the integral thermodynamic properties of mixing: the Gibbs free energy,  $\Delta G$ , the entropy,  $\Delta S$ , and the enthalpy,  $\Delta H$ , were derived according to the integral Gibbs-Duhem relationship:

$$\begin{aligned} \ln \gamma_{\text{Sb}} &= -x_{\text{Ca}}(1 - x_{\text{Ca}})\alpha(x_{\text{Ca}}) - \int_0^{x_{\text{Ca}}} \alpha(c) dc \\ \Delta G &= (1 - x_{\text{Ca}}) \int_0^{x_{\text{Ca}}} \alpha(c) dc \\ \Delta S &= (1 - x_{\text{Ca}}) \int_0^{x_{\text{Ca}}} \beta(c) dc \\ \Delta H &= \Delta G + T\Delta S \end{aligned}$$

where:  $\alpha(x_{\text{Ca}}) = \frac{\Delta \bar{G}_{\text{Ca}}}{(1-x_{\text{Ca}})^2}$ ,  $\beta(x_{\text{Ca}}) = -\frac{(\partial \Delta \bar{G}_{\text{Ca}} / \partial T)_{x_{\text{Ca}}}}{(1-x_{\text{Ca}})^2}$ , and  $x_{\text{Ca}}$  is the mole fraction of calcium in the alloy.

$\Delta \bar{G}_{\text{Ca}}(x_{\text{Ca}}, T)$  was fitted as a linear function of temperature for constant composition, giving  $\Delta \bar{H}_{\text{Ca}}(x_{\text{Ca}}, T)$  and  $\Delta \bar{S}_{\text{Ca}}(x_{\text{Ca}}, T)$  by the relation  $\Delta \bar{G}_{\text{Ca}}(x_{\text{Ca}}, T) = \Delta \bar{H}_{\text{Ca}}(x_{\text{Ca}}, T) - T\Delta \bar{S}_{\text{Ca}}(x_{\text{Ca}}, T)$  in the all-liquid region, in the liquid +  $\text{Ca}_{11}\text{Sb}_{10}$  re-

$x_{\text{Ca}}$	$T$ (°C)	$\Delta\bar{H}_{\text{Ca}}$ (kJ/mol)	$\Delta\bar{S}_{\text{Ca}}$ (J/mol/K)
0.01	616 - 800	$-181 \pm 1$	$43 \pm 1$
0.03	619 - 822	$-177 \pm 1$	$35 \pm 1$
0.05	624 - 825	$-177 \pm 2$	$27 \pm 2$
0.10	591 - 821	$-180.4 \pm 0.5$	$15.8 \pm 0.6$
0.14	591 - 821	$-180.3 \pm 0.6$	$12.1 \pm 0.6$
0.19	640 - 825	$-181 \pm 1$	$6.2 \pm 0.9$
0.20	638 - 824	$-182 \pm 1$	$4 \pm 1$
0.25	720 - 824	$-188 \pm 2$	$-6 \pm 2$
0.30	726 - 798	$-202 \pm 2$	$-22 \pm 2$
L + $\text{Ca}_{11}\text{Sb}_{10}$	666 - 828	$-226.6 \pm 0.7$	$-45.8 \pm 0.7$
L + $\text{CaSb}_2$	580 - 641	$-261 \pm 4$	$-83 \pm 4$
$\text{Ca}_{11}\text{Sb}_{10}$ + $\text{Ca}_5\text{Sb}_3$ high T	734 - 798	$-178 \pm 3$	$-15 \pm 3$
Sb + $\text{CaSb}_2$	502 - 580	$-190.10 \pm 0.02$	0
$\text{CaSb}_2$ + $\text{Ca}_{11}\text{Sb}_{10}$	508 - 577	$-185.9 \pm 0.1$	0

Table 3.1: Partial molar enthalpy and entropy of calcium in Ca-Sb alloys vs. Ca(s) determined from the linear fit of the experimental data (T in K), with the temperature range over which the fit is valid

$x_{\text{Ca}}$	$T$ (°C)	$a$	$b$	$c$
L + Sb	571 - 617	$82 \pm 8$	$-0.75 \pm 0.07$	$0.097 \pm 0.009$
$\text{Ca}_{11}\text{Sb}_{10}$ + $\text{Ca}_5\text{Sb}_3$ low T	627 - 734	$9 \pm 2$	$-0.07 \pm 0.01$	$0.008 \pm 0.002$

Table 3.2: Emf (in V) measured vs. Ca(s) as a function of temperature (in K) non linear fits:  $E = a + bT + cT \ln(T)$

gion, and in the  $\text{Ca}_{11}\text{Sb}_{10}$  +  $\text{Ca}_5\text{Sb}_3$  region (Table 3.1). In the low temperature solid + solid regions (Sb +  $\text{CaSb}_2$  and  $\text{CaSb}_2$  +  $\text{Ca}_{11}\text{Sb}_{10}$  regions),  $\Delta\bar{G}_{\text{Ca}}$  was found to be independent of temperature. In the liquid + Sb and low temperature  $\text{Ca}_{11}\text{Sb}_{10}$  +  $\text{Ca}_5\text{Sb}_3$  regions, the emf did not vary linearly with temperature and was found to follow  $E = a + bT + cT \ln(T)$ , with  $T$  in K (Table 3.2). The same fit was used by Petric et al. [56] in the case of K-Bi alloys.

$\alpha(x_{\text{Ca}})$  and  $\beta(x_{\text{Ca}})$  were then fitted with a piecewise cubic hermite interpolating polynomial before the integration to obtain  $a_{\text{Sb}}$ ,  $\Delta G$ ,  $\Delta S$  and  $\Delta H$ . The results at 800 °C are presented in Figures 3-15 and 3-16, with the data in Table 3.3.  $a_{\text{Ca}}$  and  $a_{\text{Sb}}$  are reported with reference to Ca(s) and Sb(l), while the thermodynamic properties of mixing are reported with reference to Sb(l) and undercooled Ca(l). The solid phase of Ca in the temperature range of interest is bcc. Using the Ca(bcc) phase as

reference, the Gibbs energy of Ca(l) is  $G^0(\text{Ca}, l) = +8540 - 7.659T$  in J/K [37].

In the two-phase regions, the chemical potentials of Ca and Sb do not change with composition; therefore, the integral properties of mixing vary linearly with composition at a given temperature.  $\Delta H(x_{\text{Ca}})$  and  $\Delta S(x_{\text{Ca}})$  in these regions are also reported in Table 3.3, together with the values for  $\text{Ca}_{11}\text{Sb}_{10}$  and  $\text{Ca}_5\text{Sb}_3$ .

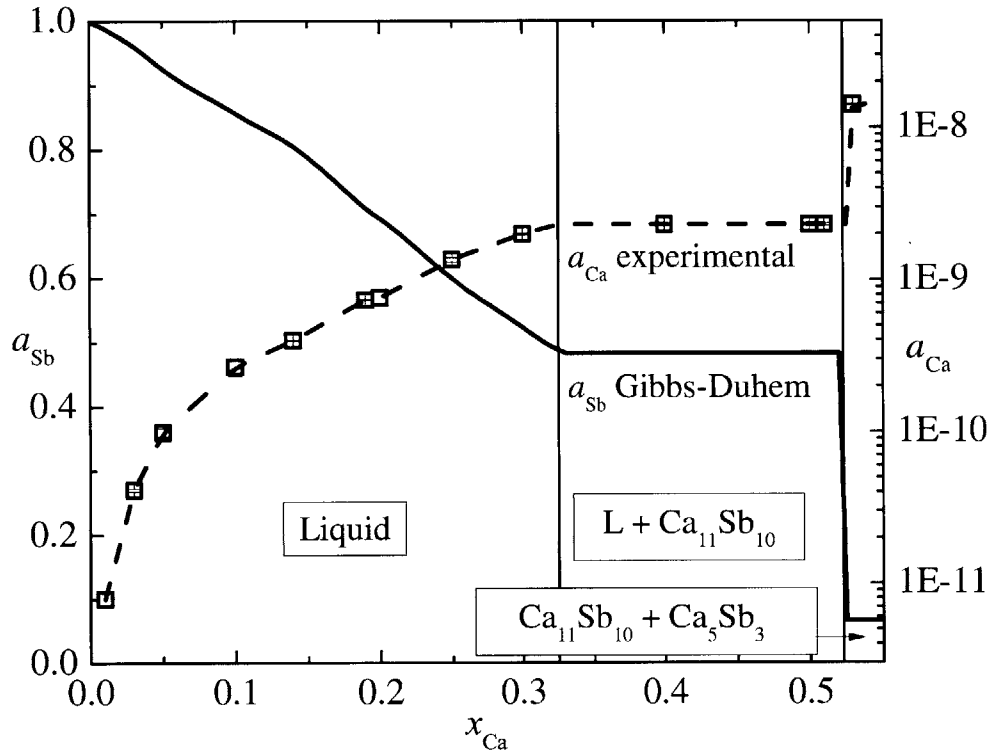


Figure 3-15: Activities of Ca and Sb vs. Ca concentration in Ca-Sb alloys at 800 °C vs. Ca(bcc) and Sb(l) (data in Table 3.3)

$x_{\text{Ca}}$	$a_{\text{Ca}}$	$a_{\text{Sb}}$	$\Delta H$ (kJ/mol)	$\Delta S$ (J/mol/K)
0.01	8.15E-12	0.989	-1.97	0.380
0.02	1.97E-11	0.976	-3.85	0.713
0.04	6.06E-11	0.944	-7.56	1.25
0.06	1.19E-10	0.910	-11.3	1.63
0.08	1.81E-10	0.883	-15.0	1.89
0.10	2.46E-10	0.857	-18.8	2.06
0.12	3.11E-10	0.832	-22.6	2.17
0.14	3.90E-10	0.806	-26.4	2.24
0.16	5.12E-10	0.770	-30.1	2.27
0.18	6.65E-10	0.729	-33.9	2.25
0.20	8.16E-10	0.693	-37.7	2.15
0.22	1.01E-9	0.657	-41.5	1.96
0.24	1.24E-9	0.617	-45.5	1.68
0.26	1.46E-9	0.583	-49.5	1.28
0.28	1.69E-9	0.553	-53.6	0.74
0.30	1.93E-9	0.523	-57.8	0.0122
0.32	2.30E-9	0.493	-62.4	-1.08
Ca <sub>11</sub> Sb <sub>10</sub>	2.23E-9	0.483	-114	-16.8
Ca <sub>5</sub> Sb <sub>3</sub>	1.43E-8	0.0654	-130	-18.5
L + Ca <sub>11</sub> Sb <sub>10</sub>	2.23E-9	0.483	18.8 - 254 $x_{\text{Ca}}$	23.6 - 77.1 $x_{\text{Ca}}$
Ca <sub>11</sub> Sb <sub>10</sub> + Ca <sub>5</sub> Sb <sub>3</sub>	1.43E-8	0.0654	-32.3 - 156 $x_{\text{Ca}}$	-7.46 - 17.6 $x_{\text{Ca}}$

Table 3.3: Activities of Ca (with the measured standard deviation) and Sb vs. Ca(s) and Sb(l), and enthalpy and entropy of mixing vs. Ca(l) and Sb(l) at 800 °C in Ca-Sb alloys

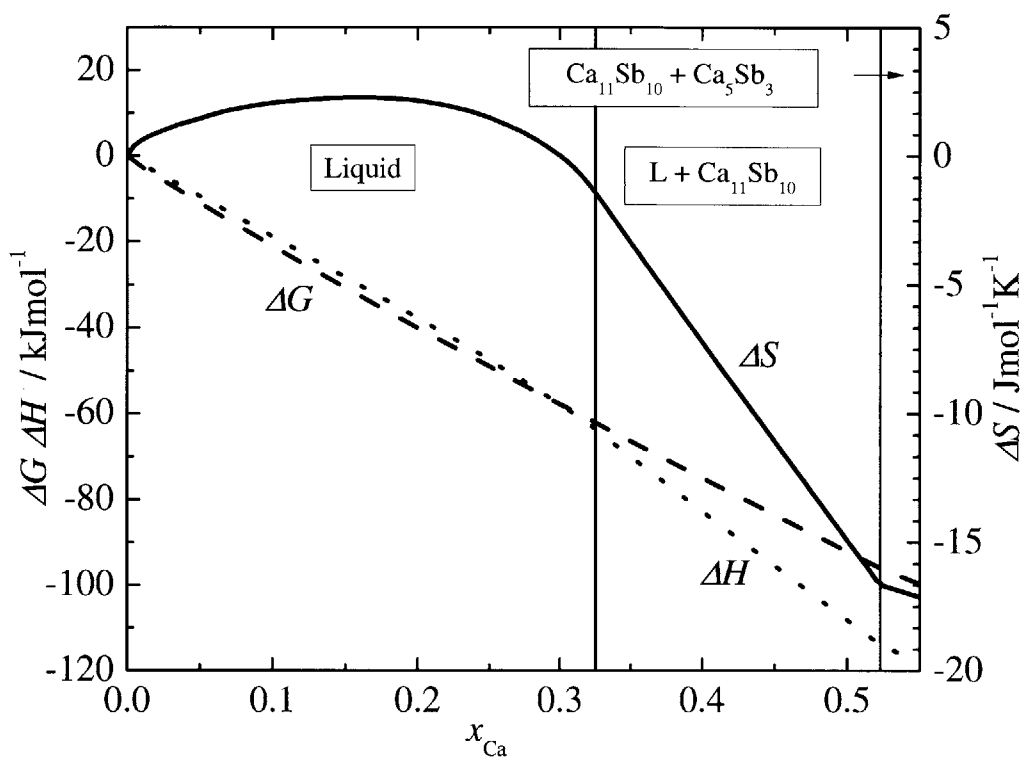


Figure 3-16:  $\Delta H$ ,  $\Delta G$  and  $\Delta S$  vs. Ca concentration of Ca-Sb alloys at 800 °C vs. Ca(l) and Sb(l) (data in Table 3.3)

### 3.5.4 Phase diagram

The goal here was not to derive a new phase diagram for the Ca-Sb system, but rather to use the data we could get from our emf measurements to provide additional data to the existing ones, and check the consistency with what was in the literature.

From the intersection points of the emf fitting lines, the liquidus temperatures of the Ca-Sb alloys as well as the eutectic and peritectic temperatures can be extracted for  $x_{Ca} < 0.5$ . From Tables 3.1 and 3.2, the fit for the emf signal can be extracted for the samples at different temperatures. By finding numerically the temperature at which these fits intersect, the temperature of the phase change can be estimated. The use of intersection points minimized the impact of metastable states on the results. The uncertainty in our temperature evaluation comes from the temperature variation



between the different wells, which was measured to be  $\pm 1$  °C, the average temperature difference between the central and peripheral wells having been corrected. Also, the emf was not measured continuously with temperature, but only every 20 °C. And finally, while the emf data lie on a line in a single-phase region, such as the liquid region, they do not necessarily in a two-phase region, such as the L + Sb region. Therefore it is not as straightforward to choose a fit for these points, which will impact the intersection temperature of the data fits that indicate the liquidus temperature. In Figure 3-17, the results are plotted on the latest version of the Ca-Sb phase diagram [53], together with the differential thermal analysis (DTA) measurements by Niyazova [49] and Bouhajib [12]. The intersection points are reported in Table 3.4.

The overall shape is consistent with the Ca-Sb phase diagram from Okamoto [53], even though the temperature of the L + Sb liquidus is lower than the previous measurements. The emf fit for the L + Sb phase was not very satisfying due to the low number of points, as it can be seen on Figure 3-12 (a), and therefore the temperatures at which this fit intersects with the liquid phase fitting lines may have been underestimated in this case. The peritectic temperature ( $633$  °C  $\pm$   $12$  °C) is between the inconsistent temperatures measured by Niyazova ( $730$  °C  $\pm$   $5$  °C) and Bouhajib ( $597$  °C). This study suggests that the eutectic point occurs at lower Ca content ( $x_{Ca} = 0.14$  vs.  $0.18$ ) than reported in [53], although the eutectic temperature is fairly consistent.

$x_{Ca}$	$T_{liq}$ (°C)
0.01	621
0.03	610
0.05	601
0.10	588
0.14	575
0.19	625
0.20	631
0.25	685
0.30	736

Table 3.4: Liquidus temperatures of Ca-Sb alloys found by intersecting the emf fitting lines

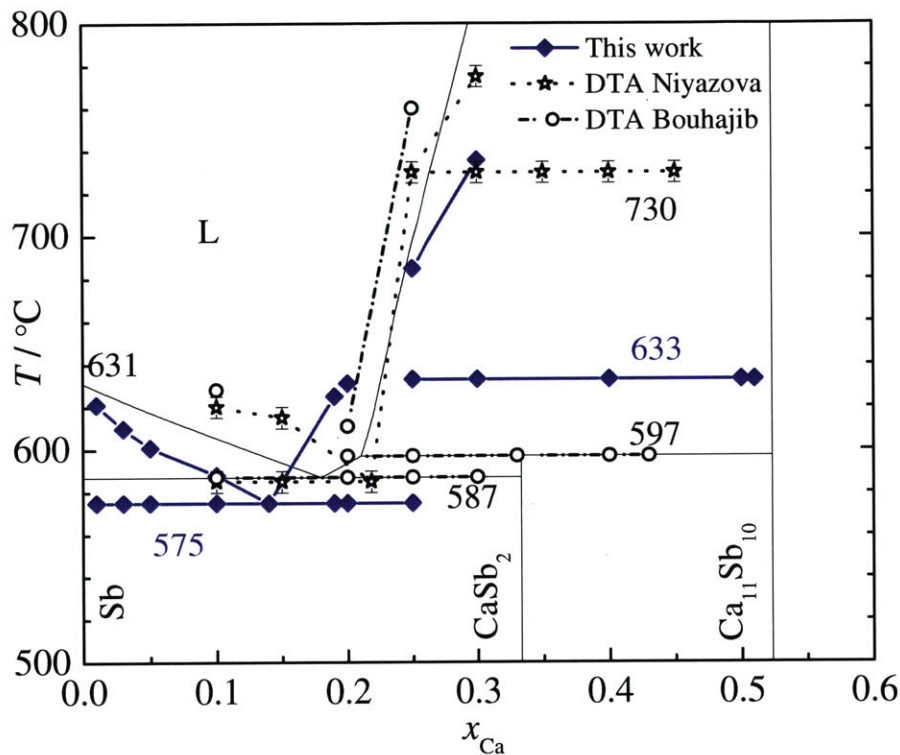


Figure 3-17: Liquidus and transition temperatures from emf and DTA measurements [49, 12] on Ca-Sb phase diagram [53] (data in Table 3.4)

### 3.6 Conclusions of the chapter

The partial thermodynamic properties of Ca and Sb in Ca-Sb liquid alloys, as well as the integral mixing properties, were determined via emf measurements. They confirm the results obtained by Delcet et al. [23] via coulometric titration at 800 °C and expand the scientific knowledge of the thermodynamic properties of this system, down to 600 °C over the full range of compositions. This confirmation of the measurements by Delcet et al. also gives confidence that the measurements realized by the same research team for Ca-Ag, Ca-Bi, Ca-In, Ca-Pb, Ca-Sn, Ca-Tl, and Ca-Zn are reliable, and could be used to compare the Ca-Sb system to other systems with high-melting intermetallics. The melting points of Ca-Sb alloys between  $x_{\text{Ca}} = 0.01$  and  $x_{\text{Ca}} = 0.25$  were also estimated by intersecting the fitted emf vs. temperature lines, questioning

in particular the peritectic temperature of the currently accepted phase diagram.

Based on these emf measurements, and especially based on the low Ca activity in Ca-Sb alloys on the Sb side of the high-melting intermetallics, Sb is an attractive material for a positive electrode in a Ca-based LMB, since the OCV would be more than 0.9 V in the 650–800 °C range.



## Chapter 4

# Thermodynamic modeling of Ca-Sb liquid alloys at 800 °C

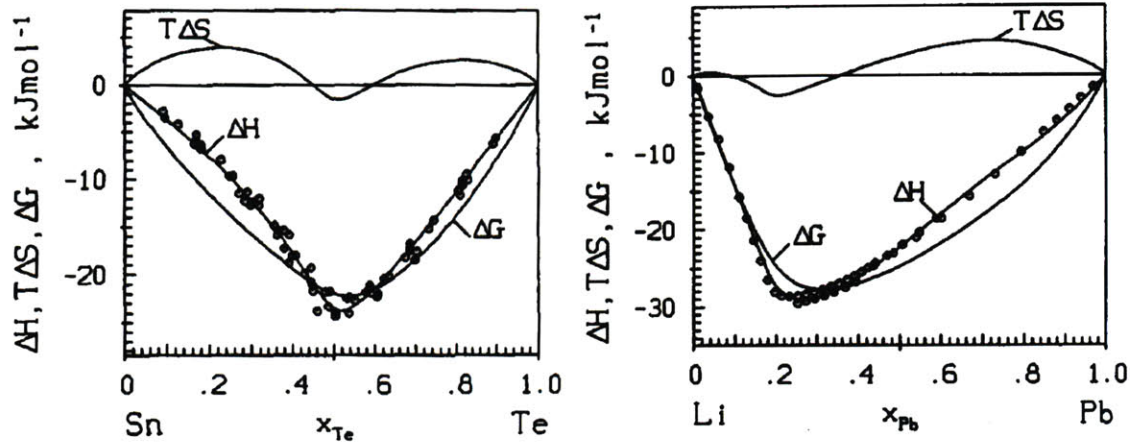
Ca-Sb liquid alloys, like most alloys of systems with high-melting intermetallics, exhibit thermodynamic properties far from ideality. By modeling the thermodynamic properties of the Ca-Sb liquid alloys, one can understand the relationship between their atomic structure and their macroscopic thermodynamic properties. Two models were chosen to answer this question: an association model and the molecular interaction volume model (MIVM). With Ca-Sb as the physical system of interest, the objective is to reconcile these two models and to show how the structure of liquid Ca-Sb alloys affects their thermodynamic properties at 800 °C.

## 4.1 Association model

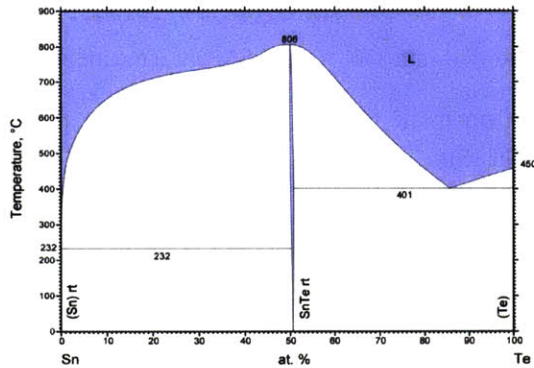
### 4.1.1 Evidence of short-range order

The association model was introduced by Bhatia in 1974 [8]. This model is used to describe short-range order for liquid alloys with compound-forming tendency. The short-range ordered volume parts are described as associates with a well defined composition,  $C \equiv A_aB_b$ , while the rest of the A and B atoms are considered as free atoms. The attribution of a well defined composition to the short-range ordered parts of the liquid alloy is justified by the observation of maximal deviation from ideal mixing of the properties of the alloy, such as electrical conductivity or thermodynamic properties, at a specific ratio of A and B, that corresponds to C. Sometimes, only one maximum is observed, as in Li-Pb, but in other cases, several local maxima are observed, as in Na-Pb and Na-Sn [45, 72], which are explained by the presence of several compositions of associates (2 and 3 respectively). Therefore, the modeling can become very complicated, involving many parameters.

The variation in  $\Delta H$  and  $\Delta S$  with composition differs substantially between the case of a compound-forming alloy and the case of an alloy of very similar elements. Indeed, in the case of an alloy of very similar elements, the shape of  $\Delta H$  and  $\Delta S$  can be described by a parabola. However, in the case of compound-forming alloys with one associate, the shape of  $\Delta H$  is closer to a triangle, while  $\Delta S$  exhibits 2 maxima and a minimum instead of only one maximum.  $\Delta H$  and  $\Delta S$  reach their minima for  $C \equiv AB$ , as in the case of Sn-Te alloys, or off-stoichiometry, as in the case of Li-Pb, as exhibited in Figure 4-1 from [70]. The associate usually has the same composition as an intermetallic of the system, but not always. For instance, in the two cases considered above, the compositions for which the entropy and the enthalpy of mixing reach their minima correspond to the highest-melting intermetallics of these systems: SnTe and  $Li_{17}Pb_4$ . However in the case of Ca-Mg, the entropy of mixing reaches its minimum for  $x_{Ca} = 0.5$ , while the only intermetallic in the Ca-Mg system is  $Ca_2Mg$ , as seen in Figure 4-2.

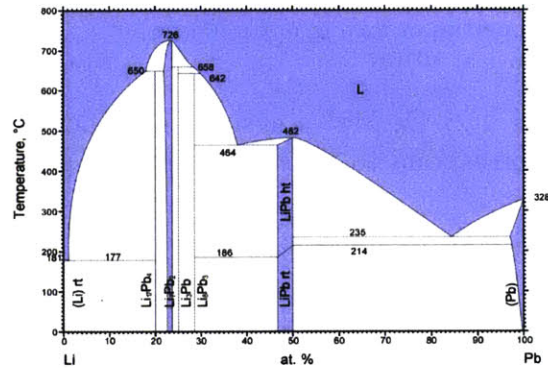


(a) Properties of mixing of Sn-Te liquid alloys at 1140K, experimental data from [9] <sup>1</sup>  
 (b) Properties of mixing of Li-Pb liquid alloys at 1000K, experimental data from [60] <sup>1</sup>



© ASM International 2009. Diagram No. 101216

(c) Sn-Te phase diagram [44]



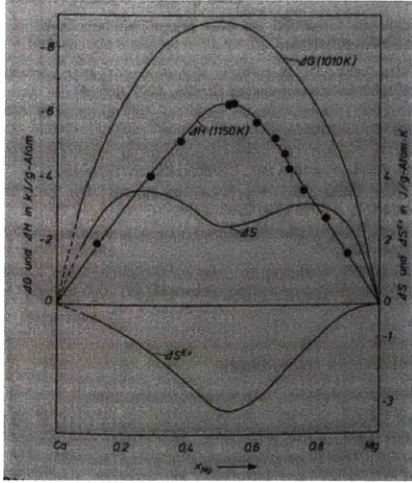
© ASM International 2006. Diagram No. 981004

(d) Li-Pb phase diagram [52]

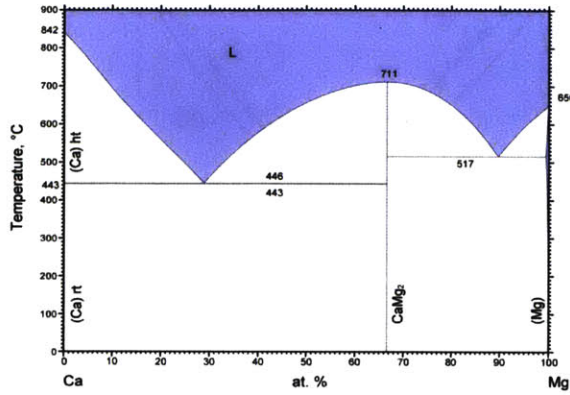
Figure 4-1: Thermodynamic properties of mixing of Sn-Te and Li-Pb alloys, modeled by Sommer using the association model [70], and corresponding phase diagrams from ASM international

Other data can give insight into short-range ordering in liquid alloys. For instance, the shape of the structure factor, obtained via XRD or neutron diffraction measurements, and in particular the presence of pre-peaks, is directly indicative of short-range order. By identifying the composition for which the intensity of the pre-peak is maximal, Alblas et al. [3] were able to identify the existence of an associate of the approximate composition  $\text{NaSn}/\text{Na}_4\text{Sn}_3$  in the Na-Sn system, as reproduced in Figure 4-3.

<sup>1</sup>The slopes of the Gibbs free energy and entropy of mixing should be infinite for  $x = 0$  and  $1$ .



(a) Properties of mixing of Ca-Mg liquid alloys at 1010K [68]



(b) Ca-Mg phase diagram [36] from ASM international

Figure 4-2: Ca-Mg: a system for which the minimum in the entropy of mixing does not correspond to the composition of an intermetallic

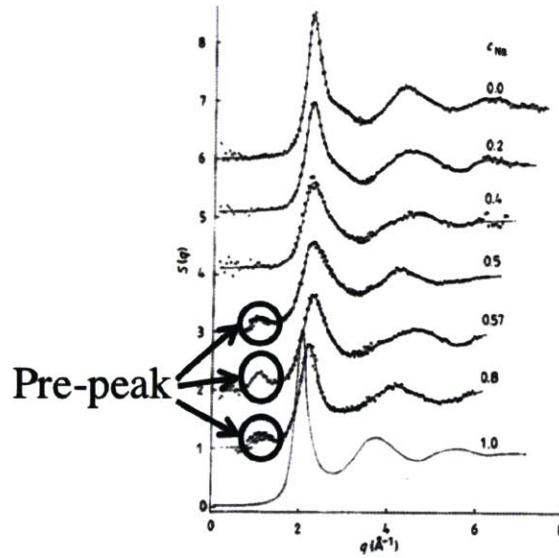


Figure 4-3: Total structure factor  $S(q)$  for liquid Na-Sn alloys, from neutron diffraction measurements at different compositions 25 °C above the liquidus temperature [3]



Short-range order can also affect properties such as the electrical resistivity. For instance, Rais et al. [61] developed a set-up that allowed them to measure the electrical resistivity and thermodynamic properties of liquid alloys simultaneously, and applied it to liquid Na-In and Na-Sn alloys. They showed that the electrical resistivity presented a peak very close to the same composition that corresponded to a minimum of the enthalpy of mixing, suggesting that, close to maximum short-range order, the properties of the associate can greatly affect the properties of the overall solution.

### 4.1.2 Model theory

Figure 4-4 presents a schematic of the melt as envisioned by the associate model. 3 types of atom are present in solution, located at lattice sites. A and B are the pure elements, while C is an associate formed of A and B atoms.

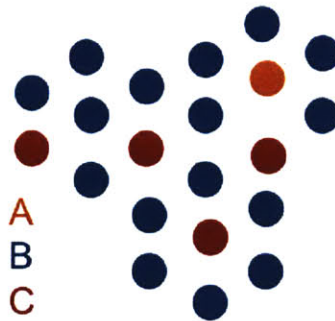


Figure 4-4: Schematic of an A-B melt forming a C associate according to the associate model

#### **First assumption: composition of the associate(s)**

First, the presence and composition of an associate needs to be assumed to start modeling the system. Once the composition of the associate has been determined using one of the above techniques, the composition of the ternary melt can be expressed via the equilibrium constant of the association reaction. The association model has been used many times since its introduction by Bhatia [7, 42, 69, 70]. The notations used here are the same as those used by Bergman et al. [7].

For a reaction  $aA + bB \rightarrow C \equiv A_aB_b$ , of equilibrium reaction K:

$$K = \exp\left(-\frac{\Delta H^0 - T\Delta S^0}{RT}\right) = \frac{a_C}{a_A^a a_B^b} = \frac{X_C \gamma_C}{(X_A \gamma_A)^a (X_B \gamma_B)^b} \quad (4.1)$$

$$X_A = \frac{x_A - aN_C}{N_T} \quad (4.2)$$

$$X_B = \frac{1 - x_A - bN_C}{N_T} \quad (4.3)$$

$$X_C = \frac{N_C}{N_T} \quad (4.4)$$

where  $N_C$  is the number of associates per mole of alloy.  $N_T = 1 - (a + b - 1)N_C$  is the number of “particles” (free atoms or associates) per mole of alloy.  $\Delta H^0$  and  $\Delta S^0$  are the enthalpy and entropy of formation of the associate respectively,  $x_A$  is the fraction of A in the binary alloy,  $X_i$  is the molar fraction of the species  $i$  in the ternary melt.

### Second assumption: configurational entropy

The free atoms and associates are supposed to be located on lattice sites. Indeed, the association model is based on a description used for alloys in the solid state, that has been adapted to take into account the presence of associates. Based on the analogy with the solid state, three expressions have been used in the literature for the configurational entropy, even though the simplest,  $s_I$ , is usually good enough. Indeed, the difference in configurational entropy depending on the expression chosen is often negligible compared to the entropy of mixing of the alloy. The first expression for the configurational entropy,  $s_I$ , used by Sommer and Krull [42], assumes that the free atoms and the associates all have the same volume (each species occupies one lattice site only) and are randomly distributed. The two other expressions take the difference in volume into account by assuming that the associate  $A_aB_b$  occupies  $a+b$  lattice sites. The Flory expression,  $s_{II}$ , based on Flory’s description of polymer solutions, takes this difference in volume into account and assumes that the A and B atoms involved in C can be exchanged with free A and B atoms. The third expression,  $s_{III}$ , proposed by Bergman in 1982 [7], also assumes that the associate  $A_aB_b$  occupies  $a+b$  lattice sites, but A and B atoms involved in C cannot be exchanged with free A and B atoms.

These different expressions for the configurational entropy are:

$$s_I = -R \sum_{i=A,B,C} X_i \ln X_i \quad (4.5)$$

$$s_{II} = -R \sum_{i=A,B,C} X_i \ln \Phi_i \quad (4.6)$$

where:

$$\begin{aligned} \Phi_A &= \frac{X_A}{X_A + X_B + (a+b)X_C} \\ \Phi_B &= \frac{X_B}{X_A + X_B + (a+b)X_C} \\ \Phi_C &= \frac{(a+b)X_C}{X_A + X_B + (a+b)X_C} \end{aligned}$$

$$\begin{aligned} s_{III} = -R \left( \sum_{i=A,B,C} X_i \ln X_i + \ln N_T \right) - R \frac{N_C}{N_T} \ln(a+b) \\ + R \frac{(a+b-1)(1-(a+b)N_C)}{(a+b)N_T} \ln(1-(a+b)N_C) \quad (4.7) \end{aligned}$$

The entropy of mixing is then defined as  $\Delta S = N_C \Delta S^0 + N_T s_i$ .

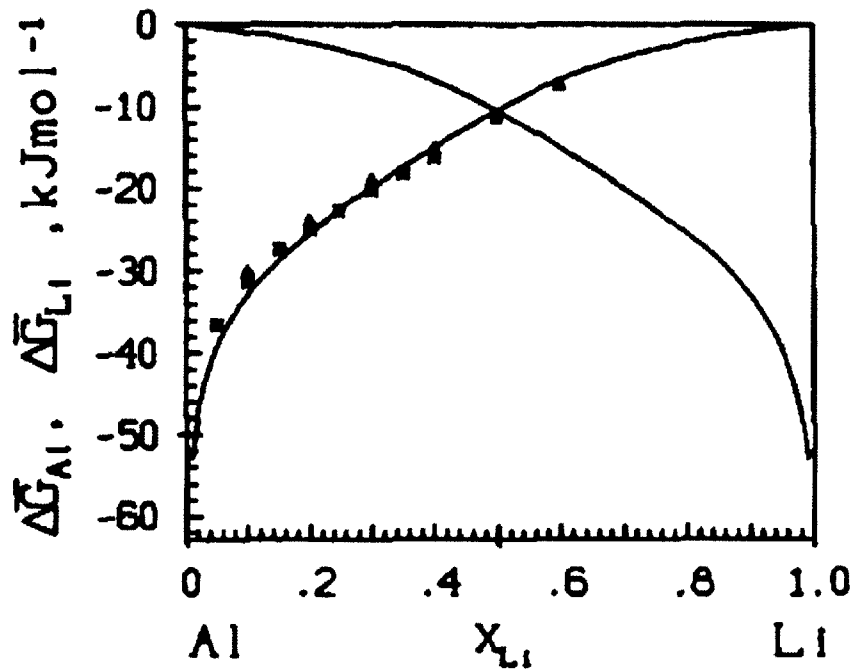
### Third assumption: interaction model

Depending on the degree of interaction between the monoatomic species and the associate, an interaction model is chosen. In most cases, the regular solution model is sufficient. The enthalpy of mixing is then defined as  $\Delta H = N_C \Delta H^0 + N_T \sum_{i \neq j} (\omega_{ij} X_i X_j)$ , where  $\omega_{ij}$  is the interaction coefficient between species  $i$  and  $j$ .

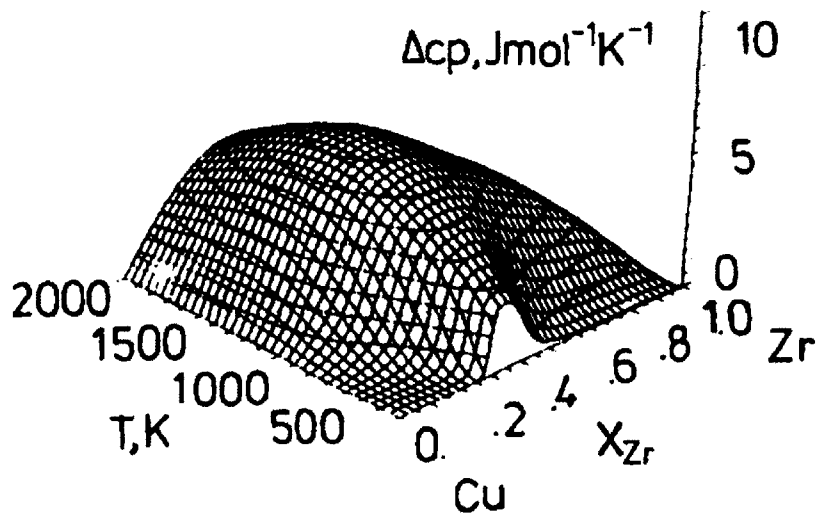
### 4.1.3 Applications of the association model

The association model has been used for many compound-forming alloys, such as In-Te [63], Al-Te [63], Li-Mg, Al-Li, Sn-Te, Lu-Pb, Cu-Si, Cu-Ce, Cu-Zr, Al-La, Ce-Mg, Cu-Mg [70] to name a few. It is mainly used to model the thermodynamic properties

of mixing, which explains why the minimum in the entropy is usually the indication used to identify the composition of the associate, since it does not require any other experiment. From the thermodynamic properties of mixing, other properties can then be derived, such as the partial molar properties, by considering the partial differentials of the properties of mixing, and the heat molar capacity. Assuming that the entropy and enthalpy of formation of the associates do not vary with temperature, the temperature dependence of the thermodynamic properties of the liquid alloys can be derived as well. A couple of applications of the association model are reproduced in Figure 4-5, from the work of Sommer [70].



(a) Partial Gibbs free energy of mixing of Li-Al liquid alloys at 970 K, experimental data from [29]



(b) Concentration and temperature dependence of excess molar heat of Cu-Zr liquid alloys, calculated [71]

Figure 4-5: Thermodynamic properties of compound-forming alloys, modeled by Sommer using the association model [70]

## 4.2 Molecular interaction volume model (MIVM)

The other model considered here is the MIVM, introduced by Tao in 2000 [73]. Even though the association model was expected to give reasonable agreement with the experiment, since Ca-Sb has properties very far from ideality, and forms high-melting intermetallics, like the other systems for which the association model was successful, there was a need for an easier-to-manipulate model. Indeed, the association model requires the identification of at least one associate, which leads to at least 5 constants that need to be fitted simultaneously. In addition, the expression of the properties of mixing requires the use of a functional: the thermodynamic functions depend on the molar fractions of associate(s) and free atoms, that depend on each other through the equilibrium constant.

Multiple models have been developed to describe the properties of liquid mixtures [59]. Most are based on the description of the liquid state as a quasicrystal, where each molecule tends to stay in a small region, a more or less fixed position in the space about which it vibrates back and forth. The association model is an example of such a lattice model. However, since a liquid is not completely equivalent to a quasicrystal, other authors have developed other types of models, where the liquid mixture is considered as a gas mixture, such as van der Waals-type theories.

### 4.2.1 Model theory

Figure 4-6 presents a schematic of the melt as envisioned by the MIVM. The MIVM is a model derived from statistical thermodynamics that considers the stability of each type of atom,  $i$  and  $j$ , based on the pair potential interaction energies  $\epsilon$  with its nearest neighbors. It is a fluid-based model that takes into account the volume and number of nearest neighbors of each one of the species.

To derive the Gibbs energy of the liquid mixture, Tao goes back to statistical mechanics, defining the partition function for independent indistinguishable particles, taking into account the translational energy and the potential energy, which depends on the interaction between the molecules: for a pure metal  $i$ , using the notations from

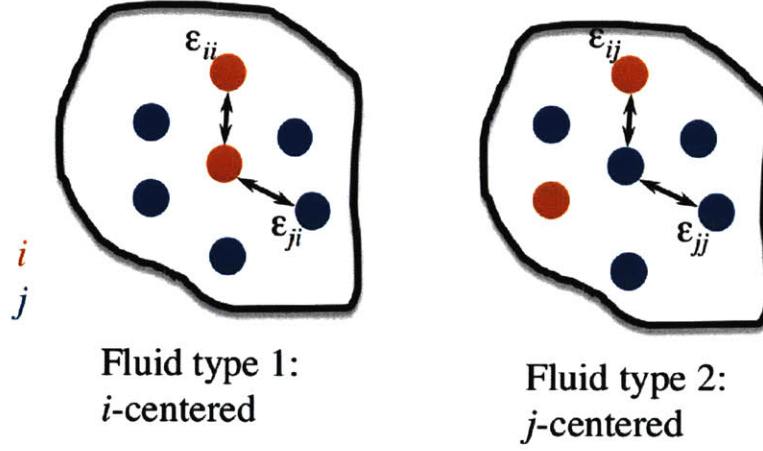


Figure 4-6: Schematic of an  $i - j$  melt according to the MIVM: two types of hypothetical fluids are present in solution, which depend on the center atom considered.

Tao, the partition function is expressed as:

$$Q_i = \frac{Q_{pi}}{N_i! \Lambda_i^{3N_i}} = \frac{1}{N_i! \Lambda_i^{3N_i}} \times \left( \frac{V_i}{N_i} \right)^N \exp \left( \frac{-Z_i N_i \epsilon_{ii}}{2kT} \right) \quad (4.8)$$

where  $\Lambda_i^{3N}$  is the partition function of molecular kinetic energy,  $N$  the molecular number,  $V$  the volume,  $Z$  is the atomic first coordination number,  $\epsilon_{ii}$  is the  $i - i$  pair potential energy.

For  $i - j$  liquid mixture, the partition function is expressed as:

$$Q = \frac{Q_p}{N_i! \Lambda_i^{3N_i} N_j! \Lambda_j^{3N_j}} = \frac{1}{N_i! \Lambda_i^{3N_i} N_j! \Lambda_j^{3N_j}} \times \left( \frac{V}{N} \right)^N \exp \left( \frac{-N \epsilon_p}{kT} \right) \quad (4.9)$$

where  $\epsilon_p$  is the  $i - j$  mixing potential energy.

Using the relation between Gibbs energy and partition function, the molar excess Gibbs energy can then be defined:

$$\frac{G_m^E}{RT} = x_i \ln \left( \frac{V_i}{x_i V} \right) + x_j \ln \left( \frac{V_j}{x_j V} \right) + \frac{2\epsilon_p - Z_i x_i \epsilon_{ii} - Z_j x_j \epsilon_{jj}}{2kT} \quad (4.10)$$

According to the two-liquid theory [59], the molar excess Gibbs energy can then

be expressed as:

$$\frac{G_m^E}{RT} = x_i \ln \left( \frac{V_{mi}}{x_i V_{mi} + x_j V_{mj} B_{ji}} \right) + x_j \ln \left( \frac{V_{mj}}{x_j V_{mj} + x_i V_{mi} B_{ij}} \right) - \frac{x_i x_j}{2} \left( \frac{Z_i B_{ji} \ln B_{ji}}{x_i + x_j B_{ji}} + \frac{Z_j B_{ij} \ln B_{ij}}{x_j + x_i B_{ij}} \right) \quad (4.11)$$

where  $V_m$  is the molar volume, and  $B_{ji}$  and  $B_{ij}$  the pair potential interaction parameters. The pair potential interaction parameters are defined as:

$$B_{ji} = \exp \left( -\frac{\epsilon_{ji} - \epsilon_{ii}}{kT} \right), B_{ij} = \exp \left( -\frac{\epsilon_{ij} - \epsilon_{jj}}{kT} \right) \quad (4.12)$$

with the energy coefficients defined as  $\epsilon_{ij} = -kT \ln(Z_{ij}/x_j)$ , where  $Z_{ij}$  is the number of  $j$  atoms surrounding the central  $i$  atom. The other energy coefficients are defined similarly.

From these new expressions for the configurational partition functions of liquids and their mixtures, Tao expressed the activity coefficients of each of the species  $i$  and  $j$  in a binary liquid alloy  $i - j$  [73].

$$\ln \gamma_i = \ln \left( \frac{V_{mi}}{x_i V_{mi} + x_j V_{mj} B_{ji}} \right) + x_j \left( \frac{V_{mj} B_{ji}}{x_i V_{mi} + x_j V_{mj} B_{ji}} - \frac{V_{mi} B_{ij}}{x_j V_{mj} + x_i V_{mi} B_{ij}} \right) - \frac{x_j^2}{2} \left( \frac{Z_i B_{ji}^2 \ln B_{ji}}{(x_i + x_j B_{ji})^2} + \frac{Z_j B_{ij} \ln B_{ij}}{(x_j + x_i B_{ij})^2} \right) \quad (4.13)$$

$$\ln \gamma_j = \ln \left( \frac{V_{mj}}{x_j V_{mj} + x_i V_{mi} B_{ij}} \right) + x_i \left( \frac{V_{mi} B_{ij}}{x_j V_{mj} + x_i V_{mi} B_{ij}} - \frac{V_{mj} B_{ji}}{x_i V_{mi} + x_j V_{mj} B_{ji}} \right) - \frac{x_i^2}{2} \left( \frac{Z_j B_{ij}^2 \ln B_{ij}}{(x_j + x_i B_{ij})^2} + \frac{Z_i B_{ji} \ln B_{ji}}{(x_i + x_j B_{ji})^2} \right) \quad (4.14)$$

## 4.2.2 Applications of the MIVM

Tao developed the MIVM to predict activity coefficients in multicomponent systems, taking into account only the interaction between a center atom and its nearest neigh-



bors in the mixing energy of the multicomponent alloy. He was able to use his model to describe the properties of binary alloys of similar elements such as Al, Bi, Cd, In, Pb, Sn, Zn [74], and from that derived properties for the ternary [75, 74, 73], quaternary [78, 73] and quinary systems [76, 79]. For instance, Tao predicted the activities of the different components in lead-free solder [78] using the MIVM.

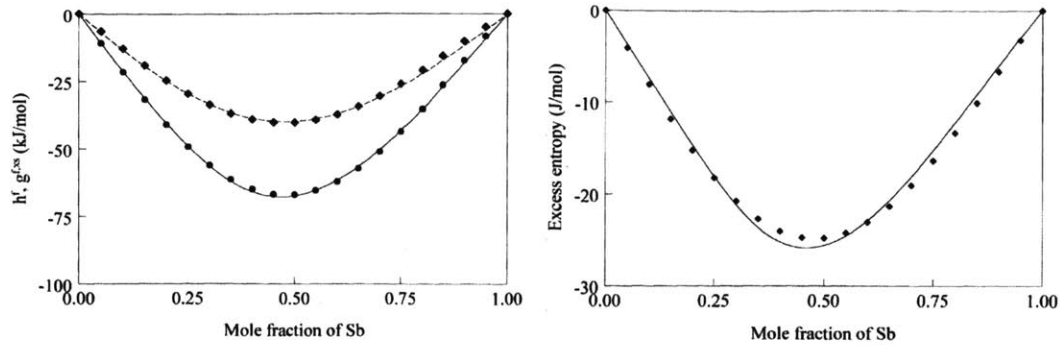
The MIVM has never been used to model liquid alloys with very dissimilar elements, such as Ca and Sb. However, the fact that it introduces different interaction coefficients corresponding to the interaction in the environment of a  $i$  vs. a  $j$  atom, instead of a global coefficient, as well as the fact that the range of interest for our application only corresponds to one side of the high-melting intermetallics (the Sb side), are encouraging.

## 4.3 Application to Ca-Sb liquid alloys at 800 °C

### 4.3.1 Application of the regular association model to Ca-Sb liquid alloys

The regular association model was first used to model the interaction between the monoatomic species and the associate. The first challenge was to identify which associate was formed, assuming only one was formed. Bouhajib [11] had modeled this system using the data he had obtained through his calorimetric measurements [10]. He found that the associate formed was CaSb. It fits indeed very well the experimental data he had obtained (Figure 4-7). The paper does not disclose however, how Bouhajib obtained experimental data for liquid Ca-Sb alloys with  $x_{\text{Ca}} > 0.3$ , since at 1078 K, the Ca-Sb alloys are not completely liquid starting at  $x_{\text{Ca}} > 0.3$ , and he doesn't report measurements for  $x_{\text{Ca}} > 0.6$  anywhere else.

It is indeed challenging to infer the composition of the associate in the case of Ca-Sb liquid alloys because there is only a limited range of compositions for which the properties of mixing of the fully liquid alloys can be measured at 1073 K. And in particular, the entropy and enthalpy of mixing do not reach a minimum in this range.



(a) Enthalpy (full line) and excess Gibbs free energy of mixing (dotted line) (b) Integral excess entropy of mixing of liquid Ca-Sb alloys

Figure 4-7: Thermodynamic properties of mixing of Ca-Sb liquid alloys at 1078 K, solid points: experimental points; line: calculated using the association model assuming the presence of a CaSb associate [11]

However, the entropy of mixing reaches a maximum, and by trying out different compositions for the associate  $C$  when modeling the thermodynamic properties, this maximum can or cannot be reproduced. Following Bouhajib's work [11], the first associate considered in this work was CaSb. However, the simultaneous fit of the entropy and enthalpy of mixing poorly modeled our experimental data. The associate CaSb<sub>2</sub>, corresponding to the intermetallic with the highest antimony to calcium ratio, was next tried and much more satisfactory results were achieved.

The equations introduce 5 parameters: 3 interaction coefficients, as well as the entropy and enthalpy of formation of the associate. These were optimized simultaneously by fitting the thermodynamic properties of mixing  $\Delta H$ ,  $\Delta G$  and  $\Delta S$ . Depending on the starting values chosen, a different solution set can be found for those parameters due to the complexity of the equations, as has been observed by Krull [42]. The optimized values for each of the configurational entropy expressions are presented in Table 4.1. The results for  $\Delta H$  and  $\Delta S$  after optimization are presented in Figure 4-8 in comparison with the experimental values obtained in chapter 3. All 3 expressions for the configurational entropy were tried, and all yielded good results ( $\pm 0.2$  kJ/mol error on  $\Delta H$  and  $\pm 0.1$  J/mol/K error on  $\Delta S$ ). However,  $\Delta S$  modeled using  $s_I$  and  $s_{II}$  reproduce the shape of the experimental data, and in particular its maximum, more accurately. This implies that the hypothesis made for  $s_{III}$ , namely

	$\Delta H^0$ (kJ/mol)	$\Delta S^0$ (J/mol/K)	$\omega_{\text{Ca-Sb}}$ (kJ/mol)	$\omega_{\text{Ca-CaSb}_2}$ (kJ/mol)	$\omega_{\text{Sb-CaSb}_2}$ (kJ/mol)
with $s_I$	$-194 \pm 1$	$-5.5 \pm 0.1$	$-10.5 \pm 1$	$-28 \pm 1$	$7.5 \pm 1$
with $s_{II}$	$-192 \pm 1$	$-10.1 \pm 0.1$	$-138 \pm 1$	$-136.5 \pm 1$	$1.5 \pm 1$
with $s_{III}$	$-190 \pm 1$	$-2 \pm 0.1$	$-195 \pm 1$	$-113 \pm 1$	$-2 \pm 1$

Table 4.1: Enthalpy and entropy of formation of  $\text{CaSb}_2$  and interaction coefficients found for each expression of the configurational entropy at 800 °C

that free Ca and Sb cannot be exchanged with atoms involved in the formation of  $\text{CaSb}_2$ , is not valid for Ca-Sb liquid alloys.

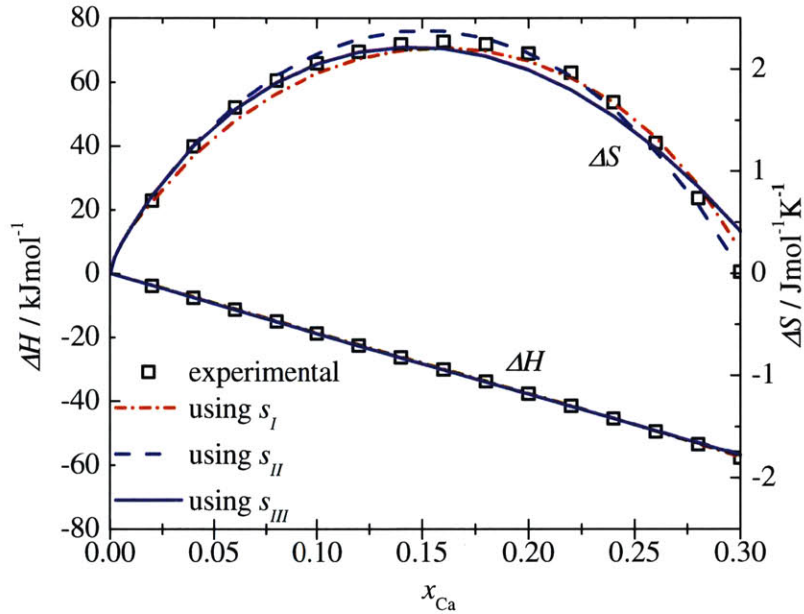


Figure 4-8: Enthalpy and entropy of mixing of Ca-Sb liquid alloys vs. Ca concentration at 800 °C (reference  $\text{Sb}(l)$  and  $\text{Ca}(l)$ )

The negative Gibbs free energy of formation of the associate  $\text{CaSb}_2$  confirm that it is stable in Ca-Sb liquid alloys. Figure 4-9 gives information about the arrangement of the “lattice”. It shows that Ca atoms do not exist free in the melt but are completely associated with Sb forming  $\text{CaSb}_2$ .

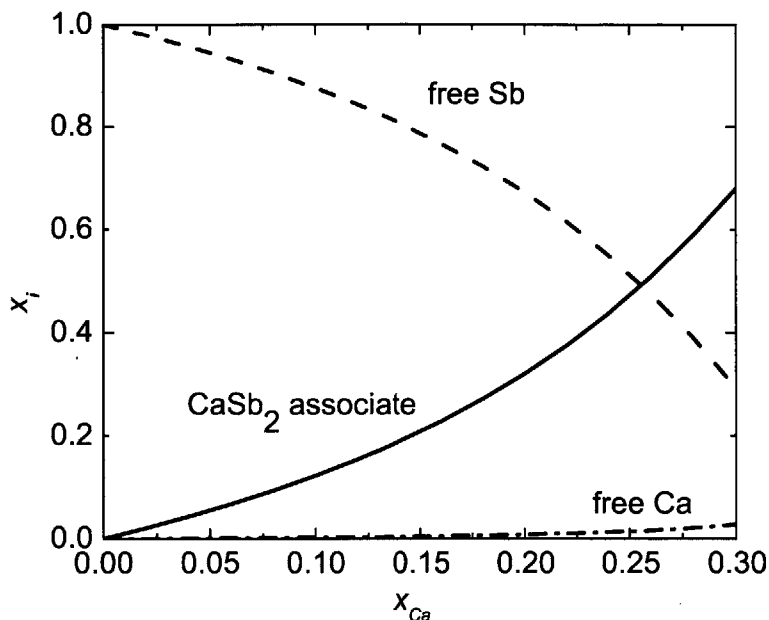


Figure 4-9: Composition of the ternary melt at 800 °C using  $s_{II}$

element	$V_m$ (m <sup>3</sup> / mol) [34]	$Z$ [77]
Ca at 842 °C	$29.54 \times 10^{-6}$	10.33
Sb at 800 °C	$19.21 \times 10^{-6}$	8.53

Table 4.2: Input parameters in the MIVM: molar volume and atomic first coordination number

### 4.3.2 Application of the MIVM to Ca-Sb liquid alloys

While the regular solution model does not require any input coefficient, but has 5 fitting parameters, the MIVM introduces only two interaction coefficients:  $B_{SbCa}$  and  $B_{CaSb}$ . The other parameters that appear in the expression of the activity coefficients are properties of the pure metals, which can be found in the literature:  $Z$  the number of first nearest neighbors and  $V_m$  the molar volume. The values used for the input parameters  $V_m$  and  $Z$  are reported in Table 4.2. For Ca, these properties were assessed at 842 °C, its melting point, even though the temperature of interest is 800 °C. However, the temperature variation of these parameters over 42 °C is minimal in the liquid state.

To find the interaction coefficients, Tao uses the values of the activity coefficients

$x_{\text{Ca}}$	$a_{\text{Ca}} \text{ exp}$	$a_{\text{Ca}} \text{ model}$	emf error (mV)	$\Delta\overline{G}_{\text{Ca}}$ error (kJ/mol)
0.01	$8.15 \times 10^{-12}$	$1.10 \times 10^{-11}$	-14	3
0.03	$3.65 \times 10^{-11}$	$3.80 \times 10^{-11}$	-2	0.4
0.05	$8.97 \times 10^{-11}$	$7.26 \times 10^{-11}$	10	-2
0.10	$2.46 \times 10^{-10}$	$2.03 \times 10^{-10}$	9	-2
0.14	$3.90 \times 10^{-10}$	$3.71 \times 10^{-10}$	2	-0.5
0.19	$7.41 \times 10^{-10}$	$7.00 \times 10^{-10}$	3	-0.5
0.20	$8.16 \times 10^{-10}$	$7.88 \times 10^{-10}$	2	-0.3
0.25	$1.35 \times 10^{-9}$	$1.37 \times 10^{-9}$	-0.8	0.2
0.30	$1.93 \times 10^{-9}$	$2.31 \times 10^{-9}$	-8	2

Table 4.3: Experimental and modeled activities of Ca in Ca-Sb alloys at 800 °C and corresponding emf and  $\Delta\overline{G}_{\text{Ca}}$  difference

of each species at infinite dilution, which simplifies the equations [74]. Here,  $B_{ji}$  and  $B_{ij}$  were found by fitting all the datapoints for  $a_{\text{Ca}}$  obtained in this work. Only  $a_{\text{Ca}}$  was used for fitting since  $a_{\text{Sb}}$  was not measured independently. Since  $a_{\text{Ca}}$  was obtained via emf measurements, the emf error  $|E_{\text{MIVM}} - E_{\text{exp}}|$  was minimized, where  $a_{\text{Ca}}$  is related to  $E$  by the Nernst equation  $E = -\frac{RT}{2F} \ln a_{\text{Ca}}$ . This corresponds to minimizing the error in the partial Gibbs free energy of Ca since  $\Delta\overline{G}_{\text{Ca}} = -zFE$ . The algorithm used is discussed in Chapter 5.

The interaction parameters found are  $B_{\text{SbCa}} = 24$  and  $B_{\text{CaSb}} = 1.2$ . The average difference between the emf modeled and the emf measured was  $\pm 5.6$  mV, or 0.6% of the emf measured (Table 4.3, Figure 4-10). This corresponds to an average absolute error of 1 kJ/mol in  $\Delta\overline{G}_{\text{Ca}}$ , or 0.6%.

In the case of alloys with similar elements [73], Tao found interaction parameters both close to 1, while in the case of Ca-Sb liquid alloys,  $B_{\text{SbCa}}$  is very far from 1. It is the first time that an interaction parameter with a value far from 1 is observed when using the MIVM. To interpret this difference in terms of the structure of the liquid alloys, the fractions of Ca and Sb surrounding Ca and Sb are presented in Figure 4-11. While the fractions of Ca and Sb surrounding Sb correspond to the average composition of the liquid alloy, as in the alloys studied by Tao, Ca atoms are surrounded almost exclusively by Sb atoms.

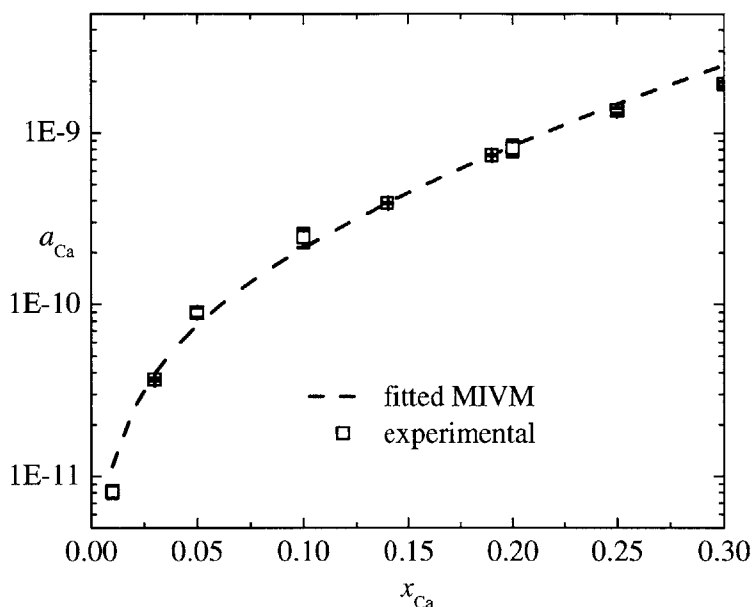


Figure 4-10: Activity of Ca vs. Ca concentration in Ca-Sb liquid alloys at 800 °C, with experimental error, (reference Sb(l) and Ca(bcc))

## 4.4 Comparison of the association model and the MIVM

### 4.4.1 Quantitative comparison

To compare the results of the modeling approaches, the activity of Ca was also calculated from the Gibbs free energy of mixing modeled via the regular association model. The best results were achieved with the first expression for the configurational entropy, used by Sommer and his collaborators. These results are reported in Table 4.4. As can be seen, the results are not as good as in the case of the MIVM, which is expected since only the integral properties were modeled. However, they are still close. The average error between the emf modeled and measured is  $\pm 14$  mV (1 %). This corresponds to an average absolute error of 3 kJ/mol in  $\Delta\bar{G}_{Ca}$ , or 1%.

The partial properties of Ca, and the activity of Ca, are related to the Gibbs free

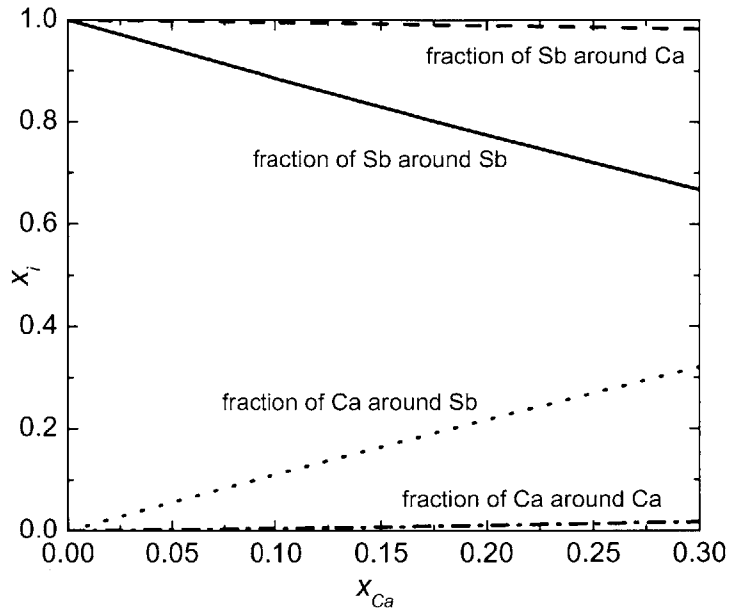


Figure 4-11: The variation of Ca and Sb environments vs. Ca concentration in Ca-Sb liquid alloys at 800 °C

energy of mixing via:

$$\Delta \bar{G}_{Ca}(x_{Ca}) = \Delta G(x_{Ca}) + (1 - x_{Ca}) \frac{\partial \Delta G}{\partial x_{Ca}}$$

Special care was taken regarding the state of reference of Ca, since the properties of mixing had been optimized vs. Ca(l) and Sb(l), and the activity of Ca is defined vs. Ca(bcc).

#### 4.4.2 Qualitative comparison

Both models show that Ca-Sb liquid alloys do not exhibit random mixing but short-range ordering. In the association model, the formation of CaSb<sub>2</sub> associates explains the shape of the thermodynamic properties of mixing of the Ca-Sb alloys. In this case, Ca does not exist as a free atom in the ternary melt, but is stabilized when associated with Sb to form CaSb<sub>2</sub>. Since CaSb<sub>2</sub> and Sb are the two species present in the melt, the Ca atoms forming CaSb<sub>2</sub> associates are almost exclusively surrounded

$x_{\text{Ca}}$	$a_{\text{Ca}} \text{ exp}$	$a_{\text{Ca}} \text{ model}$	emf error (mV)	$\Delta\overline{G}_{\text{Ca}}$ error (kJ/mol)
0.01	$8.15 \times 10^{-12}$	$1.59 \times 10^{-11}$	-31	6
0.03	$3.65 \times 10^{-11}$	$5.02 \times 10^{-11}$	-15	3
0.05	$8.97 \times 10^{-11}$	$8.80 \times 10^{-11}$	0.9	-0.2
0.10	$2.46 \times 10^{-10}$	$2.03 \times 10^{-10}$	9	-2
0.14	$3.90 \times 10^{-10}$	$3.26 \times 10^{-10}$	8	-2
0.19	$7.41 \times 10^{-10}$	$5.58 \times 10^{-10}$	14	-3
0.20	$8.16 \times 10^{-10}$	$6.07 \times 10^{-10}$	14	-3
0.25	$1.35 \times 10^{-9}$	$1.09 \times 10^{-9}$	10	-2
0.30	$1.93 \times 10^{-9}$	$3.30 \times 10^{-9}$	-25	5

Table 4.4: Experimental and modeled activities of Ca vs. Ca(bcc) in Ca-Sb alloys at 800 °C via the regular association model and corresponding emf and  $\Delta\overline{G}_{\text{Ca}}$  error

by Sb atoms. The MIVM gives a different perspective of the same phenomenon by considering the first nearest neighbors of Ca and Sb and showing that Ca atoms are almost exclusively surrounded by Sb. Both models show therefore that there is a strong short-range order, that is Ca-centered, in Ca-Sb liquid alloys.

## 4.5 Conclusions of the chapter

The activity of Ca and the mixing properties of Ca-Sb liquid alloys were successfully modeled using the MIVM and the regular association model. These two models give a different perspective of the structure of the liquid alloys but agree on the type of structure, that is highly ordered:

- the association model, which is a “lattice” model, shows that Ca-Sb liquid alloys form  $\text{CaSb}_2$  associates, and that the alloys are almost a binary mixture of  $\text{CaSb}_2$  and Sb free atoms;

- the MIVM, which is fluid-based model, shows that the Ca atoms are almost completely surrounded by Sb atoms at the atomic level.

The structure of the liquid alloys, i.e., short-range order, is therefore directly related to the particularly low activity of Ca that was measured in the Ca-Sb liquid alloys.

For the first time, the MIVM was used successfully to model the thermodynamic



properties of liquid alloys in a system with high-melting intermetallics without making assumptions about the presence of an associate and decreasing the number of fit parameters from 5 to 2, offering an alternative to the commonly used regular associated model. These results are particularly important because the MIVM is also much easier to work with, since it has fewer parameters, and directly models the partial properties of mixing, which are the object of interest in this study.

The properties of other Ca-based liquid alloys with high-melting intermetallics are available in the literature, from the work of Delcet et al. Based upon the suitability of the MIVM to model Ca-Sb liquid alloys, these other alloys can potentially be modeled similarly.



# Chapter 5

## Interaction in calcium-based liquid alloys

This chapter focuses on the application of the MIVM, introduced in the last chapter in the case of Ca-Sb liquid alloys, to other calcium-based liquid alloys of systems with high-melting intermetallics, namely Ca-Ag, Ca-Bi, Ca-In, Ca-Pb, Ca-Sb, Ca-Sn, Ca-Tl, and Ca-Zn, as well as a system with a low-melting intermetallic Ca-Mg. Using the physical meaning of the interaction coefficients derived through the application of the MIVM to these alloys, a new mixing potential for liquid alloys will be proposed, that will allow one to compare the strength of interaction in different Ca-X liquid alloys.

## 5.1 Derivation of the interaction parameters in the MIVM

### 5.1.1 Input parameters: molar volume and first coordination number

The only input parameters in the MIVM correspond to properties of the pure liquid metals involved in the alloy, namely the molar volume,  $V_m$ , and the first coordination number,  $Z$ , in the liquid state [73]. These two parameters depend on the temperature of the liquid metal. For the molar volume, Iida and Guthrie [34] compiled a list with most liquid metals on it, including the temperature dependence of the molar volume of liquid metals, reported in Table 5.1 in the form:

$$V_m = V_{fus}(1 + \alpha_V(T - T_m)) \quad (5.1)$$

with  $V_{fus}$  the molar volume at the melting point and  $\alpha_V$  the coefficient of thermal expansion.

For the first coordination number,  $Z$ , the formula derived by Tao was used [77]:

$$Z = \frac{4\sqrt{2\pi}}{3} \left( \frac{r_m^3 - r_0^3}{r_m - r_0} \right) \frac{N_a}{V_m} r_m \exp \left( \frac{\Delta H_{fus}(T - T_m)}{Z_c R T T_m} \right) \quad (5.2)$$

This formula is based on the definition of the coordination number as twice the area under half of the first peak in the radial distribution function. The shape of the first peak in the radial distribution function near its melting point is approximated by a normal distribution, depending on the beginning ( $r_0$ ) and the first peak values ( $r_m$ ) of the radial distance, as it can be visualized on Figure 5-1. The temperature dependence of the radial distribution is assumed to decrease exponentially with increasing temperature, depending on the enthalpy of fusion  $\Delta H_{fus}$ .

Tao compared his predicted coordination number for metals with experimental values, estimated by Waseda [80] via the relationship between the radial distribution function and the structure factor obtained experimentally using x-ray and neutron

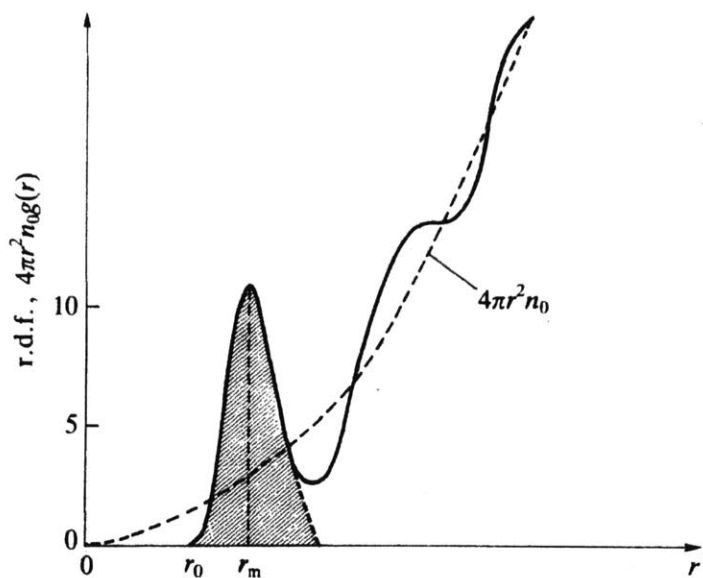


Figure 5-1:  $Z$  (shaded area) corresponds to the integral of the first peak of the radial distribution function (r.d.f), represented here in a typical case [34]

scattering data. To determine  $Z$ , different methods to compute the area under the first peak of the r.d.f. function can be used. Hines [31] reported that depending on the method used to construct the separate coordination shells (only the first shell should be included to obtain the first coordination number), the value determined for  $Z$  could vary by 20%. Waseda reported average values for the coordination numbers computed from the r.d.f. curve by three methods, to minimize the error. Tao found an average 6 % difference for all 39 metals considered between his estimation and the experimental values from Waseda [80]. Therefore, the precision obtained by Tao was deemed acceptable.

In all the metals of interest in this chapter, except Ca and Ag, the temperature dependence of the input parameters was taken into account. In the case of Ca and Ag, the values of the input parameters at the melting point were used even though the temperatures of interest ( $< 800\text{ }^{\circ}\text{C}$ ) was below their melting points.

The values used for the parameters necessary to compute  $Z$  and  $V_m$  of all the metals of interest in this chapter are reported in Table 5.1.

metal	$V_{fus}$ (m <sup>3</sup> /mol)	$\alpha_V$ (10 <sup>-4</sup> K <sup>-1</sup> )	$r_m$ (Å)	$r_0$ (Å)	$T_m$ (K)	$\Delta H_{fus}$ (kJ/mol)
Ag	11.6	0.98	2.89	2.46	1235	11.09
Bi	20.80	1.17	3.38	2.68	545	10.88
Ca	29.5	1.6	3.95	3.19	1115	8.40
In	16.3	0.97	3.33	2.64	430	16.30
Mg	15.3	1.6	3.20	2.50	923	8.80
Pb	19.42	1.24	3.50	2.70	601	4.81
Sb	18.8	1.3	3.14	2.57	904	39.70
Sn	17.0	0.87	3.16	2.59	505	7.07
Tl	18.00	1.15	3.43	2.72	577	4.31
Zn	9.94	1.5	2.79	2.30	693	7.28

Table 5.1: Input parameters for MIVM [34, 77]

### 5.1.2 Output parameters: the pair-potential energy interaction parameters $B_{ij}$

As reviewed in Chapter 4, Tao derived new expressions for the activity coefficients of  $i$  and  $j$  in a binary  $i-j$  alloy, that introduce only two pair-potential energy interaction parameters  $B_{ij}$  and  $B_{ji}$  [73].  $B_{ji}$  depends on the difference in energy for a  $j$  atom vs. an  $i$  atom next to a central  $i$  atom while  $B_{ij}$  depends on the difference in energy for an  $i$  atom vs. a  $j$  atom next to a central  $j$  atom.

$$\ln \gamma_i = \ln \left( \frac{V_{mi}}{x_i V_{mi} + x_j V_{mj} B_{ji}} \right) + x_j \left( \frac{V_{mj} B_{ji}}{x_i V_{mi} + x_j V_{mj} B_{ji}} - \frac{V_{mi} B_{ij}}{x_j V_{mj} + x_i V_{mi} B_{ij}} \right) - \frac{x_j^2}{2} \left( \frac{Z_i B_{ji}^2 \ln B_{ji}}{(x_i + x_j B_{ji})^2} + \frac{Z_j B_{ij} \ln B_{ij}}{(x_j + x_i B_{ij})^2} \right) \quad (5.3)$$

The activity coefficient of  $j$  is defined similarly. The interaction coefficients can therefore be obtained by fitting the activity coefficients obtained experimentally with these expressions. The values obtained for the interaction coefficients will differ slightly depending on the parameter minimized during the fitting and the method used to minimize this parameter.

### 5.1.3 Derivation of the interaction parameters

The parameter that was minimized through our fitting was the error on  $\ln(a_{\text{Ca}})$ . Tao minimized the error on  $a_{\text{Ca}}$  in his work, in which he was considering activities that were all in the same order of magnitude. However, in our case, the activities span several orders of magnitude. Also, the experimental values were obtained by emf measurements, whose measured values are directly related to  $\ln(a_{\text{Ca}})$  by the Nernst equation :  $E = -\frac{RT}{2F} \ln(a_{\text{Ca}})$ , with  $a_{\text{Ca}}$  the activity of calcium in the calcium alloy of interest. Therefore,  $\ln(a_{\text{Ca}})$  is a more relevant quantity in this case. The norm 2 of the error vector,  $err = (\sum_{i=1}^n (\ln(a_{\text{Ca,exp}}) - \ln(a_{\text{Ca,MIVM}}))^2)^{1/2} / n$ , with  $n$  the number of experimental datapoints, was chosen to be minimized.

The first method used to determine the interaction parameters was an algorithm developed in-house on MuPAD, the numerical solver of MATLAB. This iterative method was optimizing the interaction parameters by keeping one constant and optimizing the other one, then keeping the other constant and optimizing the first one to minimize  $err$ . During the first optimization, one of the parameters was varied by steps of 1, and the other parameter was optimized for each of these new values.  $err$  was compared at each one of these steps, and the solution for the interaction parameters that corresponded to the minimum of  $err$  was kept. The same scheme was performed with smaller steps of 0.1 and 0.01. The numerical routine was fairly simple and robust, however, one concern was that there might be several local minima in the  $err$  function, and that this program would only lead to the identification of one of these minima, depending on the starting values for  $B_{ij}$ , and not necessarily the global one.

Therefore, the second method used to obtain the interaction parameters was based on the study of  $err(B_{ij}, B_{ji})$ . By graphing the function in 3D, one would quickly see that there seemed to be only one minimum, a global one, as it can be seen in Figure 5-2 for instance in the case of Ca-Sn. This minimum could be identified by finding the values for which the partial differentials of  $err$  were equal to 0. The advantage of this more direct method, which was quick to run as well, was that it didn't require

to choose starting values, and the interaction parameters were given with a better precision, even though this didn't affect the value of the error that much, as the minimum of *err* was usually fairly flat. This second method was only possible because the function *err* was not too complicated and there was only one minimum.

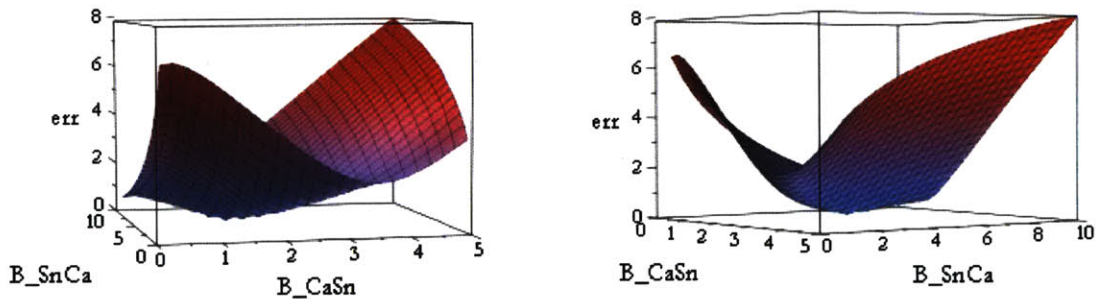


Figure 5-2: *err* for Ca-Sn liquid alloys at 800 °C (min for  $B_{CaSn} = 1.4587$  and  $B_{SnCa} = 5.9444$ )

The algorithms for both methods are available in the Appendix B in the case of Ca-Sn. The same algorithms were used for the other alloys of interest.

## 5.2 Results

### 5.2.1 Experimental data

Experimental data for most of the alloys (Ca-Ag, Ca-Bi, Ca-In, Ca-Pb, Ca-Sn, Ca-Tl, and Ca-Zn), were available from the extensive studies done at 800 °C by Delcet et al. [24, 23, 25] at Brookhaven National Laboratory. Delcet et al. obtained all these data by coulometric titration vs. a Ca-Bi (l) reference electrode through a single crystal  $CaF_2$  electrolyte, as mentioned for Ca-Sb in Chapter 3. In the case of Ca-Bi and Ca-Sb, these data were consistent with the emf measurements vs. Ca(s) through sintered  $CaF_2$  electrolyte, by H. Kim et al. [39] in the case of Ca-Bi, and from this work in the case of Ca-Sb. This gives confidence that the other data obtained by Delcet et al. are reliable. Additionally, the study by Kim et al. and the study presented in this thesis in the case of Ca-Sb provide data for an array of temperatures between



600 and 800 °C.

In the case of Ca-Mg, J. Newhouse et al. [48] measured at 1010 K the emf of Ca-Mg liquid alloys vs. a Ca-Bi(s + l) reference electrode using a similar set-up to the one presented in the case of Ca-Sb in this thesis.

In the case of Ca-Pb, additional experimental data at 900 °C were collected by Fray et al. [27] by coulometric titration vs. a Ca(l) reference electrode through solid calcium magnetoplumbite ( $\text{CaCO}_3$ ,  $\text{MgCO}_3$ , and  $\alpha\text{-Al}_2\text{O}_3$  with compositions varying from 1:0:6 to 1:0.6:6 molar proportions).

### 5.2.2 Interaction parameters

The values found for the interaction parameters and their corresponding temperatures are listed in Table 5.2, with the number of datapoints that were used for the fit. To evaluate the goodness of the fit, the average error in absolute value between the experimental emf and the modeled emf (since all the experimental data were obtained via emf measurements) is indicated. The error is low enough to be within experimental error (within less than 1 % of experimental values). The error in the partial Gibbs free energy of Ca, which is related to the emf by  $\Delta\bar{G}_{\text{Ca}} = -zFE$ , is also indicated. A plot of the modeled data vs. experimental data is available in Figure 5-3, data in Table 5.6 at the end of the chapter, with  $\Delta E$  the corresponding error for each composition.

As in the last chapter, the emf error  $\Delta E$  is defined for a cell of the type  $\text{Ca(s)} \mid \text{Ca}^{2+} \text{ conductor} \mid \text{Ca-X (l)}$ , in which the electrolyte is stable vs. the electrodes, and the transference number is one (the electrolyte is a pure ionic conductor), by:

$$\Delta E = E_{\text{MIVM}} - E_{\text{exp}} = -\frac{RT}{2F} \ln a_{\text{Ca,MIVM}} - \frac{RT}{2F} \ln a_{\text{Ca,exp}} = -\frac{RT}{2F} \ln \left( \frac{a_{\text{Ca,MIVM}}}{a_{\text{Ca,exp}}} \right) \quad (5.4)$$

All the Ca-X liquid alloys that had emf measurements at only one temperature (Ca-Ag, Ca-In, Ca-Mg, Ca-Sn, Ca-Tl, and Ca-Zn) were included in Tables 5.6 and 5.2.

The results for Ca-Pb, Ca-Bi and Ca-Sb, for which experimental data were available at several temperatures, will be presented separately in the next subsection.

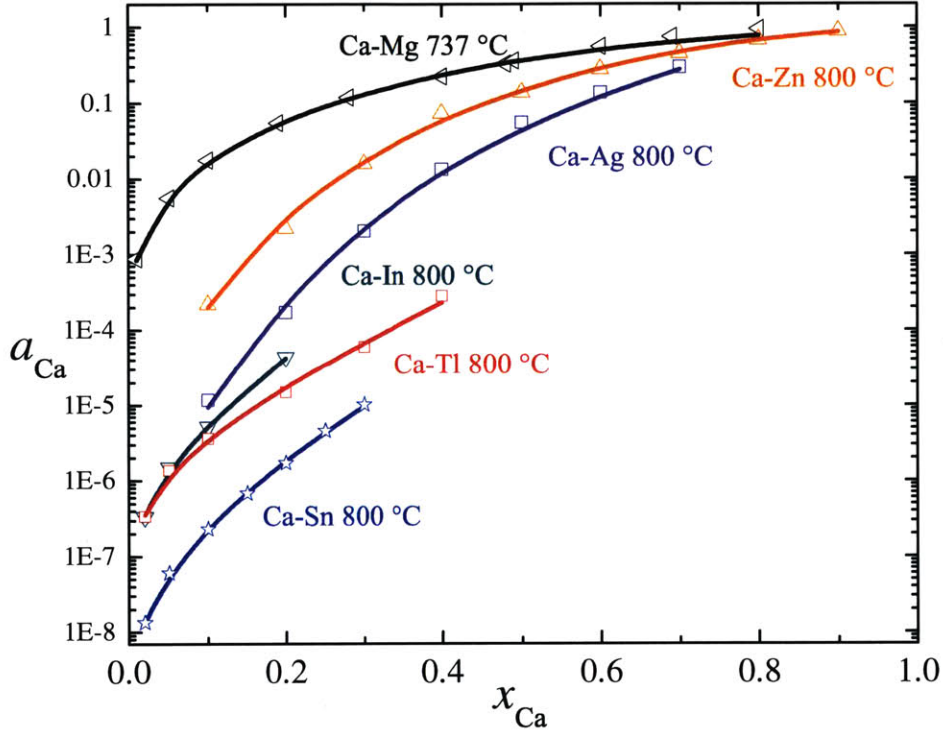


Figure 5-3: Ca activity in diverse Ca-X liquid alloys, experimental data represented by the empty symbols (Ca-Mg from [48], Ca-Zn from [25], Ca-Ag and Ca-In from [24], Ca-Tl from [23]), data modeled by the MIVM represented by the solid lines

X	T (K)	$B_{CaX}$	$B_{XCa}$	number of datapoints	average emf error (mV)	average $\Delta\overline{G}_{Ca}$ error (kJ/mol)
Ag	1073	1.8864	1.8698	7	$\pm 7.9$	$\pm 1.5$
In	1073	1.3861	3.6510	4	$\pm 2.9$	$\pm 0.6$
Mg	1010	1.5315	0.7197	11	$\pm 2.6$	$\pm 0.5$
Sn	1073	1.4587	5.9444	7	$\pm 2.3$	$\pm 0.4$
Tl	1073	1.1720	4.8600	6	$\pm 5.7$	$\pm 1.1$
Zn	1073	1.7269	1.2542	9	$\pm 3.8$	$\pm 0.7$

Table 5.2: Interaction parameters of Ca-X liquid alloys

### 5.2.3 Temperature dependence

The interaction coefficients depend on the temperature according to according to  $B_{ji} = \exp\left(-\frac{\epsilon_{ji}-\epsilon_{ii}}{kT}\right)$ , with  $\epsilon_{ji}$  the energy of a central  $i$  atom next to a  $j$  atom [73]. The temperature dependence for  $B_{ij}$  is defined similarly. Assuming a constant  $\epsilon_{ji} - \epsilon_{ii}$ , one can predict the values of the interaction coefficients of Ca-X liquid alloys at different temperatures. The accuracy of this expression (in particular of the assumption that the energy does not change over the range of temperature of interest), was tested in the case of Ca-Pb, Ca-Bi and Ca-Sb, for which experimental data were available at different temperatures.

In the case of Ca-Bi and Ca-Sb, the activity of Ca was modeled simultaneously at different temperatures:

- at 600 and 800 °C in the case of Ca-Bi;
- at 650 and 800 °C in the case of Ca-Sb.

These temperatures represent the boundaries of the temperature range for which the emf of the liquid alloys were measured. As seen on Figure 5-6, the temperature dependence of the activity is well represented by the MIVM when taking into account the temperature variation of the input parameters and of the interaction coefficients, keeping the  $\epsilon_{ji} - \epsilon_{ii}$  constant. The activity of Ca, experimental and modeled values, are available in Table 5.7 at the end of the chapter, with  $\Delta E$  the corresponding error for each composition.

In the case of Ca-Pb however, the activity of Ca could not be modeled simultaneously at 800 and 900 °C using the MIVM. This inconsistency between the 2 sets of data was already reported in the literature though, both by Fray et al. [27] and Cartigny et al. [21], who modeled the Ca-Pb system using a regular associated model with a  $\text{Ca}_2\text{Pb}$  associate. Cartigny et al. noted that, based on the results from his thermodynamic simulation, the results from Fray et al. were also not consistent with the data from Bouirden [13], who measured the liquidus temperature of Ca-Pb alloy for compositions close to  $\text{CaPb}_3$ , and chose to ignore the data from Fray to model the Ca-Pb system accurately. Based on the facts that the data measured by Delcet

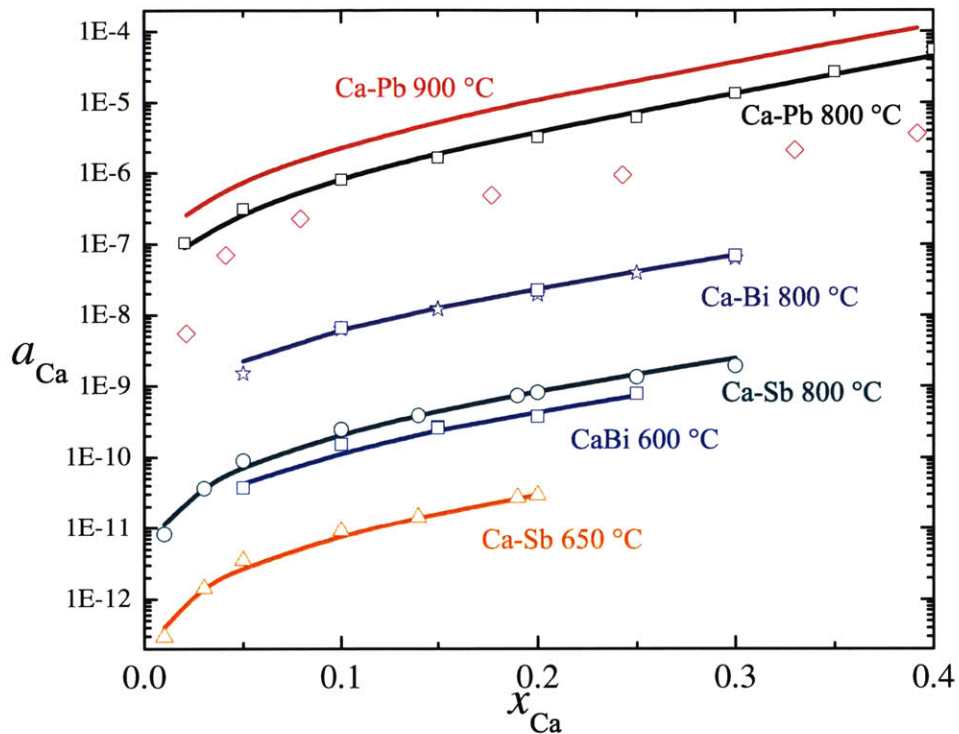


Figure 5-4: Ca activity in diverse Ca-X liquid alloys at different temperatures, experimental data represented by the empty symbols (Ca-Bi from [23] (stars) and [39] (squares), Ca-Sb from [57], Ca-Pb from [23] (squares) and [27] (diamond)), data modeled by the MIVM represented by the solid lines

et al. have been confirmed in the case of similar alloys such as Ca-Bi [39] and Ca-Sb [57], and also that the  $\text{Al}_2\text{O}_3$  used by Fray et al. in the magnetoplumbite could have reacted with  $\text{Ca}(l)$ , since  $\text{CaO}$  is much more stable than  $\text{Al}_2\text{O}_3$  at  $900\text{ }^\circ\text{C}$ , the data from Delcet were used here. Figure 5-6, the data from Fray are plotted with the prediction from the MIVM at that temperature, based on the data from Delcet et al. at  $800\text{ }^\circ\text{C}$  and the temperature dependence of the MIVM.

The values found for the interaction parameters in the Ca-Sb, Ca-Bi and Ca-Pb systems, and the corresponding temperature, are listed in Table 5.3, together the number of datapoints that were used for the fit and the average error in absolute value between the experimental emf and the modeled emf to evaluate the goodness

of the fit. The error in the partial Gibbs free energy of Ca is also indicated. The interaction coefficients that correspond to the same system but at different temperatures are interdependent. The fit at each individual temperature is as good as in the cases in Table 5.2, while the experimental data for each Ca-X system, at different temperatures, are still fitted with only two unknowns:  $(\epsilon_{XCa} - \epsilon_{CaCa})$  and  $(\epsilon_{CaX} - \epsilon_{XX})$ .

In the case of the liquid alloys of similar elements considered by Tao [75], the interaction coefficients have a value close to 1, and therefore do not vary much with temperature. In contrast, for the Ca-Sb and Ca-Bi alloys of the present study, the values of  $B_{SbCa}$  and  $B_{BiCa}$  exhibited significant variation with temperature and yet the MIVM accurately represents the quantitative nature of this variation. The temperature dependence of Tao's formulas could therefore be verified with confidence for the first time here.

X	T (K)	$B_{CaX}$	$B_{XCa}$	number of datapoints	average emf error (mV)	average $\Delta\bar{G}_{Ca}$ error (kJ/mol)
Bi	1073	1.1173	14.3925	10	$\pm 4.5$	$\pm 0.9$
	873	1.1461	26.5130	6	$\pm 6.3$	$\pm 1.2$
Sb	1073	1.1617	23.8839	9	$\pm 5.7$	$\pm 1.1$
	923	1.1903	40.0006	7	$\pm 5.9$	$\pm 1.1$
Pb	1073	1.1481	6.3354	9	$\pm 5.6$	$\pm 1.1$
	1173	1.1347	5.4128	7	$\pm 147$	$\pm 28$

Table 5.3: Temperature dependence of the interaction parameters in Ca-X liquid alloys

### 5.3 Definition of a mixing potential for liquid alloys

Based on the previous results, the MIVM is suitable to model the activity of Ca in all the Ca-X alloys of interest, that correspond to systems with high-melting intermetallics. Also, the temperature dependence of the MIVM is verified in the case of Ca-Bi and Ca-Sb, the only two systems that had reliable data at different temperatures. This suggests that  $(\epsilon_{XCa} - \epsilon_{CaCa})$ , the difference in energy for a Ca atom

surrounded by an X atom vs. a Ca atom, and  $(\epsilon_{\text{CaX}} - \epsilon_{\text{XX}})$ , the difference in energy for an X atom surrounded by a Ca atom vs. an X atom are indeed independent of temperature, and can be compared from one system to another.

To compare more easily the strength of interaction in the different Ca-X liquid alloys, a new parameter of mixing is proposed: a potential of mixing for liquid alloys,  $V_{\text{CaX}}$ , that uses the energy parameters derived from the MIVM,  $\epsilon_{ij}$ , that are independent of temperature.

$$V_{\text{CaX}} = \frac{1}{2}(\epsilon_{\text{XCa}} - \epsilon_{\text{CaCa}} + \epsilon_{\text{CaX}} - \epsilon_{\text{XX}}) = \frac{1}{2}(\epsilon_{\text{XCa}} + \epsilon_{\text{CaX}}) - \frac{1}{2}(\epsilon_{\text{CaCa}} + \epsilon_{\text{XX}}) \quad (5.5)$$

This expression is similar to the definition of the energy parameter in a regular solution model:  $W \propto (W_{AB} - (W_{AA} + W_{BB})/2)$ , that represents the difference in interaction energy between like and unlike neighbors. However, the formulation introduced here allows for an asymmetrical energy of interaction between Ca and X by introducing 2 potentially different values for the cross-energy terms  $\epsilon_{\text{XCa}}$  and  $\epsilon_{\text{CaX}}$ , depending on the central atom the energy corresponds to. The values for potential of mixing in liquid alloys in the Ca-X alloys of interest are reported in Table 5.4, and the ranking is represented in Figure 5-5. It should be noted that the order is exactly the same as the ranking of the OCV in Ca-X liquid metal batteries, for the same fraction of Ca in the positive electrode, as reported in Chapter 2 at 800 °C. The stronger the interaction, the larger the OCV.

All the values for the potential of mixing of the liquid Ca-X alloys considered here are negative, which corresponds to alloys that favor mixing. This is consistent with the fact that, in the liquid state, the activity of calcium shows a strong negative deviation from ideality (down to  $10^{-12}$  for Ca-Sb at 600 °C), indicating that Ca lowers greatly its energy when alloyed. The order of magnitude observed for the potential of mixing of ordered Ca-X liquid alloys is around 0.1 eV, which is an order of magnitude smaller than what is expected for  $W = \Delta H_f^0(AB_{\text{alloy}})/(x_A \times x_B)$  for an ordering system in the solid state, according to the regular solution model. This is consistent with the fact that interactions in the solid state are stronger than in the liquid state.

X	$V_{CaX}$ (eV)
Sb	-0.1537
Bi	-0.1285
Sn	-0.0999
Pb	-0.0918
Tl	-0.0805
In	-0.0750
Ag	-0.0583
Zn	-0.0357
Mg	-0.0042

Table 5.4: Potential of mixing of liquid Ca-X alloys

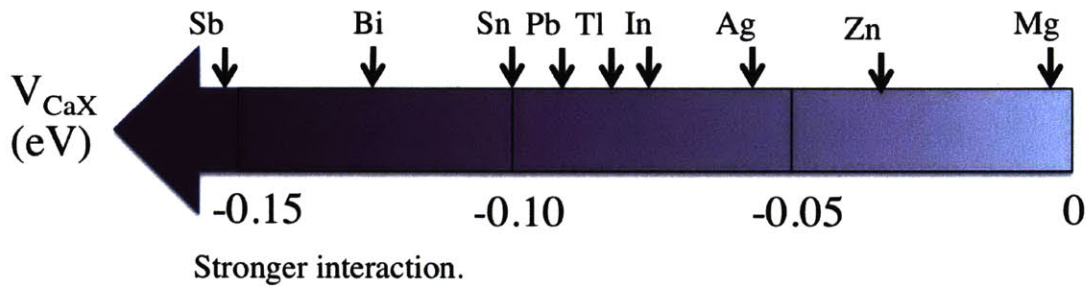


Figure 5-5: Ranking of the strength of interaction in liquid Ca-X alloys

In the case of Ca-Mg, which represents a system of very similar elements, the potential of mixing is very close to 0 (almost two orders of magnitude smaller than for Ca-Sb). For the alloys considered by Tao [75], the interaction coefficients  $B_{ij}$  were both close to 1, as in the case of Ca-Mg, and therefore the potential of mixing of the different binary alloys would all be close to zero. Here, the potentials of mixing are very different from one another, and follow a trend, that is visible in Table 5.4.

## 5.4 Analysis of the trend in $V_{CaX}$

### 5.4.1 Identification of the Ca-X systems of interest

The metals X of interest, that form Ca-X systems with high-melting intermetallics, do not lie on a row or column in the periodic table, as seen in Figure 5-6. There is no visible trend in the structural properties of X that correspond to the trend observed for the Ca-X systems of interest. However, the properties of liquid Ca-X alloys can

be compared to the interaction in the solid state of Ca-X systems.

1										18							
H	2											13	14	15	16	17	He
Li	Be											B	C	N	O	F	Ne
Na	Mg	3	4	5	6	7	8	9	10	11	12	Al	Si	P	S	Cl	Ar
K	Ca	Sc	Ti	V	Cr	Mn	Fe	Co	Ni	Cu	Zn	Ga	Ge	As	Se	Br	Kr
Rb	Sr	Y	Zr	Nb	Mo	Tc	Ru	Rh	Pd	Ag	Cd	In	Sn	Sb	Te	I	Xe
Cs	Ba		Hf	Ta	W	Re	Os	Ir	Pt	Au	Hg	Tl	Pb	Bi	Po	At	Rn

Figure 5-6: Periodic chart, with the elements of interest in this chapter in purple (Ca) and blue (X)

### 5.4.2 Enthalpy of formation of Ca-X intermetallics

The standard enthalpy of formation  $\Delta H_f^0$  of Ca-X intermetallics is an indication of the strength of interaction between Ca and X in the solid state. An estimate of the enthalpy of formation for most Ca-X intermetallics can be found in the literature. Most of the experimental data were measured at high temperature with a calorimeter [2, 43], by drop calorimetry [10] or by emf measurements [57]. Some of the enthalpies of formation were obtained from optimization of Ca-X phase diagrams [22, 21, 26, 37, 47, 54]. In some cases, the heat capacity coefficients have been optimized, allowing for a determination of the enthalpy of formation of the intermetallics at room temperature (Factsage data [4, 5]). When it wasn't the case, the Kopp-Newmann law was used. This law states that the molecular heat capacity of a solid compound is the sum of the atomic heat capacities of the elements composing it. Therefore, only the portion in the enthalpy of formation corresponding to a phase transformation of the pure metals had to be taken into account to estimate the enthalpy of formation of a compound at room temperature from data at high temperature.

The data collected from the literature are presented in Table 5.5. The method of determination (model or experiment) is in particular specified. In the case of



experimental data (indicated by exp), the experimental temperature is indicated. The values for the enthalpy of formation determined using different models ( $\text{Ca}_2\text{Sn}$ ), different experiment ( $\text{Ca}_5\text{Sb}_3$ ), or one model and one experiment ( $\text{Ca}_3\text{Sb}_2$ ), do not always agree, but are usually close enough to not affect the trend from one system to another.

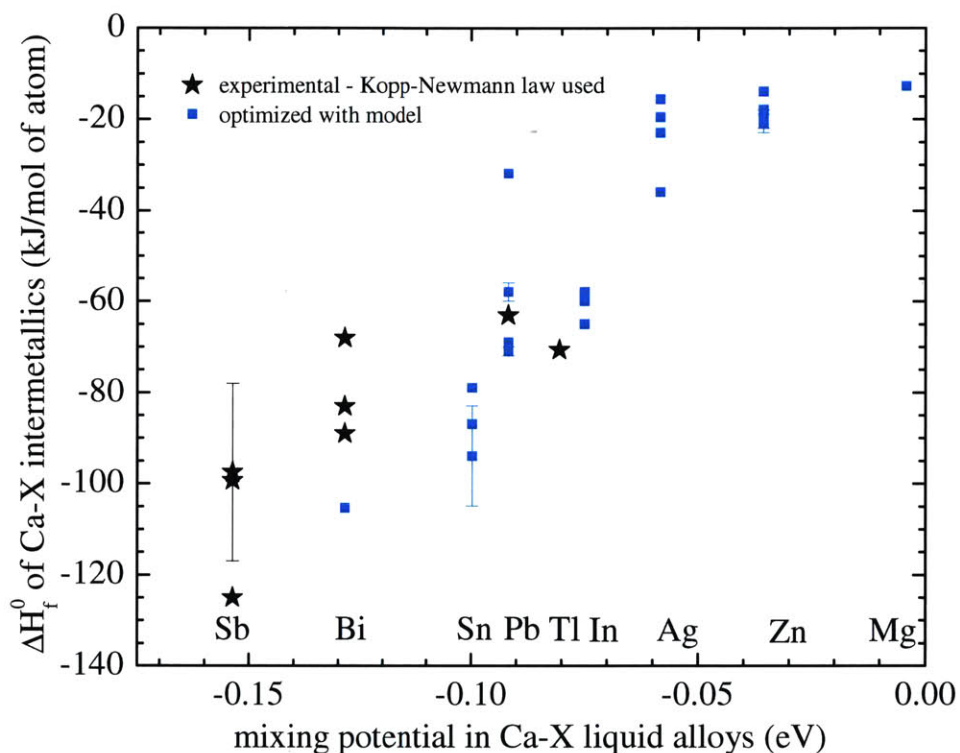


Figure 5-7: Interaction in the solid vs. liquid state for Ca-X systems with high-melting intermetallics

As seen on Figure 5-7, the systems with strong interaction in the solid state (ie. very stable intermetallics with very low enthalpy of formation) also have strong interaction in the liquid state, according to the definition of the potential of mixing in Ca-X liquid alloys.

intermetallic	$\Delta H_f^0$ (at 298K, kJ/mol of atom)	method	source
Ca <sub>11</sub> Sb <sub>10</sub>	-99	exp (1100 K)	[10]
Ca <sub>11</sub> Sb <sub>10</sub>	-100	exp (1073 K)	[57]
Ca <sub>5</sub> Sb <sub>3</sub>	-78	exp (1100 K)	[10]
Ca <sub>5</sub> Sb <sub>3</sub>	-117	exp (1073 K)	[57]
Ca <sub>3</sub> Sb <sub>2</sub>	-125	exp (933 K)	[43]
Ca <sub>3</sub> Sb <sub>2</sub>	-146	model	[4]
Ca <sub>11</sub> Bi <sub>10</sub>	-83	exp (1079 K)	[10]
Ca <sub>5</sub> Bi <sub>3</sub>	-68	exp (1079 K)	[10]
Ca <sub>3</sub> Bi <sub>2</sub>	-89	exp (903 K)	[43]
Ca <sub>3</sub> Bi <sub>2</sub>	-105	model	[4]
Ca <sub>2</sub> Sn	-83	model	[22]
Ca <sub>2</sub> Sn	-105	model	[4]
Ca <sub>5</sub> Sn <sub>3</sub>	-87	model	[22]
CaSn	-79	model	[4]
Ca <sub>2</sub> Pb	-63	exp (873 K)	[43]
Ca <sub>2</sub> Pb	-70	model	[21]
Ca <sub>2</sub> Pb	-72	model	[4]
CaPb <sub>3</sub>	-32	model	[21]
CaPb	-56	model	[21]
CaPb	-60	model	[4]
Ca <sub>5</sub> Pb <sub>3</sub>	-69	model	[21]
CaTl	-71	exp (903 K)	[43]
Ca <sub>3</sub> In	-58	model	[54]
CaIn	-65	model	[54]
CaIn <sub>2</sub>	-60	model	[54]
Ca <sub>2</sub> Ag <sub>9</sub>	-16	model	[26]
Ca <sub>2</sub> Ag <sub>7</sub>	-20	model	[26]
CaAg <sub>2</sub>	-23	model	[26]
Ca <sub>3</sub> Ag	-36	model	[26]
Ca <sub>3</sub> Zn	-14	model	[37]
Ca <sub>5</sub> Zn <sub>3</sub>	-21	model	[37]
CaZn	-23	model	[37]
CaZn	-18	model	[4]
CaZn <sub>2</sub>	-27	model	[37]
CaZn <sub>2</sub>	-22	model	[4]
CaZn <sub>3</sub>	-19	model	[37]
CaZn <sub>5</sub>	-19	model	[37]
CaZn <sub>11</sub>	-19	model	[37]
CaZn <sub>13</sub>	-18	model	[37]
CaMg <sub>2</sub>	-13	model	[2]

Table 5.5: Standard enthalpy of formation of intermetallics in Ca-X ordered systems

## 5.5 Conclusions of the chapter

The MIVM was used to model the activity of Ca in Ca-X liquid alloys, namely Ca-Ag, Ca-Bi, Ca-In, Ca-Pb, Ca-Sb, Ca-Sn, Ca-Tl, and Ca-Zn, and Ca-Mg. The agreement between the modeled data and the experimental data was within less than 1 % across the whole range of compositions. In the case of Ca-X systems with a high-melting intermetallic, data were available only for a limited range of compositions: the high X side of the intermetallic. This corresponds to the side of interest in this work since the application of this work is to use X as a positive electrode in a liquid metal battery, the composition of the liquid positive electrode would always be in the high X side of the Ca-X system.

The MIVM was also able to fit the activity of calcium over a large temperature range, as in the case of Ca-Sb and Ca-Bi, which confirms that the temperature dependence derived by Tao in the case of alloys of similar metals is also valid for alloys of very different metals. This allows one to predict the activity of Ca at several temperatures using data only obtained at one temperature, which is what is usually available for Ca-X alloys.

Using the energy coefficients of interaction derived by applying the MIVM to many Ca-X alloys with high-melting intermetallics, a new potential of mixing for liquid alloys was defined. This potential of mixing has a physical sense, and is in the right order of magnitude ( $V_{CaX} \approx -0.1$  eV) to represent the interaction in strongly interacting liquid alloys. This property could be related to the interaction in the intermetallics of the Ca-X systems. Indeed, systems with a stronger interaction in a solid state (i.e. which form stable intermetallics) have a stronger interaction in the liquid state (more negative  $V_{CaX}$ ).

This confirms that systems with high-melting intermetallics have more chances of corresponding to systems with low Ca activity in Ca-X liquid alloys, which in turn are attractive in LMBs. Indeed, high-melting intermetallics usually have very negative enthalpies of formation, corresponding to very stable intermetallics. And systems with a strong interaction in the solid state have a strong interaction in the liquid

state, as it was demonstrated in this chapter. Systems with very strong interaction in the liquid state (i.e. with very low  $V_{\text{CaX}}$ ), usually have lower Ca activities, as found through the MIVM.

After modeling the Ca-X systems in the liquid state, and having explained how strong candidates for X as a positive electrode in a LMB could be identified by looking at the interaction in the solid state, next chapter will be tackling the case of a binary positive electrode, and therefore looking at a Ca-X-Y alloy, chosen as Ca-Sb-Pb.

X	T (K)	$x_{Ca}$	$a_{Ca}$ (exp)	source	$a_{Ca}$ (MIVM)	$\Delta E$ (mV)	$\Delta \overline{G}_{Ca}$ error (kJ/mol)
Ag	1073	0.10	$1.87 \times 10^{-5}$	[24]	$0.95 \times 10^{-5}$	10	-2
		0.20	$1.72 \times 10^{-4}$	[24]	$2.51 \times 10^{-4}$	-17	3
		0.30	$2.05 \times 10^{-3}$	[24]	$2.37 \times 10^{-3}$	-7	1
		0.40	$1.33 \times 10^{-2}$	[24]	$1.25 \times 10^{-2}$	3	-0.6
		0.50	$5.53 \times 10^{-2}$	[24]	$4.51 \times 10^{-2}$	9	-2
		0.60	$1.37 \times 10^{-1}$	[24]	$1.24 \times 10^{-1}$	5	-0.9
		0.70	$2.98 \times 10^{-1}$	[24]	$2.76 \times 10^{-1}$	4	-0.7
In	1073	0.02	$3.36 \times 10^{-7}$	[24]	$3.49 \times 10^{-7}$	-2	0.3
		0.05	$1.53 \times 10^{-6}$	[24]	$1.38 \times 10^{-6}$	5	-0.9
		0.10	$5.20 \times 10^{-6}$	[24]	$5.69 \times 10^{-6}$	-4	0.8
		0.20	$4.37 \times 10^{-5}$	[24]	$4.26 \times 10^{-5}$	1	-0.2
Mg	1010	0.01	$8.78 \times 10^{-4}$	[48]	$8.44 \times 10^{-4}$	-2	0.3
		0.05	$5.56 \times 10^{-3}$	[48]	$5.96 \times 10^{-3}$	3	-0.6
		0.10	$1.76 \times 10^{-2}$	[48]	$1.72 \times 10^{-2}$	-1	0.2
		0.19	$5.43 \times 10^{-2}$	[48]	$5.46 \times 10^{-2}$	0.3	-0.05
		0.28	$1.19 \times 10^{-1}$	[48]	$1.17 \times 10^{-1}$	-1	0.1
		0.40	$2.23 \times 10^{-1}$	[48]	$2.38 \times 10^{-1}$	3	-0.5
		0.48	$3.28 \times 10^{-1}$	[48]	$3.37 \times 10^{-1}$	1	-0.3
		0.49	$3.62 \times 10^{-1}$	[48]	$3.50 \times 10^{-1}$	-1	0.3
		0.60	$5.52 \times 10^{-1}$	[48]	$5.00 \times 10^{-1}$	-4	0.8
		0.69	$7.42 \times 10^{-1}$	[48]	$6.25 \times 10^{-1}$	-8	1
		0.80	$8.62 \times 10^{-1}$	[48]	$7.71 \times 10^{-1}$	-5	0.9
Sn	1073	0.02	$1.33 \times 10^{-8}$	[23]	$1.37 \times 10^{-8}$	-1	0.2
		0.05	$6.06 \times 10^{-8}$	[23]	$5.55 \times 10^{-8}$	4	-0.8
		0.10	$2.32 \times 10^{-7}$	[23]	$2.36 \times 10^{-7}$	-1	0.2
		0.15	$6.83 \times 10^{-7}$	[23]	$7.18 \times 10^{-7}$	-2	0.4
		0.20	$1.73 \times 10^{-6}$	[23]	$1.86 \times 10^{-6}$	-3	0.7
		0.25	$4.58 \times 10^{-6}$	[23]	$4.40 \times 10^{-6}$	2	-0.4
		0.30	$1.02 \times 10^{-5}$	[23]	$9.77 \times 10^{-6}$	2	-0.4
Tl	1073	0.02	$3.42 \times 10^{-7}$	[23]	$3.57 \times 10^{-7}$	-2	0.4
		0.05	$1.39 \times 10^{-6}$	[23]	$1.18 \times 10^{-6}$	8	-2
		0.10	$3.69 \times 10^{-6}$	[23]	$3.71 \times 10^{-6}$	-0.3	0.06
		0.20	$1.51 \times 10^{-5}$	[23]	$1.83 \times 10^{-5}$	-9	2
		0.30	$6.01 \times 10^{-5}$	[23]	$6.80 \times 10^{-5}$	-6	1
		0.40	$2.85 \times 10^{-4}$	[23]	$2.33 \times 10^{-4}$	9	-2
Zn	1073	0.10	$2.22 \times 10^{-4}$	[25]	$2.00 \times 10^{-4}$	5	-0.9
		0.20	$2.25 \times 10^{-3}$	[25]	$2.84 \times 10^{-3}$	-11	2
		0.30	$1.60 \times 10^{-2}$	[25]	$1.65 \times 10^{-2}$	-1	0.3
		0.40	$7.44 \times 10^{-2}$	[25]	$5.77 \times 10^{-2}$	12	-2
		0.50	$1.39 \times 10^{-1}$	[25]	$1.45 \times 10^{-1}$	-2	0.3
		0.60	$2.82 \times 10^{-1}$	[25]	$2.86 \times 10^{-1}$	-1	0.1
		0.70	$4.55 \times 10^{-1}$	[25]	$4.72 \times 10^{-1}$	-2	0.3
		0.80	$6.80 \times 10^{-1}$	[25]	$6.76 \times 10^{-1}$	0.3	-0.05
		0.90	$8.92 \times 10^{-1}$	[25]	$8.64 \times 10^{-1}$	1	-0.3

Table 5.6: Experimental vs. modeled by the MIVM  $a_{Ca}$

X	T (K)	$x_{Ca}$	$a_{Ca}$ (exp)	source	$a_{Ca}$ (MIVM)	$\Delta E$ (mV)	$\Delta \overline{G}_{Ca}$ error (kJ/mol)
Bi	1073	0.05	$1.51 \times 10^{-9}$	[39]	$2.26 \times 10^{-9}$	-19	4
		0.10	$6.43 \times 10^{-9}$	[39]	$6.20 \times 10^{-9}$	2	-0.3
		0.10	$6.76 \times 10^{-9}$	[23]	$6.20 \times 10^{-9}$	4	-0.8
		0.15	$1.26 \times 10^{-8}$	[39]	$1.28 \times 10^{-8}$	-1	0.2
		0.15	$1.23 \times 10^{-8}$	[39]	$1.28 \times 10^{-8}$	-2	0.4
		0.20	$1.98 \times 10^{-8}$	[39]	$2.37 \times 10^{-8}$	-8	2
		0.20	$2.28 \times 10^{-8}$	[23]	$2.37 \times 10^{-8}$	-2	0.3
		0.25	$3.96 \times 10^{-8}$	[39]	$4.15 \times 10^{-8}$	-2	0.4
		0.30	$6.37 \times 10^{-8}$	[39]	$7.07 \times 10^{-8}$	-5	0.9
		0.30	$7.01 \times 10^{-8}$	[23]	$7.07 \times 10^{-8}$	-0.4	0.08
Bi	873	0.05	$3.75 \times 10^{-11}$	[39]	$4.28 \times 10^{-11}$	-6	1
		0.10	$1.53 \times 10^{-10}$	[39]	$1.17 \times 10^{-10}$	13	-2
		0.15	$2.68 \times 10^{-10}$	[39]	$2.38 \times 10^{-10}$	5	-1
		0.15	$2.61 \times 10^{-10}$	[39]	$2.38 \times 10^{-10}$	4	-0.8
		0.20	$3.78 \times 10^{-10}$	[39]	$4.34 \times 10^{-10}$	-6	1
		0.25	$7.97 \times 10^{-10}$	[39]	$7.43 \times 10^{-10}$	3	-0.6
Sb	1073	0.01	$8.15 \times 10^{-12}$	[57]	$1.14 \times 10^{-11}$	-15	3
		0.03	$3.65 \times 10^{-11}$	[57]	$3.94 \times 10^{-11}$	-3	0.7
		0.05	$8.97 \times 10^{-11}$	[57]	$7.55 \times 10^{-11}$	8	-2
		0.10	$2.46 \times 10^{-10}$	[57]	$2.13 \times 10^{-10}$	7	-1
		0.14	$3.90 \times 10^{-10}$	[57]	$3.92 \times 10^{-10}$	-0.2	0.04
		0.19	$7.41 \times 10^{-10}$	[57]	$7.46 \times 10^{-10}$	-0.3	0.06
		0.20	$8.16 \times 10^{-10}$	[57]	$8.41 \times 10^{-10}$	-1	0.3
		0.25	$1.35 \times 10^{-9}$	[57]	$1.48 \times 10^{-9}$	-4	0.8
		0.30	$1.93 \times 10^{-9}$	[57]	$2.50 \times 10^{-9}$	-12	2
		Sb	923	0.01	$3.00 \times 10^{-13}$	[57]	$4.02 \times 10^{-13}$
0.03	$1.44 \times 10^{-12}$			[57]	$1.39 \times 10^{-12}$	2	-0.3
0.05	$3.55 \times 10^{-12}$			[57]	$2.68 \times 10^{-12}$	13	-3
0.10	$9.19 \times 10^{-12}$			[57]	$7.59 \times 10^{-12}$	9	-2
0.14	$1.46 \times 10^{-11}$			[57]	$1.39 \times 10^{-11}$	2	-0.4
0.19	$2.75 \times 10^{-11}$			[57]	$2.64 \times 10^{-11}$	2	-0.4
0.20	$2.96 \times 10^{-11}$			[57]	$2.96 \times 10^{-11}$	-0.1	0.01
Pb	1073			0.02	$1.04 \times 10^{-7}$	[23]	$8.92 \times 10^{-8}$
		0.05	$3.13 \times 10^{-7}$	[23]	$2.84 \times 10^{-7}$	4	-0.9
		0.10	$8.04 \times 10^{-7}$	[23]	$8.53 \times 10^{-7}$	-3	0.5
		0.15	$1.66 \times 10^{-6}$	[23]	$1.92 \times 10^{-6}$	-7	1
		0.20	$3.24 \times 10^{-6}$	[23]	$3.87 \times 10^{-6}$	-8	2
		0.25	$6.21 \times 10^{-6}$	[23]	$7.34 \times 10^{-6}$	-8	1
		0.30	$1.35 \times 10^{-5}$	[23]	$1.35 \times 10^{-5}$	-0.1	0.02
		0.35	$2.70 \times 10^{-5}$	[23]	$2.46 \times 10^{-5}$	4	-0.8
		0.40	$5.51 \times 10^{-5}$	[23]	$4.48 \times 10^{-5}$	10	-2

Table 5.7: Experimental vs. modeled by the MIVM  $a_{Ca}$

# Chapter 6

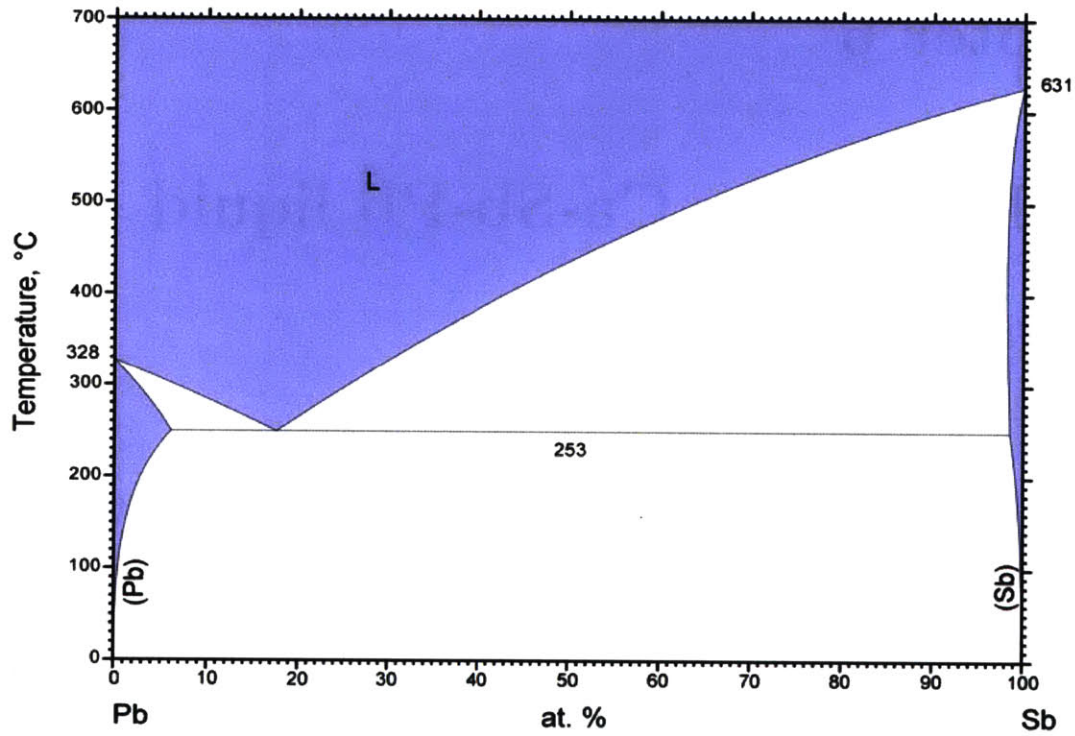
## Application to Ca-Sb-Pb liquid alloys

Based on the comparison between the interaction of Ca with Sb vs. other metals, Sb is the most attractive metal for a positive electrode in a Ca-based LMB: Ca-Sb liquid alloys have the lowest mixing potential in the liquid state, and the lowest Ca activity at a given temperature for a fixed Ca concentration, therefore Ca||Sb LMB have the highest OCV among the different Ca-based LMB.

Pb is a natural impurity of Sb. Indeed, primary Sb tends to concentrate in sulfide ores along with copper, lead, and silver, and secondary Sb is produced from lead-based alloys, and in particular from lead-acid batteries [18]. Hence the price of a Ca||Sb liquid metal battery could potentially be decreased by using a Sb-Pb positive electrode instead of a Sb positive electrode. This would particularly be interesting if the OCV could remain high. Therefore, the impact of Pb contamination on the activity of Ca is important to quantify. This chapter will focus on using the MIVM to predict the activity of Ca in Ca-Sb-Pb alloys. Emf measurements on select compositions of Ca-Sb-Pb alloys will allow the assessment of the prediction, and the difference will be interpreted.

Additionally, even though the operating temperature of a Ca||Sb battery is limited by the melting point of Ca, questions remain on whether the liquidus temperature of the positive electrode would be lowered or not in the case of a Pb-Sb alloy. Indeed,

the liquidus temperature of Pb-Sb alloys is lower than the melting temperature of pure Sb, as shown on the phase diagram in Figure 6-1, but the impact of Ca on this temperature is unknown. This impact will be assessed for select compositions of Ca-Sb-Pb alloys.



© ASM International 2009. Diagram No. 100246

Figure 6-1: Phase diagram of Pb-Sb alloys determined by Ohtani [51] from ASM International



## 6.1 Prediction of $a_{\text{Ca}}$ in Ca-Sb-Pb alloys

### 6.1.1 Application of the MIVM to ternary alloys

Tao derived a formula for the activity of each one of the components of a ternary alloy [73]. This formula is based on the assumption that the energy of a  $j$  atom next to a central  $i$  atom is the same in the presence or not of a  $k$  atom next to the  $i$  atom, taking only into account primary interactions. This allows Tao to use the coefficients derived from the studies of the binary systems to predict activity coefficients in ternary, quaternary, quinary... systems. Extending his new expression of the excess Gibbs energy of an  $i - j$  mixture to a multicomponent mixture (Equation 6.1), the activity coefficient of each species in a multicomponent mixture can be derived.

$$\frac{G_m^E}{RT} = \sum_{i=1}^n x_i \ln \underbrace{\frac{V_{mi}}{\sum_{j=1}^n x_j V_{mj} B_{ji}}}_{\text{local volume fraction of } i} - \frac{1}{2} \sum_{j=1}^n Z_i x_i \underbrace{\frac{\sum_{j=1}^n x_j B_{ji} \ln B_{ji}}{\sum_{k=1}^n x_k B_{ki}}}_{\text{energy interaction term}} \quad (6.1)$$

In our case, the activity of Ca in Ca-Sb-Pb liquid alloys is the quantity of interest, since this is the activity that will matter to determine the OCV of a Ca||Sb-Pb liquid metal battery. Therefore, in the rest of this chapter, only the activity of Ca will be modeled and compared to experimental data. However, the MIVM has the capability to model the activities of Sb and Pb as well.

### 6.1.2 Input parameters

To predict the properties of Ca-Sb-Pb alloys, the properties of Ca-Sb, Ca-Pb and Pb-Sb need to be optimized. Since the properties of Ca-Sb and Ca-Pb have been optimized in the previous chapter, only the properties of Pb-Sb need to be optimized here.

The experimental data used to optimize the Pb-Sb system was obtained by Sebkova et al. [66] by emf measurements using a molten salt electrolyte  $\text{PbCl}_2 + (\text{KCl}$

+ NaCl)(eutectic composition), where the emf signal of the Pb-Sb alloy vs. Pb(l) was recorded. Sebkova reported the emf of Pb-Sb alloys in the  $0.216 < x_{Pb} < 0.914$  range at 700, 750, and 800 °C. The properties both at 700 and 800 °C were used here to check the accuracy of the modeling regarding the temperature dependence. The results of the optimization are available in Figure 6-2 and Table 6.1, with the error for each datapoint. The average error obtain between the emf measured and the emf modeled was 0.8 mV. This corresponds to an error in the partial Gibbs free energy of Pb of  $\pm 0.1$  kJ/mol. The emf error is defined the same way as the previous chapter, but for a Pb(l) | Pb<sup>2+</sup> conductor | Pb-Sb (l) cell according to:

$$\Delta E = E_{\text{MIVM}} - E_{\text{exp}} = -\frac{RT}{2F} \ln a_{\text{Pb,MIVM}} - \frac{RT}{2F} \ln a_{\text{Pb,exp}} = -\frac{RT}{2F} \ln \left( \frac{a_{\text{Pb,MIVM}}}{a_{\text{Pb,exp}}} \right) \quad (6.2)$$

The interactions coefficients were found using the algorithm presented in Appendix B in the case of Ca-Sn. At 800 °C,  $B_{\text{PbSb}} = 0.8660$  and  $B_{\text{SbPb}} = 1.1916$ .

T (K)	$x_{\text{Pb}}$	$a_{\text{Pb}}$ [66]	$a_{\text{Pb}}$ (MIVM)	$\Delta E$ (mV)	$\Delta \bar{G}_{\text{Pb}}$ error (kJ/mol)
973	0.216	0.164	0.157	2	-0.3
	0.322	0.254	0.251	0.5	-0.1
	0.436	0.364	0.364	0.06	-0.01
	0.549	0.473	0.486	-1	0.2
	0.639	0.569	0.589	-1	0.3
	0.724	0.687	0.689	0.1	0.03
	0.807	0.795	0.787	0.4	-0.08
	0.914	0.902	0.909	0.3	0.07
1073	0.216	0.168	0.165	0.7	-0.1
	0.322	0.257	0.261	-0.7	0.1
	0.436	0.368	0.375	-0.9	0.2
	0.549	0.475	0.496	-2	0.4
	0.639	0.571	0.597	-2	0.4
	0.724	0.691	0.695	0.3	0.05
	0.807	0.796	0.790	0.3	-0.07
	0.914	0.905	0.910	0.3	0.05

Table 6.1: Experimental vs. modeled by the MIVM  $a_{\text{Pb}}$  in Pb-Sb liquid alloys

The energy parameters for Sb-Pb alloys are available in Table 6.2 along with the

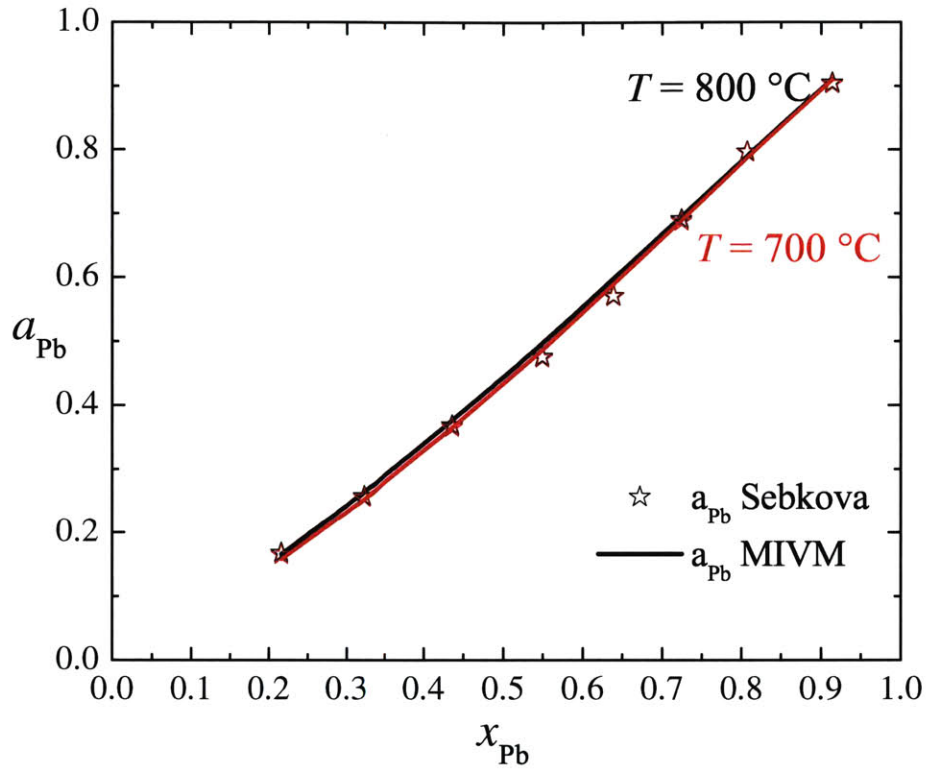


Figure 6-2:  $a_{Pb}$  in Sb-Pb liquid alloys at 700 and 800 °C, modeled by the MIVM and measured by Sebkova [66]

other energy parameters calculated for Ca-Sb and Ca-Pb. All are independent of temperature. These parameters, along with the properties of the pure metals from Table 5.1 are all the input parameters used to predict the activity of Ca in Ca-Sb-Pb liquid alloys.

j \ i	Ca	Sb	Pb
Ca	0	-0.2935	-0.1708
Sb	-0.0139	0	-0.0162
Pb	-0.0128	0.0133	0

Table 6.2:  $\epsilon_{ij} - \epsilon_{jj} = -kT \ln B_{ij}$  (eV)

### 6.1.3 Results

Based on the formula from Tao, the activity of Ca in Ca-Sb-Pb liquid alloys can be derived:

$$\begin{aligned}
 \ln \gamma_{\text{Ca}} = 1 + \ln & \frac{V_{m\text{Ca}}}{x_{\text{Ca}}V_{m\text{Ca}} + x_{\text{Sb}}V_{m\text{Sb}}B_{\text{SbCa}} + x_{\text{Pb}}V_{m\text{Pb}}B_{\text{PbCa}}} \\
 & \frac{x_{\text{Sb}}V_{m\text{Ca}}B_{\text{CaSb}}}{x_{\text{Ca}}V_{m\text{Ca}} + x_{\text{Sb}}V_{m\text{Sb}}B_{\text{SbCa}} + x_{\text{Pb}}V_{m\text{Pb}}B_{\text{PbCa}}} - \frac{x_{\text{Ca}}V_{m\text{Ca}}B_{\text{CaSb}} + x_{\text{Sb}}V_{m\text{Sb}} + x_{\text{Pb}}V_{m\text{Pb}}B_{\text{PbSb}}}{x_{\text{Pb}}V_{m\text{Ca}}} \\
 & - \frac{x_{\text{Ca}}V_{m\text{Ca}}B_{\text{CaPb}} + x_{\text{Sb}}V_{m\text{Sb}}B_{\text{SbPb}} + x_{\text{Pb}}V_{m\text{Pb}}}{x_{\text{Ca}}V_{m\text{Ca}}B_{\text{CaSb}} + x_{\text{Sb}}V_{m\text{Sb}} + x_{\text{Pb}}V_{m\text{Pb}}B_{\text{PbSb}}} \\
 & - 0.5 \left( Z_{\text{Ca}} \frac{(x_{\text{Sb}}B_{\text{SbCa}} + x_{\text{Pb}}B_{\text{PbCa}})(x_{\text{Sb}}B_{\text{SbCa}} \ln B_{\text{SbCa}} + x_{\text{Pb}}B_{\text{PbCa}} \ln B_{\text{PbCa}})}{(x_{\text{Ca}} + x_{\text{Sb}}B_{\text{SbCa}} + x_{\text{Pb}}B_{\text{PbCa}})^2} \right. \\
 & + \frac{Z_{\text{Sb}}x_{\text{Sb}}B_{\text{CaSb}} \left( (x_{\text{Sb}} + x_{\text{Pb}}B_{\text{PbSb}}) \ln B_{\text{CaSb}} - x_{\text{Pb}}B_{\text{PbSb}} \ln B_{\text{PbSb}} \right)}{(x_{\text{Ca}}B_{\text{CaSb}} + x_{\text{Sb}} + x_{\text{Pb}}B_{\text{PbSb}})^2} \\
 & \left. + \frac{Z_{\text{Pb}}x_{\text{Pb}}B_{\text{CaPb}} \left( (x_{\text{Sb}}B_{\text{SbPb}} + x_{\text{Pb}}) \ln B_{\text{CaPb}} - x_{\text{Sb}}B_{\text{SbPb}} \ln B_{\text{SbPb}} \right)}{(x_{\text{Ca}}B_{\text{CaPb}} + x_{\text{Sb}}B_{\text{SbPb}} + x_{\text{Pb}})^2} \right) \quad (6.3)
 \end{aligned}$$

Figure 6-3 represents the evolution of  $a_{\text{Ca}}$  with Ca increase in a Pb-Sb alloy of fixed ratio at 800 °C. This corresponds to the activity change that would be observed in the positive electrode of a Ca||Sb-Pb liquid metal battery during a discharge. The activity of Ca at other temperatures and compositions can be derived using the formula from Tao. If the alloy is in fact below its liquidus temperature in a solid + liquid phase, the predicted Ca activity will correspond to the metastable all-liquid Ca-Sb-Pb alloy, and not to the measured activity of Ca.

### 6.1.4 Interpretation of the results

The results show that the OCV of a Ca||Sb-Pb liquid metal battery would remain high because the interaction between Ca and Sb is stronger than the interaction between Ca and Pb. From the MIVM, the proportions of Ca, Sb, and Pb first neighbors of a central Ca atom can be determined. The proportions of Pb and Sb are equal for  $x_{\text{Pb}}/(x_{\text{Sb}} + x_{\text{Pb}}) = 0.79$ . This corresponds approximately to the

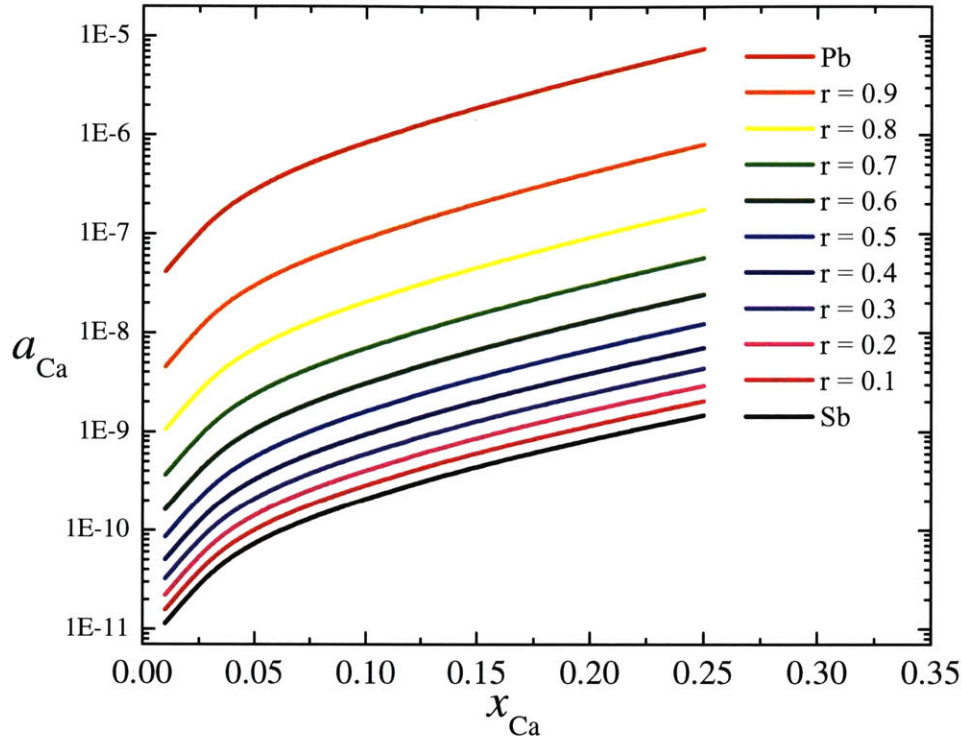


Figure 6-3: Prediction of  $a_{Ca}$  in Ca-Sb-Pb liquid alloys for fixed  $r = x_{Pb}/(x_{Sb} + x_{Pb})$  ratios at 800 °C

$x_{Ca}$ \ $x_{Pb}/x_{Sb}$	0.10	0.30	0.50	0.70	0.90
0.01	$1.55 \times 10^{-11}$	$3.21 \times 10^{-11}$	$8.52 \times 10^{-11}$	$3.61 \times 10^{-10}$	$4.49 \times 10^{-9}$
0.03	$5.35 \times 10^{-11}$	$1.11 \times 10^{-10}$	$2.96 \times 10^{-10}$	$1.26 \times 10^{-9}$	$1.58 \times 10^{-8}$
0.05	$1.03 \times 10^{-10}$	$2.14 \times 10^{-10}$	$5.71 \times 10^{-10}$	$2.45 \times 10^{-9}$	$3.09 \times 10^{-8}$
0.07	$1.65 \times 10^{-10}$	$3.45 \times 10^{-10}$	$9.25 \times 10^{-10}$	$3.99 \times 10^{-9}$	$5.08 \times 10^{-8}$
0.10	$2.90 \times 10^{-10}$	$6.08 \times 10^{-10}$	$1.64 \times 10^{-9}$	$7.16 \times 10^{-9}$	$9.23 \times 10^{-8}$
0.15	$6.13 \times 10^{-10}$	$1.29 \times 10^{-9}$	$3.53 \times 10^{-9}$	$1.57 \times 10^{-8}$	$2.07 \times 10^{-7}$
0.20	$1.15 \times 10^{-9}$	$2.45 \times 10^{-9}$	$6.78 \times 10^{-9}$	$3.07 \times 10^{-8}$	$4.16 \times 10^{-7}$
0.25	$2.03 \times 10^{-9}$	$4.35 \times 10^{-9}$	$1.23 \times 10^{-8}$	$5.69 \times 10^{-8}$	$7.89 \times 10^{-7}$

Table 6.3: Prediction of  $a_{Ca}$  at 800 °C in Ca-Sb-Pb liquid alloys using the MIVM

eutectic point in the Pb-Sb phase diagram (at  $x_{Pb} = 0.82$ ). When a Pb-Sb alloy with  $x_{Pb}/(x_{Sb} + x_{Pb}) < 0.79$  is used, the local environment of Ca is dominated by Sb atoms. The composition of the first nearest neighbors of Ca is plotted in Figure 6-4

for two different ratios of  $x_{\text{Pb}}/(x_{\text{Sb}} + x_{\text{Pb}})$ .

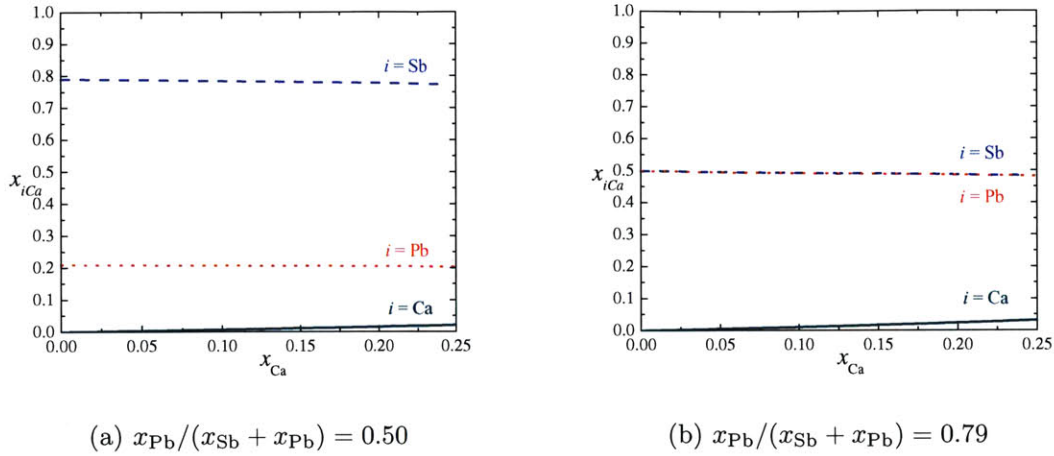


Figure 6-4:  $x_{i\text{Ca}}$ : fraction of first nearest neighbors of Ca of type  $i$

## 6.2 Comparison with experimental data

### 6.2.1 Selection of Ca-Sb-Pb compositions of interest

Based on the results, a substantial amount of Pb could be incorporated to Sb without lowering the emf too much. For  $x_{\text{Pb}}/(x_{\text{Sb}} + x_{\text{Pb}}) = 0.30$ ,  $a_{\text{Ca}}$  is one order of magnitude bigger than in pure Sb. This was chosen as a ratio of interest. Three concentrations of  $x_{\text{Ca}}$  were chosen: 0.05, 0.07 and 0.10. The concentration of Ca was chosen to be low enough to measure the emf of a fully liquid alloy, since the model can predict the activity of Ca only in this case.

### 6.2.2 Experimental set-up

The same emf set-up was used as in the case of Ca-Sb alloys. The emf of Ca-Sb-Pb alloys in a  $\text{Ca(s)}|\text{CaF}_2|\text{Ca-Sb-Pb (l)}$  cell is measured, at fixed concentrations, over a temperature range. The advantage of such a set-up over emf measurements via coulometric titration is that slope changes in the emf allow the identification of first order phase transitions (i.e. from l to s+l phase), while the coulometric titration

would not show such a transition. Indeed, in a ternary alloy, because the additional degree of freedom, the chemical potential of a s+l phase is not constant. It is only constant in the case of 3 phases at equilibrium. Therefore, in a coulometric titration, with a fixed  $x_{\text{Pb}}/(x_{\text{Sb}} + x_{\text{Pb}})$ ,  $a_{\text{Ca}}$  would be expected to vary with  $x_{\text{Ca}}$  in a s+l phase, making it indistinguishable from a pure liquid phase.

To prepare the alloys and ensure that the Pb/Sb ratio was the same as prepared, the Pb-Sb alloy was arc melted first, and then Ca was added. Indeed, Pb and Sb do not react heavily (they do not form intermetallics), and the ratio is kept constant. The weight of the samples before and after arc melting was also recorded, to ensure again that the evaporation of the Pb-Sb alloy (higher volatility) was minimal (less than 1 at% change).

### 6.2.3 Results

The emf results are shown in Figure 6-5. Apart from the activity of Ca that can be derived from these data, the liquidus temperature of these 3 alloys can be estimated by looking at the slope changes in the emf signal, following the same methodology as in Chapter 3. In this case, the measurements below the liquidus temperature are not as reproducible as in the liquid state. However, even with a  $\pm 10^\circ\text{C}$  error, the results for the liquidus Ca-Sb-Pb alloys for a fixed  $x_{\text{Pb}}/(x_{\text{Sb}} + x_{\text{Pb}}) = 0.30$  can provide interesting insight on the interaction in Ca-Sb-Pb alloys. Indeed, the increase in liquidus temperature in the  $0 < x_{\text{Ca}} < 0.10$  range suggests that the first eutectic point (for increasing % of Ca) in the Ca-(30Pb70Sb) phase diagram is below  $x_{\text{Ca}} = 0.05$ , while it was found around  $x_{\text{Ca}} = 0.14$  in the case of the Ca-Sb system. This shows that the Ca-Sb-Pb alloy enters a s+l phase at a lower Ca concentration than the Ca-Sb alloys, when adding Ca to Sb-Pb alloy, which is consistent with the fact that Ca interacts more with Sb than Pb.

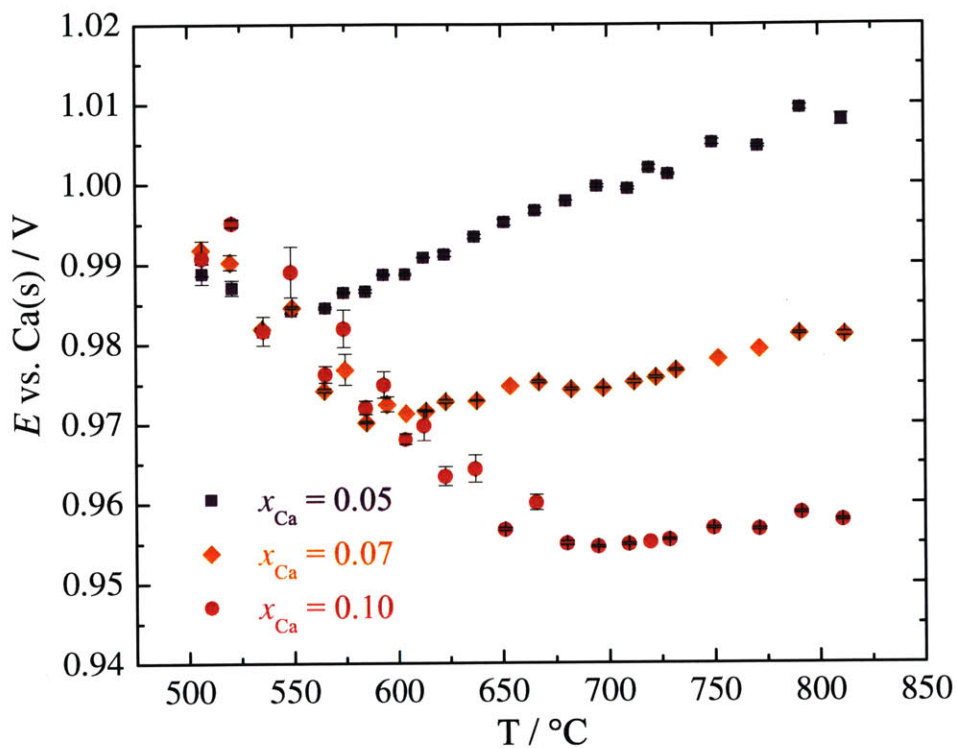


Figure 6-5: Emf vs. temperature data for  $\text{Ca(s)}|\text{CaF}_2|\text{Ca-Sb-Pb}$  cells, for  $x_{\text{Pb}}/(x_{\text{Sb}} + x_{\text{Pb}}) = 0.30$ , between 500 °C and 830 °C

$x_{\text{Ca}}$	$T_{\text{liq}}$ (°C) in Ca-Sb system	$T_{\text{liq}}$ (°C) in Ca-(30Pb70Sb) system
0	631	530 [51]
0.05	601	550
0.07	595	580
0.10	588	675

Table 6.4: Liquidus temperatures of Ca-Sb and Ca-(30Pb70Sb) alloys found by intersecting emf fitting lines



## 6.2.4 Comparison with predicted values

The comparison of the predicted emf vs. the measured emf is available in Table 6.5, for Ca-Sb-Pb liquid alloys between 650 and 800 °C. The temperature dependence of the emf is well reproduced. The predicted emf is on average 24 mV higher than the measured emf, which represents only a 2 % error. This corresponds an average error of 5 kJ/mol on the partial Gibbs free energy of Ca, while the error was 1 kJ/mol on average in the case of Ca-Pb and Ca-Sb. It suggests that as a first order approximation, the interaction is indeed dominated by first order interactions, and the MIVM predicts the activity of Ca in a Ca-Sb-Pb alloy rather well. However second order interactions are not completely negligible.

$x_{\text{Ca}}$	$T$ (°C)	emf predicted (V)	emf measured (V)	$\Delta E$ (mV)	$\Delta \bar{G}_{\text{Ca}}$ error (kJ/mol)
0.05	650	1.018	0.995	23	-4
	700	1.022	1.000	22	-4
	750	1.026	1.005	20	-4
	800	1.029	1.009	20	-4
0.07	650	0.999	0.975	25	-5
	700	1.002	0.974	27	-5
	750	1.005	0.978	26	-5
	800	1.007	0.981	26	-5
0.10	700	0.978	0.955	23	-4
	750	0.980	0.957	23	-4
	800	0.981	0.958	23	-4

Table 6.5: Emf in  $\text{Ca(s)}|\text{CaF}_2|\text{Ca-(30Pb70Sb)(l)}$  predicted by the MIVM, and measured by emf

## 6.3 Refinement of the modeling

### 6.3.1 Interpretation of the results at the atomistic level

When considering the different energy coefficients, and sorting them by type of central atom, as visualized in Figure 6-6, it appears that the difference of energy for a Sb or Pb atom next to a central Ca is much more important than in the case of a central Sb

surrounded by Ca and Pb or a central Pb surrounded by Ca and Sb. When considering a Sb or Pb central atom, the surrounding atoms have similar energy levels, as it is the case for alloys of similar elements, considered by Tao [74]. Tao showed that in that case, he could assume no effect from the presence of a ternary mixture on the energy levels obtained from binaries, and model accurately the ternary system. However, in the case of the environment of Ca, the energy level that corresponds to Sb is much lower than the energy level that corresponds to Pb, which is very different from what happened in the cases considered by Tao. A secondary type of interaction between Sb and Pb atoms that surround Ca atoms is therefore probable, that forces the energy levels of Sb and Pb to converge, making Sb less stable (less negative energy level), while Pb would gain stability from this interaction (more negative energy level). To test this hypothesis, the energy levels that correspond to the Ca environment will be allowed to vary to fit the experimental data, while the energy levels that correspond to the Sb and Pb environments will remain constant.

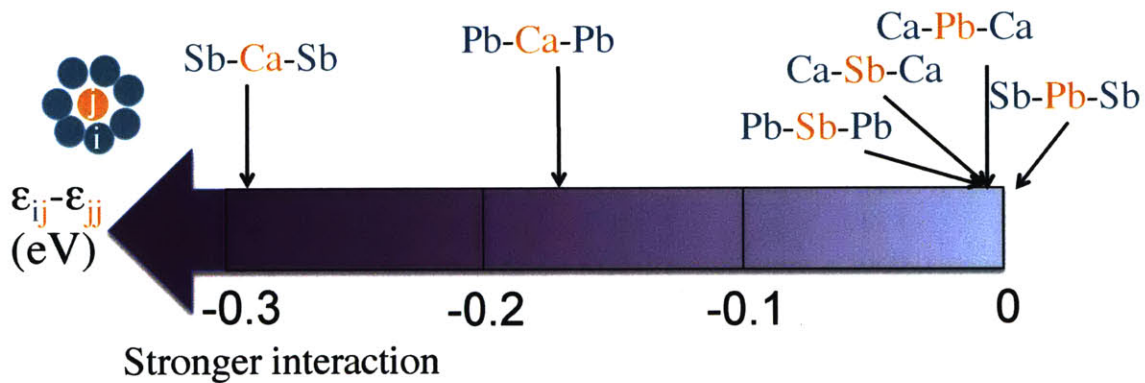


Figure 6-6:  $\epsilon_{ij} - \epsilon_{jj}$ , with  $j$  central atom (in orange) and  $i$  first nearest neighbor (in green)

### 6.3.2 Correction of the interaction coefficients around Ca

The activity of Ca at 700 and 800 °C was fitted successfully for the Ca-Sb-Pb alloys, whose properties were presented in the last section. The values for the energy levels found through this optimization are in Table 6.6.

Only  $(\epsilon_{SbCa} - \epsilon_{CaCa})$  and  $(\epsilon_{PbCa} - \epsilon_{CaCa})$  were changed, the other energy coefficients

	i	Ca	Sb	Pb
j		Ca	Sb	Pb
Ca		0	-0.2853	-0.1983
Sb		-0.0139	0	-0.0162
Pb		-0.0128	0.0133	0

Table 6.6:  $\epsilon_{ij} - \epsilon_{ji} = -kT \ln B_{ij}$  (eV). The parameters in black were derived from modeling of the binary systems, while the parameters in green were optimized in the ternary system

were kept constant. As the analysis was suggesting, the energy levels of Sb and Pb next to Ca are leveled in a Ca-Sb-Pb alloy. When correcting only these 2 energy levels, the difference was  $\pm 2$  mV between the modeled emf and the experimental emf, or  $\pm 0.4$  kJ/mol for  $\Delta\bar{G}_{Ca}$ .

$x_{Ca}$	$T$ (°C)	emf modeled (V)	emf measured (V)	$\Delta E$ (mV)	$\Delta\bar{G}_{Ca}$ error (kJ/mol)
0.05	650	0.993	0.995	-2	0.4
	700	0.998	1.000	-2	0.4
	750	1.002	1.005	-3	0.6
	800	1.007	1.009	-2	0.5
0.07	650	0.974	0.975	-1	0.08
	700	0.978	0.974	3	-0.6
	750	0.981	0.978	3	-0.6
	800	0.984	0.981	3	-0.7
0.10	700	0.954	0.955	-1	0.2
	750	0.956	0.957	-1	0.2
	800	0.958	0.958	0	0.03

Table 6.7: Emf in Ca(s)|CaF<sub>2</sub>|Ca-(30Pb70Sb)(l) measured by emf, and modeled after optimization of the energy levels of the first nearest neighbors of Ca

### 6.3.3 Interpretation of the new values for the energy parameters

To make sure that the difference in energy level was induced by the presence of a ternary mixture, and that it was not due to the fitting of the Ca-Sb and Ca-Pb data, the Ca-Sb and Ca-Pb data were reexamined with the new energy coefficients. Indeed, it was reported in Chapter 5 that the minimum of the  $err(B_{CaX}, B_{XCa})$  function, that

assessed the difference the emf measured and the emf modeled for the Ca-X liquid alloys of interest, was rather flat, allowing slightly different ( $B_{CaX}, B_{XCa}$ ) solution couples to have almost the same *err* value. However, there was a substantial difference between the data modeled by the new coefficients, and the experimental data:

- for Ca-Pb at 800 °C, the modeled data overestimate the emf of Ca-Pb liquid alloys measured by Delcet [23] by 80 mV (or 13%), which corresponds to an underestimation of  $\Delta\bar{G}_{Ca}$  by 16 kJ/mol.

- for Ca-Sb at 800 °C, the modeled data underestimate the emf of Ca-Sb liquid alloys measured in this work by 27 mV (or 3 %), which corresponds to an overestimation of  $\Delta\bar{G}_{Ca}$  by 5 kJ/mol.

From the MIVM, the proportions of Ca, Sb, and Pb first neighbors of a central Ca atom can be determined using the updated coefficients. The proportions of Pb and Sb around Ca are equal for  $x_{Pb}/(x_{Sb} + x_{Pb}) = 0.72$ , which is close to the value that was observed using the coefficients from the binary alloys.

## 6.4 Prediction of the activity of calcium for other Ca-Sb-Pb alloys

### 6.4.1 Emf measurements

Additional emf measurements for other Ca-Sb-Pb alloys were made in  $Ca(s) | CaF_2 | Ca-Sb-Pb$  cells. The Ca-Sb-Pb alloys were chosen outside the range of compositions used in the previous experiment. One sample had the same  $x_{Pb}/(x_{Sb} + x_{Pb}) = 0.3$  ratio, but at a higher Ca concentration:  $x_{Ca} = 0.15$ . The two others had different  $x_{Pb}/(x_{Sb} + x_{Pb})$  ratios (0.1 and 0.5), with a low  $x_{Ca} = 0.07$ .

The emf measurements are presented in Figure 6-7. The liquidus temperatures of the alloys can be derived from the slope changes, and are reported in Table 6.8. The liquidus temperature of the sample with  $x_{Pb}/(x_{Sb} + x_{Pb}) = 0.3$ , is higher than the liquidus temperatures of the previous samples that had a smaller  $x_{Ca}$ . Comparing the liquidus temperatures of the different samples with fixed  $x_{Ca} = 0.07$  shows again

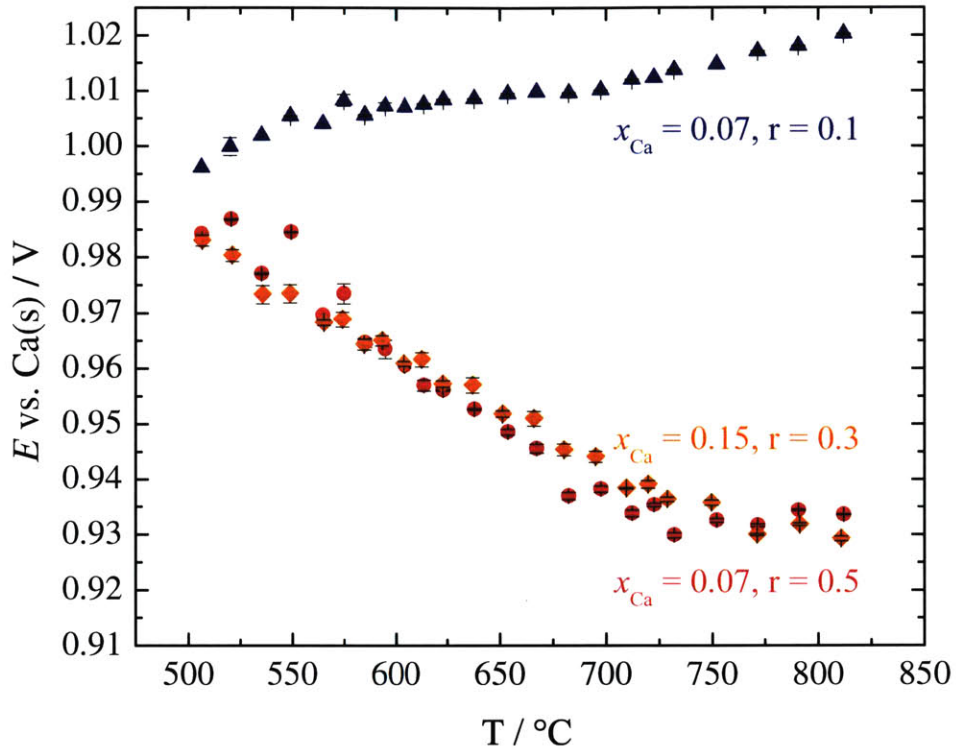


Figure 6-7: Emf vs. temperature data for  $\text{Ca(s)}|\text{CaF}_2|\text{Ca-Sb-Pb}$  cells, between 500 °C and 830 °C,  $r = x_{\text{Pb}}/(x_{\text{Sb}} + x_{\text{Pb}})$

that adding Pb to Sb, does not necessarily decrease the liquidus temperature of the Ca-Sb alloy, even though the liquidus temperature of Sb-Pb alloys is lower than the melting point of Sb. This is consistent with the fact that Ca interacts more with Sb than Pb.

Figure 6-8 represents the evolution of the liquidus temperature with the Ca, Sb and Pb concentrations based on the datapoints obtained from the 2 previous experiments.

### 6.4.2 Assessment of the prediction with corrected coefficients

Using the new energy coefficients derived from the fitting of emf data for 3 liquid Ca-Sb-Pb alloys, reported in Table 6.6, the emf in the  $\text{Ca(s)}|\text{CaF}_2|\text{Ca-Sb-Pb (l)}$  cells was predicted and the values were compared to the measured emf in Table

$x_{Ca}$	$x_{Pb}/(x_{Sb} + x_{Pb})$	$T_{liq}$ (°C)
0.07	0	595 [57]
	0.10	560
	0.30	580 (previous experiment)
	0.50	730
0.15	0.3	710

Table 6.8: Liquidus temperatures of Ca-Sb-Pb alloys found by intersecting emf fitting lines

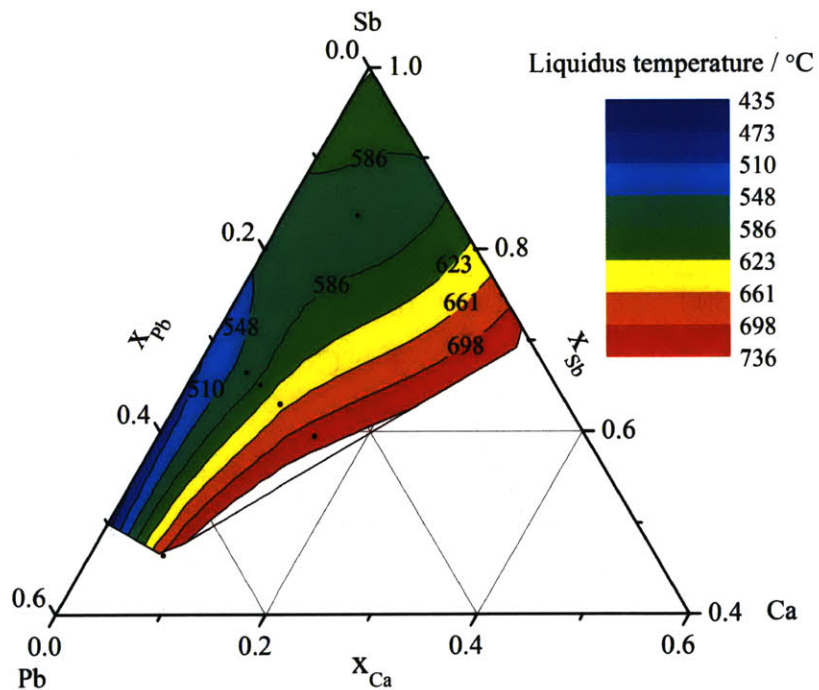


Figure 6-8: Liquidus temperature of Ca-Sb-Pb alloys. Experimental data obtained through this work represented by the black points

6.9. Because the liquidus temperatures of these alloys were on average higher than in the last experiment, some of the alloys have more datapoints to compare between predicted and measured values. On average, the emf error for these 3 alloys is  $\pm 6$  mV, or 0.6 % of the emf measured. This corresponds to an average error of 1 kJ/mol on  $\Delta\bar{G}_{Ca}$ .

$x_{Ca}$	$\frac{x_{Pb}}{(x_{Sb}+x_{Pb})}$	$T$ (°C)	emf predicted (V)	emf measured (V)	$\Delta E$ (mV)	$\Delta \overline{G}_{Ca}$ error (kJ/mol)
0.15	0.30	750	0.923	0.936	-13	-3
		800	0.923	0.930	-7	-1
0.07	0.10	650	1.003	1.008	-5	-1
		700	1.007	1.007	0	-0.002
		750	1.012	1.012	0	-0.07
		800	1.016	1.017	-1	-0.2
0.07	0.50	750	0.942	0.932	10	-2
		800	0.945	0.934	11	-2

Table 6.9: Emf in  $Ca(s)|CaF_2|Ca-Pb-Sb(l)$  measured by emf, and predicted by the MIVM, using the updated interaction coefficients

### 6.4.3 Results interpretation

With the new parameters, the Ca activity of Ca-Sb-Pb alloys of various compositions was corrected.

Figure 6-9 shows the values for  $a_{Ca}$  in different Ca-Sb-Pb alloys, comparing the measured activity and the modeled activity. The new coefficients, obtained after correction using only 3 compositions of Ca-Sb-Pb alloys, represent well the activity of Ca in the 6 Ca-Sb-Pb liquid alloys that have been considered. However, as it can be seen on Figure 6-9, the activity of Ca in the binary alloys Ca-Sb and Ca-Pb is not well represented with these coefficients. Therefore, this suggests that the difference for the energy coefficients is due to a secondary type of interaction between Sb and Pb, that are very similar (almost ideal solution), and can be exchanged easily around Ca. This type of interaction can only exist in the ternary alloy. It can be taken into account by looking at its impact on the primary type of interaction between the Ca and its first nearest neighbors, and correcting the corresponding coefficients accordingly.

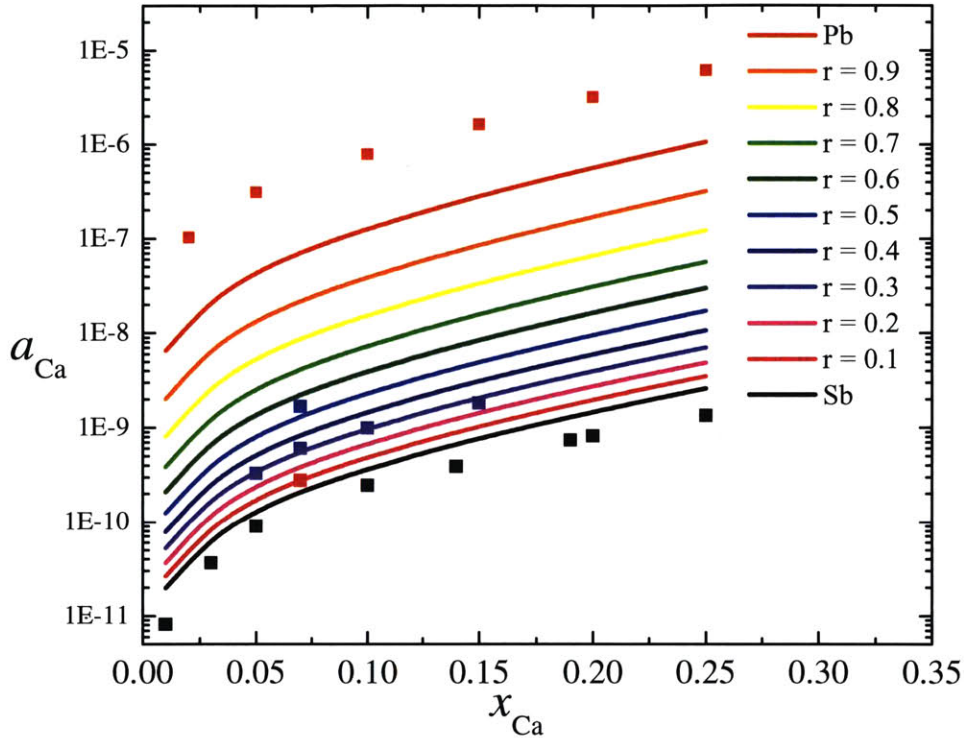


Figure 6-9:  $a_{\text{Ca}}$  in Ca-Sb-Pb liquid alloys at 800 °C for fixed  $r = x_{\text{Pb}}/(x_{\text{Sb}} + x_{\text{Pb}})$  ratios. The lines represent the data predicted by the MIVM after correction of the coefficients corresponding to the first nearest neighbors of Ca, and the squares represent the experimental data measured by emf. The data for Ca-Pb is from Delcet [23], the other datapoints were obtained from this work.

## 6.5 Conclusions of the chapter

The activity of Ca in Ca-Sb-Pb liquid alloys was modeled successfully using the MIVM. Assuming that the first nearest neighbors of Ca interact only with the center atom, not with each other, led to an overestimation of the emf measured in a Ca(s)|CaF<sub>2</sub>|Ca-Sb-Pb (l) cell. This overestimation was quantified as much as 2 % in the case of Ca-Sb-Pb liquid alloys with  $x_{\text{Pb}}/(x_{\text{Sb}} + x_{\text{Pb}}) = 0.3$ , which corresponds to an underestimation of  $\Delta\bar{G}_{\text{Ca}}$  by 5 kJ/mol. When taking into account the interaction between the first nearest neighbors of Ca by estimating its impact on the energy interaction between a Ca center atom and its nearest neighbors using the data ob-



tained for 3 alloys, the activity of Ca could be assessed more precisely. Using these updated coefficients, the activity of Ca for other compositions outside the range used for the fitting was evaluated with less than 0.6 % error in the corresponding emf, which corresponds to an average error of  $\Delta\overline{G}_{\text{Ca}}$  by 1 kJ/mol.

The modeling showed that Pb is an interesting candidate to alloy Sb with in a Ca||Sb-Pb liquid metal battery. Indeed, it would lower the cost of the positive electrode, while keeping a high voltage. This is due to the fact that the interaction between Ca and Sb stays much stronger than the interaction between Ca and Pb (and Ca and Ca), which leads to a non-random distribution of first nearest neighbors around Ca. This short-range order is characterized by a higher concentration of Sb than Pb, for the same nominal fraction in the alloy, while almost no Ca is located next to a Ca atom. Therefore, the properties of Ca, such as its activity are mainly governed by the Sb entourage, even though the impact of Pb cannot be neglected, keeping low  $a_{\text{Ca}}$  values, which translates into a high voltage Ca||Sb-Pb LMB. For instance, in the case of a Ca||Sb-Pb liquid metal battery with  $x_{\text{Pb}}/(x_{\text{Sb}} + x_{\text{Pb}}) = 0.3$ , the voltage drop would be less than 100 mV, which corresponds to only 10 % of the emf value.

The emf measurements revealed, however, that alloying Sb with Pb would not necessarily be interesting in the case of a liquid metal battery if the goal is to reduce the operating temperature, since the cycling range at a given temperature is expected to be smaller in the case of a Sb-Pb positive electrode than pure Sb electrode. For a Ca||Sb liquid metal battery at 710 °C, the maximal amount of calcium in the liquid positive electrode is close to  $x_{\text{Ca}} = 0.28$ , while a Ca||Sb-Pb liquid metal battery with  $x_{\text{Pb}}/(x_{\text{Sb}} + x_{\text{Pb}}) = 0.3$ , it would be  $x_{\text{Ca}} < 0.15$ , or half.



# Chapter 7

## Conclusion

### 7.1 Summary

#### 7.1.1 Main results

A thorough study of the thermodynamic properties of liquid Ca-Sb alloys was conducted, involving both emf measurements using a solid  $\text{CaF}_2$  electrolyte and thermodynamic modeling using the regular association model and the MIVM. The experimental results were consistent with the previous measurements by Delcet et al. [23]. The models applied to Ca-Sb liquid alloys were chosen for their capability to reveal the local structure of the Ca-Sb liquid alloys. The different approaches were reconciled in the case of Ca-Sb liquid alloys, showing that the low Ca activities (around  $10^{-10}$  for the temperature and compositions of interest), are related to the short-range order in liquid Ca-Sb alloys: Ca atoms are stabilized when surrounded by only Sb atoms.

For the first time, the MIVM was used in this work for compound-forming alloys, leading to experimental  $\Delta\bar{G}_{\text{Ca}}$  modeled with a 1 kJ/mol (0.6 %) precision. This model has the advantage of using only 2 physical parameters that need to be fitted, whereas the regular association model, the classical model for systems such as Ca-Sb with high-melting intermetallics, uses 5 parameters, and needs the input of the composition of the associate formed.

Based on the excellent modeling results for the Ca-Sb liquid alloys via the MIVM, the model was tested for other Ca-X systems that form high-melting intermetallics, namely Ca-Ag, Ca-Bi, Ca-In, Ca-Pb, Ca-Sb, Ca-Sn, Ca-Tl, and Ca-Zn, as well as a system with a low melting intermetallic Ca-Mg. The results were again excellent, with an error of 1kJ/mol on  $\Delta\overline{G}_{\text{Ca}}$ . Based on the definition of the interaction parameters in the MIVM, a new mixing potential in Ca-X liquid alloys was proposed. Comparing the trend observed for the mixing potential for Ca-X liquid alloys with the standard enthalpy of formation of the alloys in the corresponding systems, it was found that the systems that have the most stable intermetallics at room temperature are the systems with stronger short-range order in the liquid state.

The knowledge of binary Ca-Sb and Ca-Pb systems was then used in combination with the modeling of the Pb-Sb system to predict with a precision of 2 % the OCV of a Ca||Sb-Pb liquid metal battery using the MIVM. This corresponds to a precision of 5 kJ/mol on the partial Gibbs free energy of Ca in Ca-Sb-Pb alloys. The precision could be increased by a factor of 3 after running one test with select Ca-Sb-Pb compositions and refitting the interaction coefficients that corresponded to the interactions with Ca centered atom. To explain this need, the involvement of a secondary type of interaction between Sb and Pb first neighbors of Ca was evoked, since Sb and Pb are very similar atoms, as the modeling of the Sb-Pb system suggests. Therefore the large difference in energy for a Sb or a Pb atom next to a Ca atom is effectively decreased in the ternary mixture, as the modeling confirmed.

### 7.1.2 Application to Ca-based liquid metal batteries

This work on thermodynamic properties of Ca-based alloys was motivated by its application to Ca||X liquid metal batteries. Indeed, the OCV of a Ca-based liquid metal battery is directly related to  $\Delta\overline{G}_{\text{Ca}}$  and  $a_{\text{Ca}}$ , the activity of Ca and partial Gibbs free energy of Ca in Ca-X alloys, by the Nernst equation:

$$OCV = -\frac{\Delta\bar{G}_{Ca}}{2F} = -\frac{RT}{2F} \ln a_{Ca} \quad (7.1)$$

The experimental results for Ca-Sb liquid alloys showed that Sb was a particularly interesting candidate for a positive electrode, since it would provide an  $OCV > 0.95V$ . This value is particularly high compared to what can be expected for liquid metal batteries. By comparing the Ca-Sb system to other Ca-X systems with high-melting intermetallics, it was found that Ca-Sb was the system that would yield the highest OCV in a Ca-X liquid metal battery, due the strong short-range order in its liquid structure, which corresponds to the high stability of its intermetallics in the solid state.

Therefore, the experimental data obtained on Ca-Sb are particularly valuable, both experimental and in modeling, since they will provide the thermodynamic basis needed to assess the potential limitations of such a battery. Results were indeed obtained for an array of temperatures (all liquid for  $T > 800$  °C), over the entire range of compositions, expanding the small database available in the literature for this system.

Even though Sb is a cheap metal (\$1.8 /mol), with an estimated cost of energy for a Ca||Sb liquid metal battery of \$69 /kWh [40], alloying could decrease this price if the value of the OCV could be kept high. The element considered for alloying the Sb electrode was Pb. Indeed, Pb is substantially cheaper than Sb, and is expected to lower the price of the positive electrode even as an impurity, since Sb is usually produced with Pb impurity, especially when recycling the Sb from Pb-acid batteries. The MIVM predicted that the OCV would be kept high, which was confirmed by experimental analysis. Indeed, Ca is more stable when surrounded by Sb than Pb and in the presence of Sb and Pb atoms, the attraction between Ca and Sb dominates. This explains why the thermodynamic properties keep values close to what would be observed in the presence of Sb only.

An additional interest in Pb was motivated by the possibility of lowering the

melting point of the positive electrode. The few melting temperatures obtained for Ca-Sb-Pb alloys from emf experiments show that this would not necessarily be the case. In particular, adding Pb to Sb would decrease the all-liquid cycling range of the battery. Therefore, to work with an all-liquid positive electrode, the addition of Pb would be interesting if it stays only at an impurity level, which would probably not affect the voltage and the cycling range, but would still allow the use of a cheaper positive electrode.

## 7.2 Contributions

Beyond the field of liquid metal batteries, the present work has an appreciable impact for a wider scientific community.

### 7.2.1 Application of the MIVM for liquid alloys exhibiting short-range order

Beyond the case of Ca-X alloys, the MIVM was used for the first time for compound-forming alloys. This model constitutes a viable alternative to the regular association model with fewer parameters and assumptions than the regular association model. This makes the MIVM a model of choice to model compound-forming alloys. It has also the advantage of modeling directly the partial properties of mixing, which are often the properties measured, rather than the integral properties of mixing. Therefore, the additional errors due to the derivation of the integral properties of mixing can be avoided when modeling directly the data measured.

### 7.2.2 Definition of a new potential of mixing for liquid alloys

For systems that can be modeled by the MIVM, a new parameter of comparison was defined in this thesis, based on the interaction parameters obtained from the MIVM:

$$V_{ij} = \frac{1}{2}(\epsilon_{ij} - \epsilon_{jj} + \epsilon_{ji} - \epsilon_{ii}) = \frac{1}{2}(\epsilon_{ij} + \epsilon_{ji}) - \frac{1}{2}(\epsilon_{jj} + \epsilon_{ii}) \quad (7.2)$$

This potential of mixing for liquid alloys allows the comparison of the strength of short-range ordering.

### 7.2.3 Short-range order and stable intermetallics

The trend in the potential of mixing of the liquid alloys vs. the enthalpy of formation of the intermetallics in Ca-based systems demonstrated that a strong interaction in the solid state usually correlates with a strong interaction in the liquid state. By assessing the enthalpy of formation of the intermetallics of a system, one can therefore estimate the strength of interaction in the liquid state. This gives a physical basis to the selection of system for an application in the liquid state by looking at the solid state.

This work also identified which property should be considered in the solid state to predict the strength of the mixing in the liquid state. The standard enthalpy of formation of the intermetallics was found to be of value.

Stable intermetallics are usually associated with high-melting compounds. While this is true in some cases, and looking at a phase diagram will already give an idea of the strength of the intermetallics, it should be pointed out that the melting temperature depends also largely on the structure, and there is only correlation between enthalpy of formation and melting point if the alloys of interest share the same structure. An example is given in Figure 7-1 from [64].

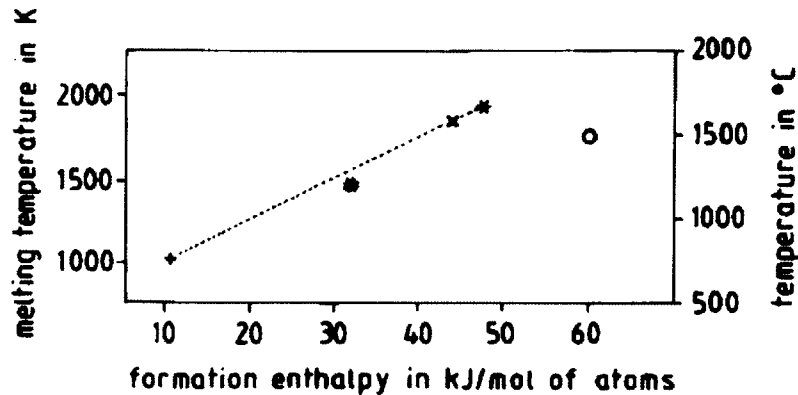


Figure 7-1: Melting temperature as a function of enthalpy of formation for the B2 phases CuZn (+), FeAl (#), CoAl (x), NiAl (\*), and for the L1 phase TiAl (o) [64]

## 7.3 Future work

### 7.3.1 Ternary systems

#### Phase diagrams

The work in this thesis revealed that the use of binary alloys for the liquid positive electrode could be interesting to lower the cost of the electrode without lowering the OCV of the liquid metal battery by much. However, a side result was that the cycling window of the battery would potentially be much smaller, reducing the quantity of positive electrode that would be utilized, and therefore increasing the price of the battery.

Based on the results, it seems that the limitation of the use of binary positive electrodes will be governed by the phase diagrams of the ternary Ca-based alloys of interest. It would indeed be crucial to assess the cycling window of the Ca-based liquid metal battery to be able to judge the feasibility of positive electrodes made of binary alloys. The phase diagrams of Ca-Sb-based ternary systems are expected to be challenging to obtain because of the difficulty to design a container that would not react with the alloy. Indeed, only very few ceramics, such as yttria, are barely more stable than calcia. Looking at nitrides, boron and aluminum nitride are supposedly more stable than calcium nitride. However, these materials are very hard to machine, without the addition of binders, which will react with calcium. Looking at metals, tungsten would be an option, but once again, small crucibles are quite difficult to obtain.

An alternative to solve the problem of the container could be the use of a container-free method, such as electrostatic levitation [33, 62]. Recent results have shown that it was an accurate method to determine phase diagrams by examining the cooling curves of a set of compositions of interest. This method has been used for instance in the case of the Ti-Zr-Ni ternary system [33]. Additional thermophysical properties can be obtained by this method, such as surface tension, viscosity, density, thermal expansion, vapor pressure, and specific heat, which could certainly be helpful to model



the battery.

### **Utilization of partially solid positive electrodes**

A fully liquid metal battery  $\text{Ca}||\text{Sb-Pb}$  would be of limited interest, because the battery would operate only at elevated temperatures, over a narrow range of compositions. However, this battery would be much more interesting if it could still operate with a partially liquid positive electrode, i.e., with some solid phase present.

Many challenges would need to be overcome for this to work, involving a complete understanding of the dynamics of the solid phase. Would it form a layer or pieces? Would it float, sink to the bottom, or form a mushy phase with the liquid? Would the calcium diffuse through the solid phase or only through the liquid phase? Would the solid phase be electrochemically inert or active?

### **7.3.2 Investigation of the Ca-based liquid metal batteries**

The work in this thesis aimed at selecting candidates candidates for a Ca-based liquid metal battery based on its OCV. Sb was the best candidate in that regard. Bi was second, but is a very expensive material, and Pb and Sn as a positive electrode would provide an OCV 40 % lower than Sb in a  $\text{Ca}||\text{X}$  liquid metal battery.

The OCV is a crucial parameter for the selection of candidates, in particular since for the same voltage losses, a system with a higher OCV will have a better efficiency, and store more energy. However, the inefficiencies will need to be quantified to assess if a Ca-based liquid metal battery is a good storage device.

### **Electronic conduction of the electrolyte - leakage current**

In an ideal battery, the electrolyte is a pure ionic conductor. However, in some cases, the molten salt serving as electrolyte is also an electronic conductor, and the leakage current is unacceptably high. The leakage current is due to the solubility of the metal in the electrolyte, and corresponds to the amount of current that passes between the electrodes without passing through an external circuit, resulting in the self-discharge,

and inefficiency of the battery.

For the emf study of the Ca-Sb liquid alloys, a solid and thick electrolyte was chosen, to prevent metal solubility. However, in a liquid metal battery, this is not an option, since the electrolyte would be a molten salt. A few solutions would reduce the amount of leakage current, i.e., the solubility of calcium in the electrolyte, such as:

- reducing the operating temperature, invoking Le Châtelier's principle;
- reducing the activity of calcium, by alloying it with an other metal, like Mg [48], invoking Le Châtelier's principle as well;
- tuning the composition of the electrolyte. Depending on the type of electrolyte, the solubility of calcium is more or less of an issue. For instance, Shaw et al. [67] measured that the solubility of calcium in  $\text{CaCl}_2$  at 800 °C was 2.7 at%, while it was reduced to 0.4 at% in a  $\text{CaCl}_2$ -CaO mixture with  $x_{\text{CaO}} = 0.09$ .

### **Determination of the passive components**

Other than the electrolyte, the materials such as the current collectors and an electrically insulating layer to prevent shorts between the electrodes, as present on Figure 2-3, will also need to be determined. In particular, sheaths may not be necessarily the most cost-effective solution to electrically insulate the electrodes for scale-up. Maybe a coating layer would be easier to scale-up.

The positive current collector will also need to be designed, keeping in mind that Sb alloys with most metals. Using tungsten as a material for the positive current collector would probably be too costly, which opens the question of the corrosion of other materials. Would the corrosion of other metals necessarily reduce service lifetime? Indeed, some materials may work long enough to be considered resistant to corrosion.

## Other inefficiencies

The efficiency of a liquid metal battery is also limited by other phenomena [6]:

- ohmic drop: it depends on the resistance of the electrolyte more than the resistance of the metals. By choosing a more or less resistant electrolyte, this parameter can be tuned.

- mass-transport in the electrodes: it depends on how fast the species can move from the bulk to the interface at which the reactions happen.

- charge-transfer at each molten salt | metal interface: it depends on how fast the charge transfer reaction happens. If the electrochemical reaction at the interfaces is charge transfer-limited, it means that the reaction is limited by at least one of the electron transfer steps (since in the case of Ca, 2 electrons need to be transferred).

All these rate processes depend also on the current density used. A complete study would have to be conducted to identify the highest inefficiencies, and to eventually optimize the Ca-based liquid metal batteries.

## 7.4 Perspectives

With emphasis on the Ca-based systems, and a particularly thorough study of the thermodynamic properties of Ca-Sb liquid alloys, the work in this thesis presents a simple criteria to select the electrodes to use in liquid metal batteries. The systems that have the most stable intermetallics in the solid state, which can be determined by looking at the enthalpy of formation per mole of alloy of the compounds of the system, will indeed provide the highest theoretical voltage when assembled as positive and negative electrodes of a liquid metal battery.

This criteria will allow rapid advances of liquid metal batteries, focusing on the systems that can potentially store the most energy. Other challenges remain, in particular designing the whole battery system around the most promising metal couples, keeping in mind that the application targeted for this system, grid-scale storage, is highly cost-sensitive.

Liquid metal batteries have the potential to change our energy future, allowing our

energy consumption to be disconnected from the energy production from intermittent sources, such as wind and solar. This work, by its direct application to the design of these batteries, will help select the best materials to fulfill this mission.

# Appendix A

## Standard operating procedure for the emf Ca-Sb cell preparation

The preparation of the different parts of the electrochemical cells, the  $\text{CaF}_2$  electrolyte and the Ca-Sb alloys, can be conducted simultaneously, and are necessary to be completed for the final assembly.

### A.1 Preparation of the $\text{CaF}_2$ electrolyte and caps

#### A.1.1 Safety precautions and personal protective equipment

Latex gloves, lab coat and safety glasses should be worn for all the stages of the preparation. When working with powder, a disposable mask should be worn as well.

#### A.1.2 Equipment and materials

**For the electrolyte + binder mixture preparation:**

- 500 g  $\text{CaF}_2$  99% Fisher Scientific
- 20 g polyvinyl alcohol (PVA) 99+%, hydrolyzed Sigma Aldrich
- 150 mL+ distilled water
- blender

- 30 cm × 19 cm pyrex dish
- spatula

**For the grinding steps:**

- spatula
- small mortar
- sieve (850  $\mu\text{m}$  mesh size)
- recipient for the powder (plastic bottle)

**For the preparation of the pellets:**

- hydraulic press
- 2 sets of dies: large set for electrolyte pellet (75 mm diameter), small set for caps (19 mm diameter).
- isopropanol
- isopropanol + 2wt% stearic acid
- dry electrolyte + binder mixture
- 0.4375 " (11 mm) diameter stainless steel drill bit for the electrolyte pellet
- 0.0635 " (1.6 mm) diameter carbide drill bit for the caps

### **A.1.3 Operating procedure**

**For the electrolyte + binder mixture preparation:**

1. mix the PVA with as little distilled water as possible.
2. add  $\text{CaF}_2$  in the blender 50 g by 50 g with the spatula, mixing with the blender and adding as little distilled water as possible to form a homogeneous mixture (goal: use only 150 mL distilled water).
3. pour the liquid mixture in the dish, forming a uniform layer.
4. let the mixture dry for 36-48 h in the fume hood to accelerate the drying process.

### **For the grinding steps:**

1. transfer some of the dry electrolyte mixture from the dish to the mortar with the help of the spatula.
2. grind the electrolyte until it is fine enough to go through the sieve.
3. repeat step 1 and 2 with all the electrolyte mixture.
4. store the ground electrolyte mixture in a plastic bottle.

### **For the preparation of the pellets:**

1. clean the die set with isopropanol, then lubricate the set with the isopropanol + stearic acid mixture.
2. for the electrolyte pellets (1 per experiment)
  - (a) weigh 150 g of dry electrolyte mixture.
  - (b) press the powder into a pellet using the large die set using 30,000 lb uniaxial pressure for 10 min.
  - (c) drill manually 7 wells 1 cm deep in the electrolyte pellet: 6 in an hexagon pattern and one in the center with the large drill bit.
3. for the caps (6 per experiment)
  - (a) weigh 6 g of dry electrolyte mixture.
  - (b) press the powder into a pellet using the small die set using 6,000 lb uniaxial pressure for 1.5 min.
  - (c) drill manually one hole all the way through the pellet, with the small drill bit, making sure that the drill bit goes through the pellets perpendicularly to the faces
4. fire the pellets
  - (a) place the green pellets on alumina plates in the furnace, separating the layers using alumina rings, with the caps on the top layers.
  - (b) heat the pellets at 120 °C for 12 h, 550 °C for 8 h and 1000 °C for 4 h.

## A.2 Preparation of the Ca-Sb samples

### A.2.1 Safety precautions and personal protective equipment

For the steps that are carried outside the Ar-filled glovebox ( $< 1$  ppm  $O_2$ ,  $< 0.1$  ppm  $H_2O$ ), latex gloves, a lab coat and safety glasses should be worn. Every step involving antimony outside of the glovebox requires the use of a respirator, because of the acute toxicity of the metal.

### A.2.2 Equipment and materials

#### Alloy preparation

- 6 glass vials, thread covered with PTFE tape
- calcium, distilled, dendritic pieces, 99.99% metals basis
- antimony shot, 6 mm and under, 99.999% metals basis
- electrical tape
- zirconium
- acetone

#### Sample machining

- mini-lathe
- hand drill
- 0.052 " (1.3 mm) diameter carbide drill bit

### A.2.3 Operating procedure

#### Alloy preparation

1. weigh 1 cm<sup>3</sup> of metals in the proportion of interest in the glovebox.
2. record the weight of each metal.
3. store each sample in a glass vial in the glovebox, cover the cap of the glass vial with electrical tape.



4. arc melt the samples:

- (a) clean the arc melter with acetone.
- (b) put the sample in one hole of the copper plate, and zirconium in another hole.
- (c) purge the chamber three times with argon.
- (d) arc melt under slightly negative pressure, starting with the zirconium that acts as an oxygen getter.
- (e) bring the sample back to the glovebox.
- (f) weight the sample.
- (g) repeat the procedure for all 6 samples.

### Sample machining

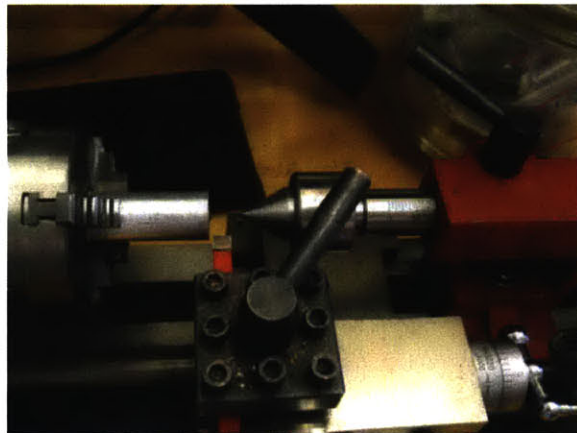


Figure A-1: Mini-lathe configuration for ductile sample machining

1. for ductile samples

- (a) prepare the mini-lathe in the configuration in Figure A-1.
- (b) mark the center of the sample with a drill bit or tweezers.
- (c) place the sample on the aluminium shaft, holding it firmly with the tip of the cone in the center of the sample.
- (d) use the lathe to remove the sides of the sample to get a cylinder of a bit less than 9 mm in diameter.

- (e) remove the aluminium shaft, flip the sample and place it in the spindle of the lathe.
  - (f) use the cone to mark the center of the cylinder.
  - (g) replace the cone by the drill bit holder.
  - (h) drill a hole all the way in the cylinder.
  - (i) remove the face of the sample with the lathe.
  - (j) flip the sample and remove the other side similarly.
2. for brittle samples
    - (a) drill a hole all the way through the sample with the hand drill.
    - (b) cut the sides with a plier to get a sample less than 9 mm in diameter.
    - (c) grind the sample slightly to remove the oxidation layer.
  3. sonicate each sample for 4 min in acetone.

## **A.3 Assembly**

### **A.3.1 Safety precautions and personal protective equipment**

For the steps that are carried outside the glovebox, latex gloves, a lab coat and safety glasses should be worn.

### **A.3.2 Equipment and materials**

- 7 alumina tubes (20 to 30 cm long) (check with multimeter that they are electrically insulated) 2/16 " ID, 4/16 " OD
- 7 ultra-torr Swagelok
- 7 viton o-rings (1/4 " ID, 3/8 " OD)
- 1 thermocouple type K
- 6 straightened tungsten wires (1 mm diameter) 99.95% Alfa Aesar 48 cm long
- insulation
- 1 alumina crucible 75 mm diameter, 26 mm high

- titanium sponge ( $O_2$  getter)
- stainless steel crucible and carrier
- sandpaper 600 grid
- Devcon 5 min epoxy
- electrolyte pellet
- 6 caps
- 6 samples
- $CaF_2$  powder 99% Fisher Scientific

### A.3.3 Operating procedure

#### Carrier preparation outside the glovebox

1. grind the thermocouple and W wires with the sandpaper.
2. clean with acetone the alumina tubes, crucible, as well as the thermocouple and W wires.
3. vacuum the powder that comes out of the insulation, and place it at the top of the carrier.
4. place the alumina crucible at the bottom of the carrier.
5. assemble the small o-ring and Swagelok at the top of the holes of the carrier.
6. pass the alumina tubes through the holes, then the W wires through the peripheral alumina tubes and the thermocouple through the center tube, so that the tip of the wires form a regular hexagon at the bottom of the alumina crucible.
7. seal the top of the alumina tubes with the epoxy.
8. place the titanium sponge at the bottom of the crucible.
9. place the large o-ring on the top of the crucible, then the carrier in the crucible and close the crucible.
10. check that the crucible is hermetically closed by pulling a vacuum down to 8 mtor.
11. transport to the glovebox.

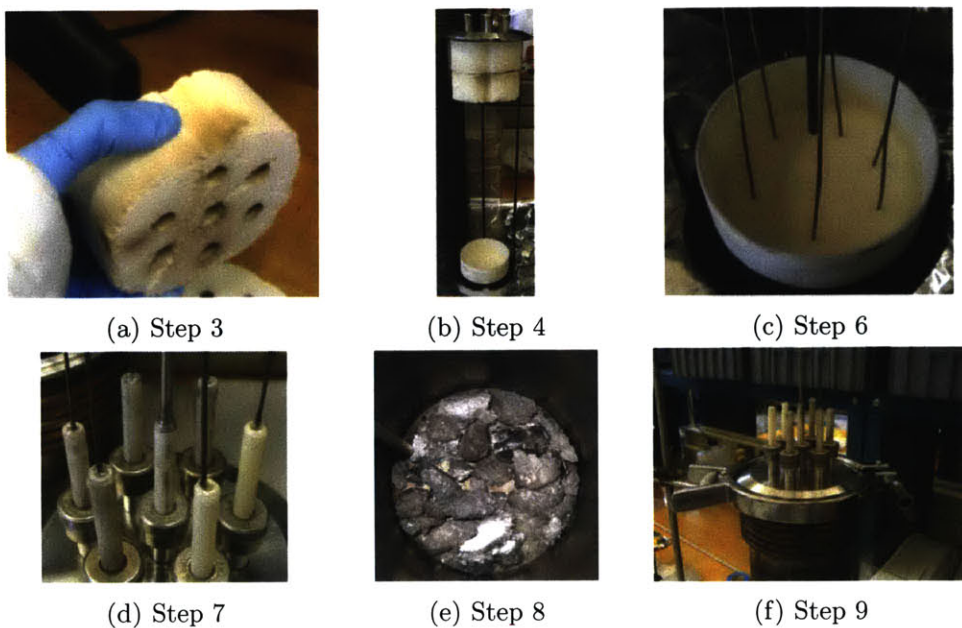


Figure A-2: Carrier preparation in open air

**Final assembly inside the Ar-filled glovebox (< 1 ppm O<sub>2</sub>, < 0.1 ppm H<sub>2</sub>O)**

1. place the electrolyte pellet in the alumina crucible.
2. place the electrodes in the electrolyte peripheral wells and label the cap of the crucible accordingly.
3. slip the caps on each tungsten wire and lower the wires in the holes of the electrodes.
4. with the spatula, add loose CaF<sub>2</sub> powder on top of the caps to cover all the electrolyte.
5. close the crucible.

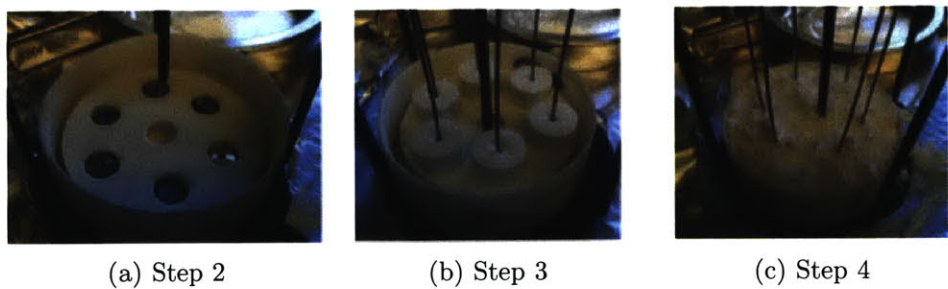


Figure A-3: Final assembly inside the Ar-filled glovebox, <1 ppm O<sub>2</sub>, < 0.1 ppm H<sub>2</sub>O

# Appendix B

## Algorithms for the determination of the MIVM coefficients of Ca-Sn alloys at 800 °C

### B.1 Coefficients determination via error minimization algorithm

definition of the constants: close packed coordination number, Avogadro's number, gas constant and temperature (in K)

```
reset():  
Zc:=12:  
Na:=6.022E23:  
R:=8.314472:  
cal:=4.184:  
T:=1073:
```

definition of a function that outputs the error between  $\ln(a_{Ca, exp}) - \ln(a_{Ca, modeled}) = \ln((a_{Ca, exp}) / (a_{Ca, modeled}))$ , given  $x=(a_{Ca, exp})$  and  $y=(a_{Ca, modeled})$  as inputs:

```
division_vector_line_ln:=proc(x,y)  
begin  
divi:=matrix(1,linalg::matdim(x)[2]):  
if linalg::matdim(x)[2]=linalg::matdim(y)[2]  
then for i from 1 to linalg::matdim(x)[2]  
do divi[i]:=ln((x[i]/y[i])):  
end_for  
end_if;  
divi;
```

Figure B-1: MuPAD algorithm 1

```
end_proc:
```

properties of pure metals, Ca and Sn  
rm: first peak value of the radial distance near Tm, in m  
r0: beginning value of the radial distance near Tm, in m  
deltaHm: enthalpy of melting, in J/mol  
Tm: melting temperature, in K  
Vm: molar volume of the liquid in m<sup>3</sup>/mol – T in K  
rho: molecular number density (in mol<sup>-1</sup>)=Na/Vm  
Z\_Tao: first coordination number in liquid metal, according to Tao's definition  
i: Ca  
j: Sn

```
rm_Ca:=3.95e-10:  
rm_Sn:=3.16E-10:  
r0_Ca:=3.19e-10:  
r0_Sn:=2.59E-10:  
deltaHm_Ca:=8.40e3:  
deltaHm_Sn:=7.07e3:  
Tm_Ca:=1115:  
Tm_Sn:=505:  
Vm_Ca:=29.54e-6:  
Vm_Sn:=17.0e-6*(1+0.87E-4*(T-Tm_Sn)):  
rho_Ca:=Na/Vm_Ca:  
rho_Sn:=Na/Vm_Sn:  
Z_Tao_Sn:=float(4*sqrt(2*PI)/3*((rm_Sn^3-r0_Sn^3)/(rm_Sn-r0_Sn))  
*rho_Sn*rm_Sn*exp(-deltaHm_Sn*(Tm_Sn-T)/(Zc*R*T*Tm_Sn))):  
Z_Tao_Ca_Tm:=10.32882247:  
Vmi:=Vm_Ca:  
Vmj:=Vm_Sn:  
Zi:=Z_Tao_Ca_Tm:  
Zj:=Z_Tao_Sn:
```

experimental data used for the fitting: activity measurements at 800C (Delcet's paper 1979)  
reference is Ca(s) for calculation of the activity coefficients.

```
x_Ca:=[0.02,0.05,0.10,0.15,0.20,0.25,0.30]:  
activity_Ca:=[1.3326E-08,6.0589E-08,2.3155E-07,6.8301E-07,1.7318E-06,4.5821E-06,1.0201E-05]:  
aCa_vsx:=transpose(matrix([x_Ca,activity_Ca])):
```

The activities of Ca and Sn will be calculated from the MIVM model every 0.01 from xCa=0.01 to xCa=0.30.

```
i:=2:  
x1_Ca:=0.01:  
while i<31  
do xi:=i/100:  
x1_Ca:=x1_Ca,xi:  
i:=i+1:  
end_while:  
x_Ca_2:=[x1_Ca]:
```

Through this program, the total error:  $\text{tot\_error} = 1/7 * (\text{sum}(\text{from } i=1 \text{ to } 7, [\ln(a_{Ca, \text{exp}}) - \ln(a_{Ca, \text{MIVM}})]^2)^{1/2}$   
will be determined, as well as the activity of Ca and Sn in the Ca-Sn alloys based on the interaction coefficients input.  
The activities of Ca and Sn are calculated based on the MIVM model, for xCa=0.01 to 0.30 by step of 0.01.  
The output are:  
activity of Ca: activity\_calc\_Ca\_matrix  
activity of Sn: activity\_calc\_Sn\_matrix  
tot\_error: total\_error

```
error_optimization:=proc(B_CaSn,B_SnCa)  
begin  
x1:=x_Ca_2;  
Mat := Dom::Matrix();  
activity_i:=Mat(1,30):
```

Figure B-1: MuPAD algorithm 1 (cont.)

```

activity_j:=Mat(1,30):
activity_j[1]:=1;
B_ij:=B_CaSn:
B_ji:=B_SnCa:

  for i from 1 to 30
    do j:=1-x1[i];
      gamma_:=exp(ln(Vmj/(x1[i]*Vmi+j*Vmj*B_ji))
+ j*(Vmj*B_ji/(x1[i]*Vmi+j*Vmj*B_ji)-Vmi*B_ij/(j*Vmj+x1[i]*Vmi*B_ij))
-(j^2)/2*(Zi*(B_ji^2)*ln(B_ji)/(x1[i]+j*B_ji)^2+Zj*B_ij*ln(B_ij)/(j+x1[i]*B_ij)^2));
      activity_i[i]:=gamma_*x1[i];
    end_for:

  for i from 1 to 30
    do j:=1-x1[i];
      gamma_:=exp(ln(Vmj/(j*Vmj+x1[i]*Vmi*B_ij))
+ x1[i]*(Vmi*B_ij/(j*Vmj+x1[i]*Vmi*B_ij)-Vmj*B_ji/(x1[i]*Vmi+j*Vmj*B_ji))
-(x1[i]^2)/2*(Zj*(B_ij^2)*ln(B_ij)/(j+x1[i]*B_ij)^2+Zi*B_ji*ln(B_ji)/(x1[i]+j*B_ji)^2));
      activity_j[i]:=gamma_*j;
    end_for:

calc_a_Ca:=[activity_i[2],activity_i[5],activity_i[10],activity_i[15],activity_i[20],activity_i[25],activity_i[30]];

activity_calc_Ca_matrix:=Mat(30,2):
for i from 1 to 30
do activity_calc_Ca_matrix[i,1]:=x_Ca_2[i]:
activity_calc_Ca_matrix[i,2]:=activity_i[i]:
end_for:

activity_calc_Sn_matrix:=Mat(30,2):
for i from 1 to 30
do activity_calc_Sn_matrix[i,1]:=x_Ca_2[i]:
activity_calc_Sn_matrix[i,2]:=activity_j[i]:
end_for:

error_aCa:=norm(division_vector_line_ln(matrix([calc_a_Ca]),matrix([activity_Ca])),2)/7:

total_error:=float(error_aCa);

return(activity_calc_Ca_matrix,activity_calc_Sn_matrix,total_error):

end_proc:

```

This program finds the  $B_{ij}$  that minimizes  $\text{tot\_error}(B_{ij}, B_{ji})$ , for a given  $B_{ji}$  by step of  $\text{step\_B}_{ij}$

```

optim_Bij:=proc(Bij,Bji,step_Bij)
begin
error_calc:=float(error_optimization(Bij,Bji)[3]):

Bij_2:=Bij+step_Bij:
error_Bij:=float(error_optimization(Bij_2,Bji)[3]):

if error_Bij<error_calc
then while (error_Bij<error_calc)
do error_calc:=error_Bij:
Bij:=Bij_2:
Bij_2:=Bij+step_Bij:
error_Bij:=float(error_optimization(Bij_2,Bji)[3]):
end_while
else Bij_2:=Bij-step_Bij:
error_Bij:=float(error_optimization(Bij_2,Bji)[3]):
if error_Bij<error_calc
then while error_Bij<error_calc
do error_calc:=error_Bij:
Bij:=Bij_2:
Bij_2:=Bij-step_Bij:

```

Figure B-1: MuPAD algorithm 1 (cont.)

```

        error_Bji:=float(error_optimization(Bji_2,Bji)[3]);
        end_while
    end_if

end_if:
return(Bji);
end_proc:

```

This program finds the Bji that minimizes tot\_error(Bji, Bji), for a given Bij by step of step\_Bji

```

optim_Bji:=proc(Bij,Bji,step_Bji)
begin
error_calc:=float(error_optimization(Bij,Bji)[3]);

Bji_2:=Bji+step_Bji;
error_Bji:=float(error_optimization(Bij,Bji_2)[3]);

if error_Bji<error_calc
then while error_Bji<error_calc
do error_calc:=error_Bji;
Bji:=Bji_2;
Bji_2:=Bji+step_Bji;
error_Bji:=float(error_optimization(Bij,Bji_2)[3]);
end_while
else Bji_2:=Bji-step_Bji;
error_Bji:=float(error_optimization(Bij,Bji_2)[3]);
if error_Bji<error_calc
then while error_Bji<error_calc
do error_calc:=error_Bji;
Bji:=Bji_2;
Bji_2:=Bji-step_Bji;
error_Bji:=float(error_optimization(Bij,Bji_2)[3]);
end_while
end_if

end_if:
return(Bji);
end_proc:

```

Through this program, both Bij (=B\_CaSn) and Bji (=B\_SnCa) are optimized at the same time.

The value of B\_CaSn is changed by steps of step\_1 (positive or negative value), and the value of B\_SnCa is changed by steps of step\_2 (positive or negative value). Using the 2 programs above, the initial value of B\_CaSn is changed by step1 to B\_CaSn\_2. Then B\_SnCa is optimized for the new B\_CaSn by step2, to B\_SnCa\_2

If the new error tot\_error(B\_CaSn\_2,B\_SnCa\_2) is smaller than the initial error, then the Bji values are reinitialized to the new values, and the same scheme is repeated.

In case the values for B\_CaSn\_2 and B\_SnCa\_2, calculated after the first step, give an error on tot\_error superior to the initial values for B\_CaSn and B\_SnCa, the program should be repeated using -step1 instead of step1.

```

Tao_optim:=proc(B_CaSn,B_SnCa,step1,step2)

begin
error1:=error_optimization(B_CaSn,B_SnCa)[3];
B_CaSn_2:=B_CaSn+step1;

B_SnCa_2:=optim_Bji(B_CaSn_2,B_SnCa,step2);
error2:=error_optimization(B_CaSn_2,B_SnCa_2)[3];

while error1>error2
do

```

Figure B-1: MuPAD algorithm 1 (cont.)



```

B_CaSn:=B_CaSn_2:
B_SnCa:=B_SnCa_2:

error1:=error_optimization(B_CaSn,B_SnCa)[3]:
B_CaSn_2:=B_CaSn+step1:

B_SnCa_2:=optim_Bji(B_CaSn_2,B_SnCa,step2):
error2:=error_optimization(B_CaSn_2,B_SnCa_2)[3]:

end_while:

print(B_CaSn,B_SnCa,error1):
end_proc:

```

A first value is tried, with large steps to get closer to the minimum faster.

```

Tao_optim(1,3,0.5,1)
1.5, 6, 0.1027960694

```

With the newer values, smaller steps are tried.

```

Tao_optim(1.5,6,0.1,0.2)
1.5, 6, 0.1027960694

```

```

Tao_optim(1.5,6,-0.1,0.2)
1.4, 6.2, 0.04564826621

```

```

Tao_optim(1.4,6.2,0.01,0.02)
1.46, 5.94, 0.02042495162

```

```

Tao_optim(1.46,5.94,0.01,0.01)
1.46, 5.94, 0.02042495162

```

```

Tao_optim(1.46,5.94,-0.01,0.01)
1.46, 5.94, 0.02042495162

```

The values for B\_CaSn and B\_SnCa found are therefore:

B\_CaSn=1.46±0.01  
B\_SnCa=5.94±0.01

To check that this makes sense, the activity of Ca from Delcet and the modeled values are plotted below:

```

activity_calc_Ca:=error_optimization(1.46,5.94)[1]:
plot(plot::Listplot(aCa_vsx,LinesVisible = FALSE),
plot::Listplot(activity_calc_Ca,PointsVisible =FALSE,LineStyle = Dashed,
Color = RGB::Purple,InterpolationStyle = Cubic),CoordinateType = LinLog,
AxesTitles = ["x_Ca", "a_Ca"]):

```

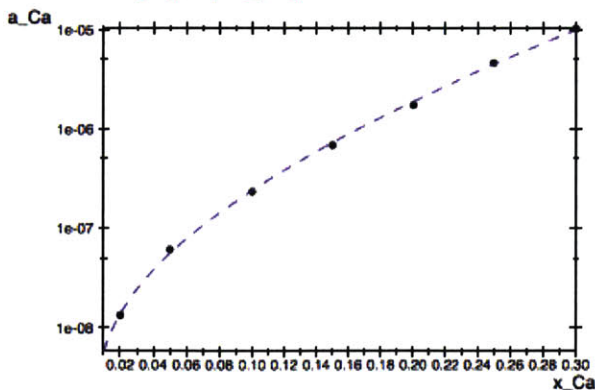


Figure B-1: MuPAD algorithm 1 (cont.)

## B.2 Coefficients determination using partial differentials

definition of the constants: close packed coordination number, Avogadro's number, gas constant and temperature (in K)

```
reset():  
Zc:=12:  
Na:=6.022E23:  
R:=8.314472:  
T:=1073:
```

properties of pure metals, Ca and Sn

rm: first peak value of the radial distance near Tm, in m

r0: beginning value of the radial distance near Tm, in m

deltaHm: enthalpy of melting, in J/mol

Tm: melting temperature, in K

Vm: molar volume of the liquid in m<sup>3</sup>/mol - T in K

rho: molecular number density (in mol<sup>-1</sup>)=Na/Vm

Z\_Tao: first coordination number in liquid metal, according to Tao's definition

i: Ca

j: Sn

```
rm_Ca:=3.95e-10:  
rm_Sn:=3.16E-10:  
r0_Ca:=3.19e-10:  
r0_Sn:=2.59E-10:  
deltaHm_Ca:=8.40e3:  
deltaHm_Sn:=7.07e3:  
Tm_Ca:=1115:  
Tm_Sn:=505:  
Vm_Ca:=29.54e-6:  
Vm_Sn:=17.0e-6*(1+0.87E-4*(T-Tm_Sn)):  
rho_Ca:=Na/Vm_Ca:  
rho_Sn:=Na/Vm_Sn:  
Z_Tao_Sn:=float(4*sqrt(2*PI)/3*((rm_Sn^3-r0_Sn^3)/(rm_Sn-r0_Sn))  
*rho_Sn*rm_Sn*exp(-deltaHm_Sn*(Tm_Sn-T)/(Zc*R*T*Tm_Sn))):  
Z_Tao_Ca_Tm:=10.32882247:  
Vmi:=Vm_Ca:  
Vmj:=Vm_Sn:  
Zi:=Z_Tao_Ca_Tm:  
Zj:=Z_Tao_Sn:
```

experimental data used for the fitting: activity measurements at 800C (Delcet's paper 1979)  
reference is Ca(s) for calculation of the activity coefficients.

```
x_Ca:=[0.02,0.05,0.10,0.15,0.20,0.25,0.30]:  
activity_Ca:=[1.3326E-08,6.0589E-08,2.3155E-07,6.8301E-07,1.7318E-06,4.5821E-06,1.0201E-05]:
```

calculation of ln(a\_Ca):

```
ln_activity_Ca:=[0,0,0,0,0,0,0]:  
for i from 1 to 7  
do ln_activity_Ca[i]:=ln(activity_Ca[i]):
```

Figure B-2: MuPAD algorithm 2

```
end_for:
aCa_vsx:=transpose(matrix({x_Ca,activity_Ca}));
```

MIVM:  $\ln a$  is the expression of  $\ln(a_{Ca})$  as a function of the metal properties and the interaction coefficients  $B_{ij}$  and  $B_{ji}$   
 $d\ln a_{ij}$  is the partial derivative of  $d(\ln a)/d(B_{ij})$   
 $d\ln a_{ji}$  is the partial derivative of  $d(\ln a)/d(B_{ji})$

```
xi:=x_Ca:
xj:=1-xi:
lna:=(i,B_ij,B_ji)->ln(xi[i])+ln(Vmi/(xi[i]*Vmi+xj[i]*Vmj*B_ji))+xj[i]
*(Vmj*B_ji/(xi[i]*Vmi+xj[i]*Vmj*B_ji)-Vmi*B_ij/(xj[i]*Vmj+xi[i]*Vmi*B_ij))
-(xj[i]^2)/(2*(Zi*(B_ij^2)*ln(B_ij)/(xi[i]+xj[i]*B_ji)^2+Zj*B_ij*ln(B_ij)/(xj[i]+xi[i]*B_ij)^2):

dlna_ij:=(i,B_ij,B_ji)->-xj[i]*(Vmi/(Vmj*xj[i]+B_ij*Vmi*xi[i])-(B_ij*Vmi^2*xi[i])/(Vmj*xj[i]+B_ij*Vmi*xi[i])^2)
-(xj[i]^2*(Zj/(xj[i]+B_ij*xi[i])^2+(Zj*ln(B_ij))/(xj[i]+B_ij*xi[i])^2
-(2*B_ij*Zj*xi[i]*ln(B_ij))/(xj[i]+B_ij*xi[i]^3)))/2:

dlna_ji:=(i,B_ij,B_ji)->xj[i]*(Vmj/(Vmi*xi[i]+B_ji*Vmj*xj[i])-(B_ji*Vmj^2*xj[i])/(Vmi*xi[i]+B_ji*Vmj*xj[i])^2)
-(xj[i]^2*(B_ji*Zi/(xi[i]+B_ji*xj[i])^2+(2*B_ji*Zi*ln(B_ji))/(xi[i]+B_ji*xj[i])^2
-(2*B_ji^2*Zi*xj[i]*ln(B_ji))/(xi[i]+B_ji*xj[i]^3)))/2
-(Vmj*xj[i])/(Vmi*xi[i]+B_ji*Vmj*xj[i]):
```

In this case, the properties of Ca in Ca-Sn liquid alloys were only measured for 7 compositions. For each composition, the activity from the model, as a function of interaction coefficients, and the experimental activity from Delcet's measurement can be compared.

Each group of functions (1 to 7) concerns one specific composition.

The goal is to minimize the difference between the  $\ln(a_{Ca})$  measured and modeled, by minimizing the quantity:

```
tot_error=1/7*(sum(from i=1to 7, [ln(aCa,exp) - ln(aCa,MIVM)]^2)^1/2
```

This quantity corresponds to the norm 2 of the error.

For each one of these compositions,  $\ln a_{Ca}$  from the MIVM is solely a function of the interaction coefficients. Therefore, the error is also a function of the interaction coefficients.

At the minimum of err, the err partial derivatives with respect to the interaction coefficients are equal to zero. The partial derivatives of err are:

```
d(tot_error)/d(Bij)=-1/7*(sum(from i=1 to 7, [ln(aCa,exp) - ln(aCa,MIVM)] x d(lnaCa, MIVM)/d(Bij))...
.../(sum(from i=1to 7, [ln(aCa,exp) - ln(aCa,MIVM)]^2)^1/2
```

```
d(tot_error)/d(Bji)=-1/7*(sum(from i=1 to 7, [ln(aCa,exp) - ln(aCa,MIVM)] x d(lnaCa, MIVM)/d(Bji))...
.../(sum(from i=1to 7, [ln(aCa,exp) - ln(aCa,MIVM)]^2)^1/2
```

since we are interested in the values of  $B_{ij}$  and  $B_{ji}$  for which the partial derivatives are equal to 0, only the numerator of these functions matter for this determination:

```
derror_ij=(sum(from i=1 to 7, [ln(aCa,exp) - ln(aCa,MIVM)] x d(lnaCa, MIVM)/d(Bij)))
```

```
derror_ji=(sum(from i=1 to 7, [ln(aCa,exp) - ln(aCa,MIVM)] x d(lnaCa, MIVM)/d(Bji)))
```

Below, the quantities necessary for this determination are defined for each composition as follow:

$\ln a$ : natural logarithm of the activity of Ca modeled by the MIVM

```
dlna_ij=d(lnaCa, MIVM)/d(Bij)
```

```
dlna_ji=d(lnaCa, MIVM)/d(Bji)
```

```
derror_ij=[ln(aCa,exp) - ln(aCa,MIVM)] x d(lnaCa, MIVM)/d(Bij)
```

```
derror_ji=[ln(aCa,exp) - ln(aCa,MIVM)] x d(lnaCa, MIVM)/d(Bji)
```

```
Ina_1:=(B_CaSn,B_SnCa)->lna(1,B_CaSn,B_SnCa):
dlna_1_ij:=(B_CaSn,B_SnCa)->dlna_ij(1,B_CaSn,B_SnCa):
dlna_1_ji:=(B_CaSn,B_SnCa)->dlna_ji(1,B_CaSn,B_SnCa):
derror_1_ij:=(B_CaSn,B_SnCa)->((ln_activity_Ca[1]-lna_1(B_CaSn,B_SnCa))*dlna_1_ij(B_CaSn,B_SnCa)):
derror_1_ji:=(B_CaSn,B_SnCa)->((ln_activity_Ca[1]-lna_1(B_CaSn,B_SnCa))*dlna_1_ji(B_CaSn,B_SnCa)):

Ina_2:=(B_CaSn,B_SnCa)->lna(2,B_CaSn,B_SnCa):
dlna_2_ij:=(B_CaSn,B_SnCa)->dlna_ij(2,B_CaSn,B_SnCa):
dlna_2_ji:=(B_CaSn,B_SnCa)->dlna_ji(2,B_CaSn,B_SnCa):
derror_2_ij:=(B_CaSn,B_SnCa)->((ln_activity_Ca[2]-lna_2(B_CaSn,B_SnCa))*dlna_2_ij(B_CaSn,B_SnCa)):
derror_2_ji:=(B_CaSn,B_SnCa)->((ln_activity_Ca[2]-lna_2(B_CaSn,B_SnCa))*dlna_2_ji(B_CaSn,B_SnCa)):

Ina_3:=(B_CaSn,B_SnCa)->lna(3,B_CaSn,B_SnCa):
dlna_3_ij:=(B_CaSn,B_SnCa)->dlna_ij(3,B_CaSn,B_SnCa):
```

Figure B-2: MuPAD algorithm 2 (cont.)

```

dlna_3_ji:=(B_CaSn,B_SnCa)->dlna_ji(3,B_CaSn,B_SnCa):
derror_3_ij:=(B_CaSn,B_SnCa)->((ln_activity_Ca[3]-lna_3(B_CaSn,B_SnCa))*dlna_3_ij(B_CaSn,B_SnCa)):
derror_3_ji:=(B_CaSn,B_SnCa)->((ln_activity_Ca[3]-lna_3(B_CaSn,B_SnCa))*dlna_3_ji(B_CaSn,B_SnCa)):

lna_4:=(B_CaSn,B_SnCa)->lna(4,B_CaSn,B_SnCa):
dlna_4_ij:=(B_CaSn,B_SnCa)->dlna_ij(4,B_CaSn,B_SnCa):
dlna_4_ji:=(B_CaSn,B_SnCa)->dlna_ji(4,B_CaSn,B_SnCa):
derror_4_ij:=(B_CaSn,B_SnCa)->((ln_activity_Ca[4]-lna_4(B_CaSn,B_SnCa))*dlna_4_ij(B_CaSn,B_SnCa)):
derror_4_ji:=(B_CaSn,B_SnCa)->((ln_activity_Ca[4]-lna_4(B_CaSn,B_SnCa))*dlna_4_ji(B_CaSn,B_SnCa)):

lna_5:=(B_CaSn,B_SnCa)->lna(5,B_CaSn,B_SnCa):
dlna_5_ij:=(B_CaSn,B_SnCa)->dlna_ij(5,B_CaSn,B_SnCa):
dlna_5_ji:=(B_CaSn,B_SnCa)->dlna_ji(5,B_CaSn,B_SnCa):
derror_5_ij:=(B_CaSn,B_SnCa)->((ln_activity_Ca[5]-lna_5(B_CaSn,B_SnCa))*dlna_5_ij(B_CaSn,B_SnCa)):
derror_5_ji:=(B_CaSn,B_SnCa)->((ln_activity_Ca[5]-lna_5(B_CaSn,B_SnCa))*dlna_5_ji(B_CaSn,B_SnCa)):

lna_6:=(B_CaSn,B_SnCa)->lna(6,B_CaSn,B_SnCa):
dlna_6_ij:=(B_CaSn,B_SnCa)->dlna_ij(6,B_CaSn,B_SnCa):
dlna_6_ji:=(B_CaSn,B_SnCa)->dlna_ji(6,B_CaSn,B_SnCa):
derror_6_ij:=(B_CaSn,B_SnCa)->((ln_activity_Ca[6]-lna_6(B_CaSn,B_SnCa))*dlna_6_ij(B_CaSn,B_SnCa)):
derror_6_ji:=(B_CaSn,B_SnCa)->((ln_activity_Ca[6]-lna_6(B_CaSn,B_SnCa))*dlna_6_ji(B_CaSn,B_SnCa)):

lna_7:=(B_CaSn,B_SnCa)->lna(7,B_CaSn,B_SnCa):
dlna_7_ij:=(B_CaSn,B_SnCa)->dlna_ij(7,B_CaSn,B_SnCa):
dlna_7_ji:=(B_CaSn,B_SnCa)->dlna_ji(7,B_CaSn,B_SnCa):
derror_7_ij:=(B_CaSn,B_SnCa)->((ln_activity_Ca[7]-lna_7(B_CaSn,B_SnCa))*dlna_7_ij(B_CaSn,B_SnCa)):
derror_7_ji:=(B_CaSn,B_SnCa)->((ln_activity_Ca[7]-lna_7(B_CaSn,B_SnCa))*dlna_7_ji(B_CaSn,B_SnCa)):

tot_error:=(B_CaSn,B_SnCa)->1/7*sqrt((ln_activity_Ca[1]-lna_1(B_CaSn,B_SnCa))^2
+(ln_activity_Ca[2]-lna_2(B_CaSn,B_SnCa))^2+(ln_activity_Ca[3]-lna_3(B_CaSn,B_SnCa))^2
+(ln_activity_Ca[4]-lna_4(B_CaSn,B_SnCa))^2+(ln_activity_Ca[5]-lna_5(B_CaSn,B_SnCa))^2
+(ln_activity_Ca[6]-lna_6(B_CaSn,B_SnCa))^2+(ln_activity_Ca[7]-lna_7(B_CaSn,B_SnCa))^2):

derror_ij:=(B_CaSn,B_SnCa)->derror_1_ij(B_CaSn,B_SnCa)+derror_2_ij(B_CaSn,B_SnCa)
+derror_3_ij(B_CaSn,B_SnCa)+derror_4_ij(B_CaSn,B_SnCa)+derror_5_ij(B_CaSn,B_SnCa)
+derror_6_ij(B_CaSn,B_SnCa)+derror_7_ij(B_CaSn,B_SnCa):

derror_ji:=(B_CaSn,B_SnCa)->derror_1_ji(B_CaSn,B_SnCa)+derror_2_ji(B_CaSn,B_SnCa)
+derror_3_ji(B_CaSn,B_SnCa)+derror_4_ji(B_CaSn,B_SnCa)+derror_5_ji(B_CaSn,B_SnCa)
+derror_6_ji(B_CaSn,B_SnCa)+derror_7_ji(B_CaSn,B_SnCa):

```

the total error as a function of  $B_{ij}$  and  $B_{ji}$  is plotted to identify the window to look for the minimum.

```

h := plot::Function3d(tot_error, x = 0.1 .. 5, y = 0.5..10):
plot(h,
  AxesTitles = ["B_CaSn", "B_SnCa", "err"],
  AxesTitleFont = ["Garamond", 15],
  TicksLabelFont = ["Garamond", 12])

```

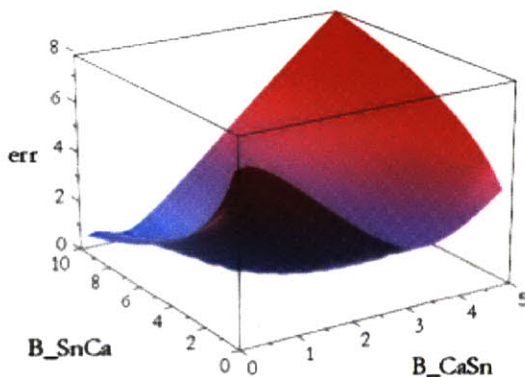


Figure B-2: MuPAD algorithm 2 (cont.)

The values for which the partial derivatives of `tot_error(Bij,Bji)` are equal to zero are then found:  
`x=B_CaSn`  
`y=B_SnCa`

```
numeric::solve([derror_ij(x,y)=0,derror_ji(x,y)=0], [x = 1 .. 3, y = 0.4 .. 10], MultiSolutions)  
{{x= 1.458661252, y= 5.944394784}}
```

Figure B-2: MuPAD algorithm 2 (cont.)

### B.3 Conclusion

The second method gives more precision on the interaction coefficients, but the first method is faster and gives the same values for the coefficients  $\pm 0.01$ .



# Bibliography

- [1] Metalprices online database.
- [2] R. Agarwal, J. J. Lee, H. L. Lukas, and F. Sommer. Calorimetric measurements and thermodynamic optimization of the Ca-Mg system. *Zeitschrift fuer Metallkunde/Materials Research and Advanced Techniques*, 86(2):103 – 108, 1995.
- [3] B. Alblas, W. van der Lugt, J. Dijkstra, W. Geertsma, and C. van Dijk. Structure of liquid Na–Sn alloys. *J. Phys. F, Met. Phys. (UK)*, 13(12):2465 – 2477, 1983.
- [4] C. Bale, E. Belisle, P. Chartrand, S. Decterov, G. Eriksson, K. Hack, I.-H. Jung, Y.-B. Kang, J. Melancon, A. Pelton, C. Robelin, and S. Petersen. Factsage thermochemical software and databases - recent developments. *Calphad: Computer Coupling of Phase Diagrams and Thermochemistry*, 33(2):295 – 311, 2009.
- [5] C. Bale, P. Chartrand, S. Decterov, G. Eriksson, K. Hack, R. Ben Mahfoud, J. Melancon, A. Pelton, and S. Petersen. Factsage thermochemical software and databases. *Calphad: Computer Coupling of Phase Diagrams and Thermochemistry*, 26(2):189 – 228, 2002.
- [6] A. Bard and L. Faulkner. *Electrochemical methods: fundamentals and applications*. John Wiley and sons, inc., second edition, 2001.
- [7] C. Bergman, R. Castanet, H. Said, M. Gilbert, and J.-C. Mathieu. Configurational entropy and the regular associated model for compound-forming binary systems in the liquid state. *J. Less-Common Met. (Switzerland)*, 85(1):121 – 135, 1982.
- [8] A. Bhatia and W. Hargrove. Concentration fluctuations and thermodynamic properties of some compound forming binary molten systems. *Phys. Rev. B*, 10(8):3186 – 3196, 1974.
- [9] R. Blachnik and B. Gather. Die Mischungsenthalpien im System Zinn-Tellur. *Zeitschrift fuer Metallkunde/Materials Research and Advanced Techniques*, 74(3):172 – 176, 1983.
- [10] A. Bouhajib. *Etude thermodynamique des systemes bismuth-calcium et calcium-antimoine: calorimetrie, analyse thermique differentielle et modelisation numerique des diagrammes de phases*. PhD thesis, Universite de Nancy I, 1990.

- [11] A. Bouhajib, A. Nadiri, A. Yacoubi, and R. Castanet. Investigation of the short-range order in the Ca–Sb melts. *J. Alloys Compd. (Switzerland)*, 287(1-2):167 – 169, 1999.
- [12] A. Bouhajib, M. Notin, A. Nadiri, and A. Yacoubi. Calorimetric study coupled with a numerical optimization technique for the Ca-Sb system. *High Temperature Materials and Processes*, 18(3):151 – 158, 1999.
- [13] L. Bouriden. PhD thesis, University of Nancy I, France, 1984.
- [14] D. Bradwell. *Liquid Metal Batteries: Ambipolar Electrolysis and Alkaline Earth Electroalloying Cells*. PhD thesis, Massachusetts Institute of Technology, 2010.
- [15] D. Bradwell, G. Ceder, L. Ortiz, and D. Sadoway. Liquid electrode battery. US Patent appl. 12/839,130, Jul 2010.
- [16] D. J. Bradwell. Technical and economic feasibility of a high-temperature self-assembling battery. Master’s thesis, Materials Science and Engineering, MIT, 2006.
- [17] D. J. Bradwell, H. Kim, A. H. C. Sirk, and D. R. Sadoway. Magnesium–antimony liquid metal battery for stationary energy storage. *Journal of the American Chemical Society*, 134(4):1895–1897, 2012.
- [18] W. C. Butterman and J. F. J. Carlin. Mineral commodity profiles - antimony. Technical Report 03-019, U.S. Department of the Interior - U.S. Geological Survey, 2004.
- [19] E. Cairns, C. Crouthamel, A. Fischer, M. Foster, J. Hesson, C. Johnson, H. Shimotake, and A. Tevebaugh. Galvanic cells with fused salts. Technical report, Argonne National Laboratory, 1967.
- [20] E. Cairns and H. Shimotake. High-temperature batteries. *Science*, 164(3886):1347–1355, 1969.
- [21] Y. Cartigny, J. Fiorani, A. Maitre, and M. Vilasi. Thermodynamic assessment of the Ca-Pb system. *Thermochimica Acta*, 414(2):197 – 202, 2004.
- [22] Y. Cartigny, J. Fiorani, A. Maitre, and M. Vilasi. Thermodynamic assessment of the Ca-Sn system. *Zeitschrift fuer Metallkunde/Materials Research and Advanced Techniques*, 96(11):1308 – 1313, 2005.
- [23] J. Delcet, A. Delgado-Brune, and J. Egan. Coulometric titrations using CaF<sub>2</sub> and BaF<sub>2</sub> solid electrolytes to study alloy phases. Technical report, Brookhaven National Laboratory, 1979.
- [24] J. Delcet and J. Egan. Thermodynamics of liquid Ca-Ag and Ca-In alloys. *J. Less-Common Met. (Switzerland)*, 59(2):229 – 36, 1978.



- [25] J. Delcet and J. Egan. Thermodynamics of liquid Ca-Zn alloys. *Metall. Trans. B, Process Metall. (USA)*, 9B(4):728 – 729, 1978.
- [26] K. El Aissaoui, N. Selhaoui, J. Charles, and B. L. Modelisation numerique des systemes Ag-Ca et Cu-Ca. *Ann. Chim. Sci. Mat*, 22:517–527, 1997.
- [27] D. Fray and R. Kumar. Electrochemical determination of the thermodynamics of the Ca-Pb system at 1173 K using calcium magnetoplumbite as the electrolyte. *Scandinavian Journal of Metallurgy*, 22(5):266 – 270, 1993.
- [28] K. Grjotheim and H. Kvande. *Introduction to aluminium electrolysis*. Aluminium-Verlag, 2nd edition, 1993.
- [29] J.-M. Hicter, A. Vermande, I. Ansara, and P. Desbe. Thermodynamical investigation of liquid Al-Li alloys. *Rev. Int. Hautes Temp. Refract. (France)*, 8(s3-4):197 – 200, 1971.
- [30] K. Hilpert. Investigation of the gaseous systems Ag-Dy and Au-Dy. *Advances in Mass Spectrometry*, 7a:584–587, 1978.
- [31] A. Hines, H. Walls, and K. Jethani. Determination of the coordination number of liquid metals near the melting point. *Metall. Trans. A, Phys. Metall. Mater. Sci. (USA)*, 16A(2):267 – 74, 1985.
- [32] R. Hultgren, P. D. Desai, D. T. Hawkins, M. Gleiser, K. K. Kelley, and D. D. Wagman. *Selected values of the thermodynamic properties of the elements*. American society for metals, 1973.
- [33] R. Hyers and J. Rogers. A review of electrostatic levitation for materials research. *High Temperature Materials and Processes*, 27(6):461–474, 2008.
- [34] T. Iida and R. I. Guthrie. *The physical properties of liquid metals*. Oxford: Clarendon Press, 1988.
- [35] H. Ipser. Vapor pressure methods: a source of experimental thermodynamic data. volume 102, pages 1217 – 24, Germany, 1998.
- [36] F. Islam and M. Medraj. The phase equilibria in the Mg-Ni-Ca system. *Calphad*, 29(298-302), 2005.
- [37] V. P. Itkin and C. B. Alcock. The Ca-Zn (calcium-zinc) system. *Bulletin of Alloy Phase Diagrams*, 11(4):328–333, 1990.
- [38] V. P. Itkin and C. B. Alcock. the Ca-Pb (calcium-lead) system. *J. Phase Equilib.*, 13:162–169, 1992.
- [39] H. Kim, D. Boysen, D. J. Bradwell, B. Chung, K. Jiang, A. A. Tomaszowska, K. Wang, W. Wei, and D. R. Sadoway. Thermodynamic properties of calcium-bismuth alloys determined by emf measurements. *Electrochimica Acta*, 60:154–162, 2012.

- [40] H. Kim, D. Boysen, J. M. Newhouse, B. L. Spatocco, B. Chung, P. J. Burke, D. J. Bradwell, K. Jiang, A. A. Tomaszowska, K. Wang, W. Wei, L. Ortiz, S. A. Barriga, S. Poizeau, and D. R. Sadoway. Liquid metal batteries: Past, present, and future. submitted to *Chemical Reviews*, 2012.
- [41] K. L. Komarek. Experimental techniques in high temperature thermodynamics. *Pure and Appl. Chem*, 64(1):93–102, 1992.
- [42] H.-G. Krull, R. Singh, and F. Sommer. Generalised association model. *Z. Met.kd. (Germany)*, 91(5):356 – 365, 2000.
- [43] O. Kubaschewski and A. Walter-Stuttgart. Erfahrungen und Ergebnisse bei der Hochtemperaturcalorimetrie der Legierungen. *Z. Elektrochem*, 45(9):732–740, 1939.
- [44] V. Kuznetsov. System Sn-Te: Critical evaluation and optimization of data on the thermodynamic properties and phase diagram. *Inorg. Mater.*, 32:231–242, 1996.
- [45] S. Matsunaga, T. Ishiguro, and S. Tamaki. Thermodynamic properties of liquid Na–Pb alloys. *J. Phys. F, Met. Phys. (UK)*, 13(3):587 – 595, 1983.
- [46] A. Morachesvkii, V. Bulatova, and A. Demidov. Reactions of lithium-tin alloys with low-melting chloride electrolytes. *Soviet Electrochemistry (translated)*, 12(8):1213–1214, 1977.
- [47] A. A. Nayeb-Hashemi and J. B. Clark. The Ca-Mg (calcium-magnesium) system. *Bulletin of Alloy Phase Diagrams*, 8(1):58–65, 1987.
- [48] J. M. Newhouse, S. Poizeau, H. Kim, B. L. Spatocco, and D. R. Sadoway. Thermodynamic properties of calcium-magnesium alloys determined by emf measurements. submitted to *Electrochimica Acta*, 2012.
- [49] Z. Niyazova, A. Vakhobov, and T. Dzhuraev. Phase diagram of the system Ca–Sb. *Inorg. Mater. (USA)*, 12(7):1074 – 1075, 1976.
- [50] M. Notin, J. Mejbar, A. Bouhajib, J. Charles, and J. Hertz. The thermodynamic properties of calcium intermetallic compounds. *J. Alloys Compd. (Switzerland)*, 220:62 – 75, 1995.
- [51] H. Ohtani, K. Okuda, and K. Ishida. Thermodynamic study of phase equilibria in the Pb-Sn-Sb system. *Journal of Phase Equilibria*, 16(5):416 – 429, 1995.
- [52] H. Okamoto. Li-Pb (lithium-lead). *J. Phase Equilib.*, 14:770, 1993.
- [53] H. Okamoto. Ca-Sb (calcium-antimony). *Journal of Phase Equilibria*, 18(3):313, 1997.
- [54] H. Okamoto, V. P. Itkin, and C. B. Alcock. The Ca-In (calcium-indium) system. *Journal of Phase Equilibria*, 12(3):379–383, 1991.

- [55] M. C. Parent. Economic assessment of candidate materials for key components in a grid-scale liquid metal battery. Master's thesis, Massachusetts Institute of Technology, June 2011.
- [56] A. Petric, A. Pelton, and M.-L. Saboungi. Thermodynamic properties of liquid K–Bi alloys by electromotive force measurements. *J. Phys. F: Met. Phys.*, 18:1473–1489, 1988.
- [57] S. Poizeau, H. Kim, J. M. Newhouse, B. L. Spatocco, and D. R. Sadoway. Determination and modeling of the thermodynamic properties of liquid calcium–antimony alloys. *Electrochimica Acta*, 76:8–15, 2012.
- [58] J. Pratt. Applications of solid electrolytes in thermodynamic studies of materials: a review. *Metall. Trans. A, Phys. Metall. Mater. Sci. (USA)*, 21A(5):1223 – 50, 1990.
- [59] J. Prausnitz, R. Lichtenthaler, and E. Gomes de Azevedo. *Molecular Thermodynamics of Fluid-Phase Equilibria*. Prentice Hall PTR, third edition, 1999.
- [60] B. Predel and G. Oehme. Kalorimetrische Untersuchung fluessiger Lithium-Blei-Legierungen. *Zeitschrift fuer Metallkunde/Materials Research and Advanced Techniques*, 70(7):450 – 453, 1979.
- [61] A. Rais, N. Cusak, and F. Neale. Simultaneous measurement of resistivity and thermodynamic properties of liquid binary alloys. application to Na–In, Na–Sn. *J. Phys. F, Met. Phys. (UK)*, 12(6):1091 – 1100, 1982.
- [62] J. Rogers and R. Hyers. Electrostatic levitation: an emerging materials characterization technique. In TMS, editor, *Supplemental Proceedings: Volume 2: Characterization, Computation and Modeling*, pages 9–14, 2008.
- [63] H. Said, R. Castanet, M. Gilbert, and J. Mathieu. Two cluster regular associated model for binary liquid alloys. *J. Less-Common Met. (Switzerland)*, 96:79 – 91, 1984.
- [64] G. Sauthoff. *Intermetallics*. VCH, 1995.
- [65] H. Schmalzried. *Solid state reactions*. Monographs in modern chemistry, 1981.
- [66] J. Sebkova and M. Beranek. Thermodynamic properties of liquid Pb-Sb alloy. *Kov. Mater. (Czechoslovakia)*, 17(4):393 – 403, 1979.
- [67] S. Shaw and R. Watson. Solubility of calcium in CaCl<sub>2</sub>-CaO. In T. E. Society, editor, *ECS transactions*, volume 16, pages 301–308, 2009.
- [68] F. Sommer. Determination of thermodynamic activities of liquid alloys in the system Ca-Mg using a modified Ruff method. *Z. Met.kd. (West Germany)*, 70(3):545 – 7, 1979.

- [69] F. Sommer. Association model for the description of the thermodynamic functions of liquid alloys. i. basic concepts. *Z. Met.kd. (West Germany)*, 73(2):72 – 6, 1982.
- [70] F. Sommer. Thermodynamic properties of compound-forming liquid alloys. *Journal of Non-Crystalline Solids*, 117-18(pt 2):505 – 512, 1990.
- [71] F. Sommer and D. K. Choi. Thermodynamic investigations of liquid and glassy copper-zirconium alloys. *Z. Met.kd. (West Germany)*, 80(4):263 – 9, 1989.
- [72] S. Tamaki, T. Ishiguro, and S. Takeda. Thermodynamic properties of liquid Na-Sn alloys. *J. Phys. F, Met. Phys. (UK)*, 12(8):1613 – 24, 1982.
- [73] D. P. Tao. A new model of thermodynamics of liquid mixtures and its application to liquid alloys. *Thermochimica Acta*, 363:105–113, 2000.
- [74] D. P. Tao. Prediction of the thermodynamic properties of multicomponent liquid alloys by binary infinite dilute activity coefficients. *Metallurgical and Materials Transactions B: Process Metallurgy and Materials Processing Science*, 32(6):1205 – 1211, 2001.
- [75] D. P. Tao. Prediction of the thermodynamic properties of solutes in the Bi-based ternary dilute solution. *Metallurgical and Materials Transactions B: Process Metallurgy and Materials Processing Science*, 33(3):502 – 506, 2002.
- [76] D. P. Tao. A comparison of the molecular interaction volume model with the subregular solution model in multicomponent liquid alloys. *Metallurgical and Materials Transactions A: Physical Metallurgy and Materials Science*, 35 A(2):419 – 424, 2004.
- [77] D. P. Tao. Prediction of the coordination numbers of liquid metals. *Metall. Mater. Trans. A, Phys. Metall. Mater. Sci. (USA)*, 36A(12):3495 – 3497, 2005.
- [78] D. P. Tao. Prediction of activities of all components in the lead-free solder systems Bi-In-Sn and Bi-In-Sn-Zn. *J. Alloys Compd. (Switzerland)*, 457(1-2):124 – 30, 2008.
- [79] D. P. Tao, B. Yang, and D. F. Li. Prediction of the thermodynamic properties of quinary liquid alloys by modified coordination equation. *Fluid Phase Equilibria*, 193(1-2):167 – 177, 2002.
- [80] Y. Waseda. The structure of liquid transition metals and their alloys. In *Liquid metals*, pages 230 – 40, London, UK, 1976.
- [81] A. Zevalkink, E. S. Toberer, W. G. Zeier, E. Flage-Larsen, and G. J. Snyder.  $\text{Ca}_3\text{AlSb}_3$ : An inexpensive, non-toxic thermoelectric material for waste heat recovery. *Energy and Environmental Science*, 4(2):510 – 518, 2011.